

Resolved Radio Continuum in Dwarf Galaxies: 6 cm imaging of LITTLE THINGS

Ged Kitchener¹, Elias Brinks¹, Volker Heesen², Deidre A. Hunter³, Hong-Xin Zhang⁴,
Michael P. Rupen⁵, Urvashi Rau⁵

ABSTRACT

Instructions AASTEX: <http://aas.org/authors/aas-journal-reference-instructions>

Preparing the manuscript: <http://texdoc.net/texmf-dist/doc/latex/aastex/aasguide.pdf>

To bypass uncertainties introduced by extinction by dust in the optical, we examine to what extent the radio continuum can probe star formation in dwarf galaxies. We provide JVLA C-band C-array (4–8 GHz) radio continuum images with integrated flux densities for 40 dwarf galaxies taken from LITTLE THINGS. We find 26 harbour significant emission coincident with SF tracers; 17 are new detections. We infer the average thermal fraction to be $(42 \pm 24)\%$, and the non-thermal fraction to be $(58 \pm 24)\%$. The LITTLE THINGS galaxies follow the Condon radio continuum – star formation rate relation down to a star formation rate of $\sim 0.1M_{\odot} \text{ yr}^{-1}$. At lower star formation rates, they follow a power-law characterised by a slope of $\sim 1.2 \pm 0.1$ with a scatter of 0.2 dex. We interpret this as an underproduction of both the thermal radio continuum due to a truncated stellar initial mass function and the non-thermal radio continuum component not due to a lower magnetic field strength (found to be typically $(9.3 \pm 4.2)\mu\text{G}$), but due to the escape of Cosmic Ray electrons perhaps facilitated by a small magnetic field scale height. The LITTLE THINGS galaxies fall below the radio continuum – far infrared relation; the observed radio continuum falls a factor of 2 below that predicted from the far infrared consistently across our range of dwarf galaxies. We observe a power-law slope of $\sim 1.05 \pm 0.08$ with a scatter of 0.25 dex—consistent with a linear trend suggesting that the ‘conspiracy’ of the radio continuum – far infrared relation continues to hold even for dwarf galaxies. However, we also find tentative evidence that the radio continuum becomes deficient with respect to far infrared emission when looking at the $q_{70.6}$ parameter—this may be explained by the rising importance of the interstellar radiation field (as opposed to massive stars) as a heating source for dust in low star formation rate systems such as LITTLE THINGS.

Subject headings: dwarf galaxies: star formation — dwarf galaxies: magnetic fields — dwarf galaxies: radio continuum — dwarf galaxies: individual(NGC 1569, NGC 4214, Holmberg I, Holmberg II, Sextans A, Sextans B, IC 10, IC 1613,)

¹Centre for Astrophysics Research, University of Hertfordshire, Hatfield, AL10 9AB, United Kingdom

²School of Physics and Astronomy, University of Southampton, Southampton, SO17 1BJ, United Kingdom

³Lowell Observatory, 1400 West Mars Hill Road, Flagstaff, AZ 86001, USA

⁴Peking University, Beijing, China

⁵National Radio Astronomy Observatory, 1003 Lopezville Road, Socorro, NM 87801, USA

1. Introduction

The Radio Continuum (RC) – Far Infrared (FIR) relation of galaxies holds over 4 orders of magnitude in luminosity, irrespective of galaxy type (Helou et al. 1985; de Jong et al. 1985; Yu et al. 2001). It displays only a 0.26 dex scatter (Yu et al. 2001) and has been observed to hold to a redshift of 3 (Appleton et al. 2004). The RC (see Condon 1992, for a review) and the FIR have long

been attributed to the input of energy following a star formation (SF) event. In C -band (4–8 GHz or 7.50–3.75 cm), the RC comprises two main contributions: a thermal component (RC_{Th}) and a non-thermal component (RC_{NTh}). The RC_{Th} comes about as follows: photons of $\lambda \leq 912\text{\AA}$ ionise hydrogen surrounding the most massive, short-lived stars ($M \gtrsim 18 M_{\odot}$, $t_{life} \lesssim 10$ Myr; Hunter & Elmegreen 2004). The resulting plasma then radiates due to, primarily, free electrons interacting with free ions leading to Bremsstrahlung emission. The RC_{Th} is mostly confined to H II regions, and is dependent on these most massive, short-lived stars which end their existence as supernovae (SNe) approximately 1–10 Myr after the SF episode. The RC_{NTh} finds its origins in the remnants of core-collapse SNe (SNR) whose progenitors are massive, short-lived stars (Maeder & Meynet 1989 find the lifetime of $120M_{\odot}$ stars to be 3.4 Myr, whilst $8M_{\odot}$ stars have lifetimes of 50 Myr). The supernova shock accelerates Cosmic Ray electrons (CRE) to ultra-relativistic velocities, which then spiral around magnetic fields producing synchrotron radiation. CRE may last, typically, 100 Myr after their initial acceleration, and an ensemble of CRE may diffuse or be advected out to typically a kpc from the SF region of origin. The RC_{Th} and RC_{NTh} thus operate on different time and spatial scales. The FIR originates from the black-body radiation of interstellar dust that is heated by the interstellar radiation field (Walter et al. 2007; Wyder et al. 2009; Roychowdhury & Chengalur 2012).

The classical scenario is that of a galaxy acting as a calorimeter (Völk 1989)—one that retains both its dust-heating photons and CRE. The model assumes that dust-heating photons (e.g., optical and UV) are absorbed by dust which eventually reradiates the energy gained as FIR. It also requires that magnetic fields retain all CRE which eventually produce synchrotron radiation. Since all the energy contained within the CRE is radiated, the strength of the magnetic field is irrelevant, i.e., whether the energy contained in the CRE is radiated over 1 Myr in a strong magnetic field, or over 1 Gyr in a weak magnetic field, the total energy emitted is the same. The calorimeter assumption implies that the mean-free-path of dust-heating photons is less than the galaxy disk scale height, and that the typical en-

ergy loss timescale of CRE is less than the diffusion timescale. Clearly, the calorimeter model is not perfect as dust-heating photons are observed coming from galaxies, and RC_{NTh} emission is observed in the haloes of larger spirals (Heesen et al. 2009). Therefore, for galaxies to follow the RC–FIR relation, the escape of CRE from galactic magnetic fields must be in proportion to the escape of dust-heating photons from the disk. Some of the earliest evidence of this comes from Klein et al. (1991) who state that the deficiency of RC_{NTh} ‘happens to be balanced’ by a lack of dust in Blue Compact Dwarfs (BCDs). This is known as the ‘conspiracy’ between the emission of RC and FIR (e.g., Bell 2003; Dale et al. 2009; Lacki et al. 2010).

In the case of dwarf galaxies, observations show that they contain less dust than spirals (Lisenfeld & Ferrara 1998; Bigiel et al. 2008), yet still follow the RC–FIR relation (Price & Duric 1992; Yun et al. 2001). To complicate the picture yet further, heating of the diffuse cold dust by photons may not be sufficient to make the RC–FIR relation as tight as is observed; Xu (1990) found that a significant fraction of the heating of diffuse cool dust could not be accounted for by UV radiation in their sample of 40 spiral galaxies. An alternative source to compensate for the insufficient UV-heating could be heating by CRE (e.g., in Ultra-Luminous Infrared Galaxies (ULIRGS); Papadopoulos 2010); however, it is not known how effective this source of heating is in systems of such low dust densities as dwarf galaxies.

The deficiency of the RC can be explained by an underproduction of both the RC_{Th} and RC_{NTh} components. A truncated stellar IMF in dwarf galaxies may lead to fewer high mass stars being born for a given SFR (Wyder et al. 2007; Lee et al. 2009; Plöckinger et al. in prep.); with fewer high mass stars producing the ionising photons needed to create H II regions, less $H\alpha$ (and RC_{Th}) is emitted. **For the least active dwarf galaxies ($SFR \lesssim 10^{-4} M_{\odot} \text{yr}^{-1}$), the $H\alpha$ emission underestimates the SFR given by FUV by a factor of 10. Only the highest mass stars ($M \gtrsim 18 M_{\odot}$) produce a significant number of photons to ionize the surrounding H I; having a deficit of these stars significantly reduces the amount of $H\alpha$ emission, while the FUV emission is not affected as much since a larger fraction of the stellar population contributes to the FUV emission.** Additionally, dwarf

galaxies generally lack differential rotation (Gallagher & Hunter 1984), and are not able to stretch small scale magnetic field perturbations (this α - ω process happens in larger, grand-design spirals leading to ordered fields of $\sim 5\mu\text{G}$ between the optical arms; Beck 2009). The low mass of dwarf galaxies makes them episodic (e.g., Stinson et al. 2007, liken the SF history of isolated dwarf galaxies to ‘breathing’) and vulnerable to the energy input following major SF episodes—the buoyancy of hot plasma manifests itself as advective winds taking resident CRE out of the galaxy and into the intragalactic medium (Heesen et al. 2009; Dubois & Teyssier 2010; Heesen et al. 2011). The energy input also disrupts ordered fields—this is why regions of SF (i.e., optical arms of spirals, H II regions in dwarf galaxies) are dominated by turbulent magnetic fields. For the same reason, polarised emission is expected to be weak.

The fact that dwarf galaxies follow the RC–FIR relation of spiral galaxies is intriguing—especially when we consider that dwarf galaxies are different from spiral galaxies in terms of their magnetic field (e.g., Chyży et al. 2011; Roychowdhury & Chengalur 2012), rotation (e.g., Gallagher & Hunter 1984), dust content (e.g., Lisensfeld & Ferrara 1998; Bigiel et al. 2008; Ficut-Vicas et al. 2013), and stellar initial mass function (IMF) (e.g., Weidner & Kroupa 2005; Lee et al. 2009; Plöckinger et al. in prep.). For all these differences, the RC–SFR and RC–FIR relations are expected to break down in dwarf galaxies, even for integrated measurements; it is puzzling why the RC, FIR, and SFR are related so closely.

To more fully understand the role that episodic SF plays in the RC–SFR and RC–FIR relations, examining SF on galactic scales in dwarf galaxies might be simpler than examining their larger, more complex spiral cousins. Dwarf galaxies, generally having had no major mergers to date, being devoid of Active Galactic Nuclei (AGN) contamination, pave a more accessible route to understanding the RC–SFR and RC–FIR relations.

Historically, spatially resolved studies of the RC in dwarf galaxies have been limited by their intrinsically low surface brightness. Limitations in instrument sensitivity forced investigations of the RC in dwarf galaxies to either: 1) a case–study orientated approach if resolved studies were desired, or 2) an approach based on integrated prop-

erties if the behaviour of a population was being investigated. Resolved observations have been reserved for the elite few—the near and bright IC 10 (Heesen et al. 2011), IC 1613 (Chyży et al. 2011), NGC 4214 (Kepley et al. 2011), NGC 1569 (Lisensfeld et al. 2004; Kepley et al. 2010), and the Magellanic Clouds (Filipovic et al. 1995, 1998). Studies into the RC emission of dwarf galaxies as a population have been few and far between. Studies have been characterised by upper limits on globally integrated quantities (e.g., Altschuler et al. 1984; Klein 1986; Price & Duric 1992; Klein et al. 1992; Höppe et al. 1994). All-sky surveys never reached the sensitivities to probe the population of dwarf galaxies—the NRAO¹ VLA Sky Survey (NVSS; Condon et al. 1998) and Faint Images of the Radio Sky at Twenty-cm (FIRST; White et al. 1997) were only able to detect the brightest few. Despite NVSS non-detections of individual galaxies, Roychowdhury & Chengalur (2012) used 57 stacked NVSS images to infer magnetic field properties in faint dwarf galaxies.

In 2011, the NRAO Karl G. Jansky Very Large Array (VLA) completed a major upgrade increasing receiver sensitivity as well as introducing a 20-fold increase of bandwidth coverage across C-band (4–8 GHz). This offered the opportunity to revisit the RC in dwarf galaxies. More importantly, it provided the tantalising prospect for a spatially resolved study of the RC in a considerably sized sample of dwarf galaxies.

We concentrate on nearby gas-rich dwarf galaxies. In this paper, we present JVLA C-band images of 40 such dwarf galaxies corresponding to the LITTLE THINGS² sample (Hunter et al. 2012). We focus on describing the sample, our calibration and imaging process, and presenting our analysis in conjunction with star formation rate (SFR) indicators.

We will discuss the integrated measurements. A study singling individual regions of SF will be

¹The National Radio Astronomy Observatory is a facility of the National Science Foundation operated under cooperative agreement by Associated Universities, Inc.

²Based on data from the LITTLE THINGS Survey (Hunter et al. 2012), funded in part by the National Science Foundation through grants AST-0707563, AST-0707426, AST-0707468, and AST-0707835 to US-based LITTLE THINGS team members and with generous support from the National Radio Astronomy Observatory.

the subject of a subsequent paper (G. Kitchener et al. in prep.).

The ultimate aim is to increase our understanding of the RC–SFR relation of low mass, low metallicity systems. With the development of the SKA, calibrating the RC–SFR relation in quiescent/low SFR galaxies will become more important than ever. Our calibration of the RC–SFR relation may provide a sound foundation on which to base high redshift surveys which will be significantly populated by normal star forming galaxies.

This paper is organized as follows: in Section 2 we describe the observations, calibration, and imaging of our sample. We present our results (images and integrated emission) in Section 3. We then discuss our results, paying particular attention to the RC–SFR and RC–FIR relations in Sections 4.2 and 4.4, respectively. We summarise our results and conclude in Section 5.

TABLE 1
THE GALAXY SAMPLE (SEE END OF DOCUMENT FOR HOW TABLE SHOULD LOOK LIKE)

Galaxy	Other names ^a	D (Mpc)	Ref ^b	M_V (mag)	R_H^c (arcmin)	R_D^c (kpc)	$E(B - V)^d$	$\log_{10} \Sigma_{SFR, D}^{H\alpha}$ ($M_{\odot} \text{yr}^{-1} \text{kpc}^{-2}$) ^e	$\log_{10} \Sigma_{SFR, D}^{FUV}$ ($M_{\odot} \text{yr}^{-1} \text{kpc}^{-2}$) ^e	$12 + \log_{10} \text{O}/\text{H}^f$	Re
Im Galaxies											
CVnIrwA	UGCA 292	3.6	1	-12.4	0.87	0.57 ± 0.12	0.01	-2.58 ± 0.01	-2.48 ± 0.01	7.3 ± 0.06	24
DDO 43	PGC 21073, UGC 3860	7.8	2	-15.1	0.89	0.41 ± 0.03	0.05	-1.78 ± 0.01	-1.55 ± 0.01	8.3 ± 0.09	25
DDO 46	PGC 21585, UGC 3966	6.1	...	-14.7	...	1.14 ± 0.06	0.05	-2.89 ± 0.01	-2.46 ± 0.01	8.1 ± 0.1	25
DDO 47	PGC 21600, UGC 3974	5.2	3	-15.5	2.24	1.37 ± 0.06	0.02	-2.70 ± 0.01	-2.40 ± 0.01	7.8 ± 0.2	26
DDO 50	PGC 23324, UGC 4305, Holmberg II, VII Zw 223	3.4	1	-16.6	3.97	1.10 ± 0.05	0.02	-1.67 ± 0.01	-1.55 ± 0.01	7.7 ± 0.14	27
DDO 52	PGC 23769, UGC 4426	10.3	4	-15.4	1.08	1.30 ± 0.13	0.03	-3.20 ± 0.01	-2.43 ± 0.01	(7.7)	28
DDO 53	PGC 24050, UGC 4459, VII Zw 238	3.6	1	-13.8	1.37	0.72 ± 0.06	0.03	-2.42 ± 0.01	-2.41 ± 0.01	7.6 ± 0.11	27
DDO 63	PGC 27605, Holmberg I, UGC 5139, Mailyan 044	3.9	1	-14.8	2.17	0.68 ± 0.01	0.01	-2.32 ± 0.01	-1.95 ± 0.00	7.6 ± 0.11	27
DDO 69	PGC 28868, UGC 5364, Leo A	0.8	5	-11.7	2.40	0.19 ± 0.01	0.00	-2.83 ± 0.01	-2.22 ± 0.01	7.4 ± 0.10	29
DDO 70	PGC 28913, UGC 5373, Sextans B	1.3	6	-14.1	3.71	0.48 ± 0.01	0.01	-2.85 ± 0.01	-2.16 ± 0.00	7.5 ± 0.06	30
DDO 75	PGC 29653, UGCA 205, Sextans A	1.3	7	-13.9	3.09	0.22 ± 0.01	0.02	-1.28 ± 0.01	-1.07 ± 0.01	7.5 ± 0.06	30
DDO 87	PGC 32405, UGC 5918, VII Zw 347	7.7	...	-15.0	1.15	1.31 ± 0.12	0.00	-1.36 ± 0.01	-1.00 ± 0.01	7.8 ± 0.04	31
DDO 101	PGC 37449, UGC 6900	6.4	...	-15.0	1.05	0.94 ± 0.03	0.01	-2.85 ± 0.01	-2.81 ± 0.01	8.7 ± 0.03	25
DDO 126	PGC 40791, UGC 7559	4.9	8	-14.9	1.76	0.87 ± 0.03	0.00	-2.37 ± 0.01	-2.10 ± 0.01	(7.8)	28
DDO 133	PGC 41636, UGC 7698	3.5	...	-14.8	2.33	1.24 ± 0.09	0.00	-2.88 ± 0.01	-2.62 ± 0.01	8.2 ± 0.09	25
DDO 154	PGC 43869, UGC 8024, NGC 4789A	3.7	...	-14.2	1.55	0.59 ± 0.03	0.01	-2.50 ± 0.01	-1.93 ± 0.01	7.5 ± 0.09	27
DDO 155	PGC 44491, UGC 8091, GR 8, LSB C D646-07	2.2	9	-12.5	0.95	0.15 ± 0.01	0.01	-1.44 ± 0.01	...	7.7 ± 0.06	29
DDO 165	PGC 45372, UGC 8201, II Zw 499, Mailyan 82	4.6	10	-15.6	2.14	2.26 ± 0.08	0.01	-3.67 ± 0.01	...	7.6 ± 0.08	27
DDO 167	PGC 45939, UGC 8308	4.2	8	-13.0	0.75	0.33 ± 0.05	0.00	-2.36 ± 0.01	-1.83 ± 0.01	7.7 ± 0.2	26
DDO 168	PGC 46039, UGC 8320	4.3	8	-15.7	2.32	0.82 ± 0.01	0.00	-2.27 ± 0.01	-2.04 ± 0.01	8.3 ± 0.07	25
DDO 187	PGC 50961, UGC 9128	2.2	1	-12.7	1.06	0.18 ± 0.01	0.00	-2.52 ± 0.01	-1.98 ± 0.01	7.7 ± 0.09	32
DDO 210	PGC 65367, Aquarius Dwarf	0.9	10	-10.9	1.31	0.17 ± 0.01	0.03	...	-2.71 ± 0.06	(7.2)	28
DDO 216	PGC 71538, UGC 12613, Peg DIG, Pegasus Dwarf	1.1	11	-13.7	4.00	0.54 ± 0.01	0.02	-4.10 ± 0.07	-3.21 ± 0.01	7.9 ± 0.15	33
F564-V3	LSBC D564-08	8.7	4	-14.0	...	0.53 ± 0.03	0.02	...	-2.79 ± 0.02	(7.6)	28
IC 10	PGC 1305, UGC 192	0.7	12	-16.3	...	0.40 ± 0.01	0.75	-1.11 ± 0.01	...	8.2 ± 0.12	34
IC 1613	PGC 3844, UGC 668, DDO 8	0.7	13	-14.6	9.10	0.58 ± 0.02	0.00	-2.56 ± 0.01	-1.99 ± 0.01	7.6 ± 0.05	35
LGS 3	PGC 3792, Pisces dwarf	0.7	14	-9.7	0.96	0.23 ± 0.02	0.04	...	-3.88 ± 0.06	(7.0)	28
M81dwA	PGC 23521	3.5	15	-11.7	...	0.26 ± 0.00	0.02	...	-2.26 ± 0.01	(7.3)	28
NGC 1569	PGC 15345, UGC 3056, Arp 210, VII Zw 16	3.4	16	-18.2	...	0.38 ± 0.02	0.51	0.19 ± 0.01	-0.01 ± 0.01	8.2 ± 0.05	36
NGC 2366	PGC 21102, UGC 3851, DDO 42	3.4	17	-16.8	4.72	1.36 ± 0.04	0.04	-1.67 ± 0.01	-1.66 ± 0.01	7.9 ± 0.01	37
NGC 3738	PGC 35856, UGC 6565, Arp 234	4.9	3	-17.1	2.40	0.78 ± 0.01	0.00	-1.66 ± 0.01	-1.53 ± 0.01	8.4 ± 0.01	25
NGC 4163	PGC 38881, NGC 4167, UGC 7199	2.9	1	-14.4	1.47	0.27 ± 0.03	0.00	-2.28 ± 0.13	-1.74 ± 0.01	7.9 ± 0.2	38
NGC 4214	PGC 39225, UGC 7278	3.0	1	-17.6	4.67	0.75 ± 0.01	0.00	-1.03 ± 0.01	-1.08 ± 0.01	8.2 ± 0.06	39
SagDIG	PGC 63287, Lowal's Object	1.1	19	-12.5	...	0.23 ± 0.03	0.14	-2.97 ± 0.04	-2.11 ± 0.01	7.3 ± 0.1	35
UGC 8508	PGC 47495, I Zw 60	2.6	1	-13.6	1.28	0.27 ± 0.01	0.00	-2.03 ± 0.01	...	7.9 ± 0.2	38
WLM	PGC 143, UGCA 444, DDO 221, Wolf-Lundmark-Melott	1.0	20	-14.4	5.81	0.57 ± 0.03	0.02	-2.77 ± 0.01	-2.05 ± 0.01	7.8 ± 0.06	40
BCD Galaxies											
Haro 29	PGC 40665, UGCA 281, Mrk 209, I Zw 36	5.8	21	-14.6	0.84	0.29 ± 0.01	0.00	-0.77 ± 0.01	-1.07 ± 0.01	7.9 ± 0.07	41
Haro 36	PGC 43124, UGC 7950	9.3	...	-15.9	...	0.69 ± 0.01	0.00	-1.86 ± 0.01	-1.55 ± 0.01	8.4 ± 0.08	25
Mrk 178	PGC 35684, UGC 6541	3.9	8	-14.1	1.01	0.33 ± 0.01	0.00	-1.60 ± 0.01	-1.66 ± 0.01	7.7 ± 0.02	42
VII Zw 403	PGC 35286, UGC 6456	4.4	22,23	-14.3	1.11	0.52 ± 0.02	0.02	-1.71 ± 0.01	-1.67 ± 0.01	7.7 ± 0.01	25

^aSelected alternate identifications obtained from NED.

^bReference for the distance to the galaxy. If no reference is given, the distance was determined from the galaxy's radial velocity, given by de Vaucouleurs et al. (1991), corrected for infall to the Virgo Cluster (Mould et al. 2006) and a Hubble constant of $73 \text{ km s}^{-1} \text{ Mpc}^{-1}$.

^c R_H is the Holmberg radius, the radius of the galaxy at a B -band isophote, corrected for reddening, of $26.7 \text{ mag arcsec}^{-2}$. R_D is the disk scale length measured from V -band images. (Table from Hunter & Elmegreen 2004).

^dForeground reddening from Burstein & Heiles (1984).

^e $\text{SFR}_D^{H\alpha}$ is the SF rate, measured from $H\alpha$, normalized to the area πR_D^2 , where R_D is the disk scale length (Hunter & Elmegreen 2004). SFR_D^{FUV} is the SF rate determined from *GALEX* FUV fluxes (Hunter et al. 2003) and an update of the *GALEX* FUV photometry to the GR4/GR5 pipeline reduction).

^fValues in parentheses were determined from the empirical relationship between oxygen abundance and M_B given by Richer & McCall (1995) and are particularly uncertain.

[§]Reference for the oxygen abundance.

References. — (1) Dalcanton et al. 2009; (2) Karachentsev et al. 2004; (3) Karachentsev et al. 2003a; (4) Karachentsev et al. 2006; (5) Dolphin et al. 2002; (6) Sakai et al. 2004; (7) Dolphin et al. 2003; (8) Karachentsev et al. 2003b; (9) Tolstoy et al. 1995a; (10) Karachentsev et al. 2002; (11) Meschin et al. 2009; (12) Sakai et al. 1999; (13) Pietrzynski et al. 2006; (14) Miller et al. 2001; (15) Freedman et al. 2001; (16) Grocholski et al. 2008; (17) Tolstoy et al. 1995b; (18) Gieren et al. 2006; (19) Momany et al. 2002; (20) Gieren et al. 2008; (21) Schulte-Ladbeck et al. 2001; (22) Lynds et al. 1998; (23) Méndez et al. 2002; (24) van Zee & Haynes 2006; (25) Hunter & Hoffman 1999; (26) Skillman, Kennicutt, & Hodge 1989; (27) Moustakas et al. 2010; (28) Richer & McCall 1995; (29) van Zee et al. 2006; (30) Kniazev et al. 2005; (31) Croxall et al. 2009; (32) Lee et al. 2003b; (33) Skillman et al. 1997; (34) Lequex et al. 1979; (35) Lee et al. 2003a; (36) Kobulnicky & Skillman 1997; (37) González-Delgado et al. 1994; (38) Moustakas & Kennicutt (2006); (39) Masegosa et al. 1991; (40) Lee et al. 2005; (41) Viallefond & Thuan 1983; (42) González-Riestra et al. 1988.

2. Observations and Data Reduction

2.1. Observations

The LITTLE THINGS sample consists of 40 gas-rich dwarf galaxies all within 11 Mpc (refer to Hunter et al. 2012, for sample details). In general, the sample spans 4 dex in both SFR and gas mass, and a factor of 50 in metallicity.

Observations (Project ID: 12A-234) were taken in 9 observing runs between March and May of 2012 with the NRAO JVLA. Following the culmination of upgrades to the WIDAR correlator in January 2012, the new C -band receivers provided 2 GHz bandwidth coverage, which we split into two intermediate frequencies (IFs) of width 1 GHz, each IF at full polarisation. Each IF holds 8 spectral windows which, in turn, contain 64 channels of width 2 MHz. To optimise coverage in the (u, v) plane, we placed the centres of each IF near the extremities of the u and frequency coverage (i.e., at 5 and 7.4 GHz), and observed our targets in hourly stints of 10–14 minutes, with the objective of gaining a total of 40–50 minutes on-source integration time. Given the intrinsically faint nature of dwarf galaxies and the desire to obtain a resolved picture of the RC, we opted for the JVLA to be arranged in C -configuration, as this was the setup which would give the best compromise between resolution and surface brightness sensitivity. For a typical observation of duration 1 hour, the 27 antennae of the JVLA at C -band generate a theoretical synthesised beam of width 3 arcsec at half maximum and an rms noise of $5\text{--}6 \mu\text{Jy beam}^{-1}$ when `robust=0.0` weighting is used³.

2.2. Calibration and imaging

We calibrated the data using the Common Astronomy Software Applications (CASA) package, not straying too far from the tutorial of 3C 391 which can be found on the CASA homepage⁴.

2.2.1. Flagging and calibration

Before calibration was started, we used two recently developed automatic flagging algorithms, namely `tflagdata:tfcrop` (Offringa et al. 2010,

2012; implemented into CASA by Rau & Cornwell 2011) and `tflagdata:rflag` (based on AIPS; Greisen, 2011), to automatically flag bad visibilities. The `tfcrop` algorithm works by splitting each baseline into ‘chunks’ along the frequency-domain (each channel) and time-domain (every 50 seconds). The amplitude of all visibilities within a given chunk were averaged and then any chunks that exhibited an amplitude greater than $4\sigma_{\text{pre}}$ from the mean were flagged. Here, σ_{pre} refers to the pre-calibration dispersion of amplitudes around the mean. We opted for a high threshold value as, at this point, we were only concerned with removing extremely high-amplitude data such that subsequent steps in the calibration would not be affected. Rogue baselines, scans and channels, as well as wide-band radio frequency interference (RFI) were generally caught by the algorithm although the measurement sets were manually checked as well to catch any discrepant visibilities missed by the program.

We proceeded with the usual calibration steps by using one of four NRAO calibrators to calibrate the flux scale, and a nearby ($< 10^\circ$) calibrator to correct the complex gain on timescales of around 10 minutes (see Table 2).

Once calibration was completed, the measurement set was inspected a final time for low-level RFI. First, a manual check was performed to flag baselines, scans, or channels that exhibited deviant amplitudes or phases. In addition to this, a second round of automated flagging was performed (this time designed to catch chunks greater than $3.5\sigma_{\text{post}}$ from the mean). Here, σ_{post} refers to the post-calibration dispersion of amplitudes around the mean. This flagging on the calibrated data often reduced the rms noise in subsequent imaging by a further $\sim 10\%$ (compared to when this second round of flagging was omitted).

2.2.2. Radio Continuum imaging

An initial image was created to ascertain the rms background level and the spatial scales of RC emission. Following this, the science quality image was created.

We generated images of our targets by means of `clean`, using the Multi-Scale, Multi-Frequency Synthesis (MS-MFS) algorithm as developed by Rau & Cornwell (2011). Since the (u, v) plane

³Calculated from the official VLA Exposure Calculator (obs.vla.nrao.edu/ect/)

⁴http://casaguides.nrao.edu/index.php?title=EVLA_Continuum_Tutorial_3C391

TABLE 2
C-BAND OBSERVATION AND IMAGING PROPERTIES OF LITTLE THINGS

Galaxy	Observation			Imaging					
	Date	Flux Cal.	Gain Cal.	Phase Centre		Scale	Res.	Noise	Notes
	Name (1)	Name (3)	Name (4)	R.A. (5)	Dec. (6)	pc arcsec ⁻¹ (7)	arcsec (8)	$\mu\text{Jy beam}^{-1}$ (9)	(10)
CVn I dwA	17 Mar 2012	3C286	J1310+3220	12 38 40.2	+32 45 40.0	6.3	3.0 × 3.0	4.3	R
DDO 43	22 Mar 2012	3C286	J0818+4222	07 28 17.8	+40 46 13.0	8.5	2.5 × 2.3	6.9	S
DDO 46	22 Mar 2012	3C286	J0818+4222	07 41 26.6	+40 06 39.0	8.5	3.0 × 2.8	5.1	R
DDO 47	20 Mar 2012	3C286	J0738+1742	07 41 55.3	+16 48 08.0	8.0	3.2 × 3.0	5.0	R
DDO 50	17 Mar 2012	3C147	J0841+7053	08 19 08.7	+70 43 25.0	5.2	3.1 × 2.4	6.1	S
DDO 52	22 Mar 2012	3C286	J0818+4222	08 28 28.5	+41 51 21.0	9.3	2.2 × 2.0	8.3	S
DDO 53	16 Mar 2012	3C147	J0841+7053	08 34 08.0	+66 30 37.0	5.6	2.8 × 2.2	6.5	
DDO 63	25 Mar 2012	3C286	J0841+7053	09 40 30.4	+71 11 02.0	5.9	5.1 × 2.8	5.0	R
DDO 69	20 Mar 2012	3C286	J0956+2515	09 59 25.0	+30 44 42.0	1.2	2.7 × 2.5	5.9	
DDO 70	20 Mar 2012	3C286	J0925+0019	10 00 00.9	+05 19 50.0	2.0	3.1 × 2.6	6.3	
DDO 75	20 Mar 2012	3C286	J1024-0052	10 10 59.2	-04 41 56.0	2.0	3.3 × 2.4	9.7	S
DDO 87	25 Mar 2012	3C286	J1048+7143	10 49 34.7	+65 31 46.0	10.3	3.8 × 2.2	6.2	
DDO 101	17 Mar 2012	3C286	J1221+2813	11 55 39.4	+31 31 08.0	13.9	3.1 × 3.0	15.1	S,P
DDO 126	05 Apr 2012	3C286	J1215+3448	12 27 06.5	+37 08 23.0	7.6	2.9 × 2.4	6.9	S
DDO 133	17 Mar 2012	3C286	J1310+3220	12 32 55.4	+31 32 14.0	9.4	3.2 × 3.2	4.9	R,S
DDO 154	17 Mar 2012	3C286	J1310+3220	12 54 06.2	+27 09 02.0	6.6	2.2 × 2.2	7.3	
DDO 155	17 Mar 2012	3C286	J1309+1154	12 58 39.8	+14 13 10.0	3.4	2.6 × 2.5	6.4	
DDO 165	25 Mar 2012	3C286	J1313+6735	13 06 25.3	+67 42 25.0	7.4	3.7 × 2.8	4.5	R
DDO 167	20 Apr 2012	3C286	J1327+4326	13 13 22.9	+46 19 11.0	6.5	3.3 × 3.0	5.1	
DDO 168	20 Apr 2012	3C286	J1327+4326	13 14 27.2	+45 55 46.0	5.4	2.6 × 2.4	6.0	
DDO 187	17 Mar 2012	3C286	J1407+2827	14 15 56.7	+23 03 19.0	3.9	2.7 × 2.5	6.9	R,S
DDO 210	19 May 2012	3C48	J2047-1639	20 46 52.0	-12 50 51.0	1.4	3.1 × 1.7	4.6	R
DDO 216	31 Mar 2012	3C48	J2253+1608	23 28 35.0	+14 44 30.0	1.4	3.1 × 2.9	5.1	R
F564-V03	20 Mar 2012	3C286	J0854+2006	09 02 53.9	+20 04 29.0	9.6	3.3 × 3.0	5.4	
Haro 29	20 Apr 2012	3C286	J219+484	12 26 16.7	+48 29 38.0	8.3	2.6 × 2.4	6.1	
Haro 36	20 Apr 2012	3C286	J219+484	12 46 56.3	+51 36 48.0	13.9	2.7 × 2.5	6.7	
IC 1613	31 Mar 2012	3C48	J0108+0135	01 05 02.5	+02 09 00.0	1.1	3.9 × 3.7	6.1	
IC 10	28 Apr 2012	3C84	J0102+5824	00 20 17.3	+59 18 14.0	1.5	2.6 × 2.3	7.8	
LGS 3	31 Mar 2012	3C48	J0112+2244	01 03 55.2	+21 52 39.0	0.9	3.0 × 2.8	5.5	R
M81 dwA	17 Mar 2012	3C147	J0841+7053	08 23 57.2	+71 01 51.0	5.6	2.7 × 1.9	10.8	S,P
Mrk 178	20 Apr 2012	3C286	J219+484	11 33 29.0	+49 14 24.0	6.0	2.6 × 2.5	6.5	
NGC 1569	16 Mar 2012	3C147	J0449+6332	04 30 49.8	+64 50 51.0	3.9	2.7 × 2.3	6.8	
NGC 2366	16 Mar 2012	3C147	J0841+7053	07 28 48.8	+69 12 22.0	4.9	2.9 × 2.3	6.5	
NGC 3738	20 Apr 2012	3C286	J1146+5356	11 35 49.0	+54 31 23.0	7.6	2.5 × 2.5	7.6	S
NGC 4163	05 Apr 2012	3C286	J1215+3448	12 12 09.2	+36 10 13.0	4.3	3.3 × 2.9	4.5	R
NGC 4214	05 Apr 2012	3C286	J1215+3448	12 15 39.2	+36 19 38.0	4.5	2.9 × 2.4	7.2	S
Sag DIG	19 May 2012	3C48	J1911-2006	19 30 00.6	-17 40 56.0	1.7	3.5 × 1.4	8.2	
UGC 8508	20 Apr 2012	3C286	J1349+5341	13 30 44.9	+54 54 29.0	4.0	2.6 × 2.5	6.0	
VII Zw 403	25 Mar 2012	3C286	J1153+8058	11 27 58.2	+78 59 39.0	6.8	3.6 × 2.2	6.3	
WLM	19 May 2012	3C48	J2348-1631	00 01 59.2	-15 27 41.0	1.5	5.0 × 1.5	5.3	R

NOTE.—Column 1: Name of dwarf galaxy observed; Column 2: Date of observation; Column 3: Name of flux calibrator; Column 4: Name of complex gain calibrator; Column 5: Phase centre of observation (dwarf galaxy); Column 6: Scale of image (parsecs per arcsecond); Column 7: Resolution of image. Note that some images were made using `robust=0.0` and others using `robust=0.5` where CASA robust values range between -2 (uniform weighting) and $+2$ (natural weighting); Column 9: The rms background level in the centre of the map prior to correction for primary beam attenuation; Column 10: Comments regarding deviations from the typical imaging process.

^RThis galaxy has been cleaned with `clean:robust=0.5` instead of `0.0`.

^SSelf-calibration was performed on this observation to minimise effects of artefacts from sources that exceeded a flux density of ~ 10 mJy.

^PThe resulting image suffered greatly from a nearby background source of ~ 0.1 Jy. Self-calibration failed due to the time varying primary beam, and so to minimise the effect of the offending source, about a quarter of the bandwidth was used in such a way as to place the offending source as near as possible to the first null of the primary beam.

is naturally dominated by short baselines, images were cleaned using Briggs’ method (`robust=0.0`). This cleans the image by weighting each point on the (u,v) plane by its uv -distance. This ensures that the image is not dominated by large scale emission from the more numerous short baselines. This method improves the resolution and results in a synthesised beam that more closely resembles a Gaussian shape, at the expense however of a slight ($\sim 20\%$) increase of the rms noise to $5\text{--}6\ \mu\text{Jy beam}^{-1}$.

Typical rms noise values in the cleaned images fell between $6\text{--}8\ \mu\text{Jy beam}^{-1}$ in close agreement with theoretical values.

For those targets where a detection was tentative or non-existent, images were generated using an approach closer to natural weighting (`robust=0.5`; note that robust values in CASA range between -2 for uniform weighting, and $+2$ for natural weighting). This approach was taken for observations where the signal-to-noise ratio (S/N) was low (12 of the 40 observations), which were: CVnIDwA, DDO 46, DDO 47, DDO 63, DDO 133, DDO 165, DDO 187, DDO 210, DDO 216, LGS 3, NGC 4163, and WLM and are marked in Table 2. Natural weighting allows all the signal captured by the interferometer to be used to its full potential, at the expense of creating a non-Gaussian synthesised beam. Typical rms noise values fell between $4.5\text{--}6.0\ \mu\text{Jy beam}^{-1}$ —a significant improvement compared to using `robust=0.0`—but besides these images having a lower resolution, any low level features (e.g., artefacts from nearby bright sources; RFI) were more prominent.

Self-calibration (phase only) was performed on 11 of our 40 observations to improve the dynamic range across the image and to minimise effects of sidelobes from bright sources. In only one case, (NGC 4214) the emission originating from the galaxy itself produced strong enough artefacts to warrant self-calibration; in all other cases, the offending source was an unresolved background object. The affected galaxies were: DDO 43, DDO 50, DDO 52, DDO 75, DDO 101, DDO 126, DDO 133, DDO 187, M81DwA, NGC 3738, and NGC 4214 and are marked in Table 2.

Two observations (DDO 101 and M81DwA; again marked in Table 2) harboured the strongest background sources in our survey (flux density of

$> 0.1\ \text{Jy}$ located approximately $9'$ and $6'$ from the observation’s phase centre, respectively). Self-calibration was not successful in improving the dynamic range. This was attributed to the fact that both offending sources resided near the edge of the primary beam and, due to the antennae operating on an alt-az mount, these sources (the primary beam has a FWHM of $10'$ at $4.5\ \text{GHz}$ and $5.7'$ at $7.9\ \text{GHz}$) show a time-varying signal due to the source passing through the sidelobes of the primary beam. The result is that the MS-MFS clean algorithm cannot successfully remove the sidelobes of the confusing source. Since these sources are not of interest to the current paper, and the fact that they lie beyond the full-width half-maximum (FWHM) of the primary beam anyway, we decided to select solely the spectral windows least affected by the offending background source, i.e., by choosing 2 or 3 spectral windows for which the offending source was located close to the first null of the primary beam. In doing this, the rms noise was approximately doubled to $15\ \mu\text{Jy beam}^{-1}$ while the side lobes of the confusing source are considerably suppressed. We note that in an earlier study, Stil & Israel (2002) do not list an RC flux density for DDO 101 for the same reason.

We maintained as much consistency as possible by using the same calibration and imaging pipeline for all observations. Inevitably, deviations from our pipeline were needed on a galaxy-by-galaxy basis, and these are summarised in Appendix A. We ended up with good quality images prior to primary beam correction—good quality was defined as having: a flat noise background lacking in structure; no artefacts from nearby strong ($> 0.5\ \text{mJy}$) sources; and all genuine emission successfully modeled (i.e., residual maps comprise a Gaussian distribution of beams consistent with pure noise—average of 0 and variance of σ). Most images indeed possessed a flat background, free of artefacts except CVnIDwA, DDO 52, DDO 75, DDO 165, DDO 187, DDO 210, NGC 3738, and WLM. We checked that all emission was retrieved by looking for a negative bowl. We found that all our images had a flat background bar NGC 1569 and NGC 4214.

We corrected our image for primary beam attenuation where we disregarded any parts of the image below 40% of the primary beam maximum.

2.3. Ancillary data

The LITTLE THINGS project has been highly successful in acquiring a plethora of spatially resolved data on 40 dwarf galaxies. Our RC images are complemented by broadband continuum images including: *GALEX* FUV (1350–1750 Å; effective wavelength 1516 Å; 4'' FWHM), *Spitzer* MIR (effective wavelength 24μm; 6'' FWHM) and FIR (effective wavelength 70μm; 17''.5 FWHM), and H α line emission (see Hunter et al. 2012; Zhang et al. 2012, for details of the ancillary data).

The H α data has been continuum subtracted and corrected for [FUV] contribution. Hunter et al. (2012) used Burstein & Heiles (1982) values to correct H α and FUV maps for foreground reddening. Internal extinction can generally be neglected due to the fact that these dwarfs are low-metallicity and consequently their dust-to-gas ratio is reduced with respect to spirals (Ficut-Vicas et al. in prep.), although it can be important in some of the more actively star forming dwarfs.

The *GALEX* FUV maps were calibrated by the GR4/5 pipeline (except DDO 165 and NGC 4214 which have been processed through the GR6 pipeline). The images have been sky subtracted and were geometrically transformed to match the optical *V*-band orientation. Due to bright foreground stars, IC 10 and UGC 8508 were not observed. For surface brightness measurements, and hence for extended emission, the estimated uncertainty for the *GALEX* FUV maps is 0.15 mag (Gil de Paz et al. 2007).

The *Spitzer* 24 and 70μm maps have been taken from either the Local Volume Legacy (LVL) survey (see Dale et al. 2009, for details) or *Spitzer* Infrared Nearby Galaxies Survey (SINGS). In summary, a pixel-dependent background subtraction was performed and images were convolved with a custom kernel to make a near Gaussian PSF. For the *Spitzer* 24μm maps, the photometric uncertainty is 2% for both unresolved sources and extended emission (Engelbracht et al. 2007).

3. Results

3.1. Radio Continuum images

All radio continuum flux density maps of the LITTLE THINGS sample presented here are available in the online version of this paper (see Appendix B). We provide, as an example, maps of DDO 50 in Figure 1 and show RC flux density contours superposed on ancillary LITTLE THINGS images (Hunter et al. 2012). As the dwarf galaxies are faint, extended RC emission does not show well when plotting contours at the native resolution. Therefore, for the lowest surface brightness contour, we smooth the RC image with a Gaussian kernel up to 2.5 times the native resolution, and use a contour level of $2.5\sigma_{\text{smooth}}$ where σ_{smooth} is the rms noise in the smoothed map. The remaining contours are drawn at $(2 + 2^n)\sigma_{\text{native}}$, where σ_{native} is the rms noise in the original maps (i.e., before smoothing) and $n \geq 0$. The images include H α , FUV, and *Spitzer* 24 and 70μm images.

3.2. Integrated emission from the disk

The integrated emission was taken from the disk of each dwarf galaxy. The disk radius and orientation was defined based the Holmberg disk (where the semi-major and semi-minor axes are defined as the radius `radius` where the B -band surface brightness falls to 26.66 mag), or, if the B -band data was not available, 3 times the V -band scale length (Hunter & Elmegreen 2006).

3.2.1. Masking out emission not related to the target object

Contamination by background sources in the RC is an issue since their emission is often brighter than or similar to the emission originating from the dwarf. Our resolved maps, which typically have resolution elements of $\sim 3''$, made it possible to remove the effects of contamination by singling out emission that was not related to galactic emission. Low resolution observations reported in the literature are predominantly single dish and will have suffered from contamination to varying degrees.

We identified significant RC emission by inspecting each field by eye, and classifying features in a manner similar to Chomiuk & Wilcots (2009)—attributing the flux as originating from: 1) the dwarf galaxy (exactly coincident with a SF tracer), 2) a background galaxy (e.g., see Padovani 2011, for a discussion on the importance of normal star-forming galaxies on the micro-Jansky RC population), 3) ambiguous emission of unknown origin (i.e., unable to discern between a) background origin, or b) non-thermal emission from unresolved SNRs or diffuse non-thermal emission). As an example, we show DDO 133 in Figure 2 along with the classification attributed to each source of RC emission.

RC emission originating from the same line-of-sight as H II regions was assumed to originate from the dwarf galaxy. The FWHM width of the filter used for the $H\alpha$ observations was 30 \AA centred on 6562.8 \AA (Hunter & Elmegreen 2004), meaning that the observed emission in galaxies receding or approaching at greater than $\sim 700 \text{ km s}^{-1}$ would be missed. All galaxies in our sample have heliocentric velocities and rotational speeds well below this value (Hunter et al. 2012), and so all observed $H\alpha$ emission must be from the dwarf galaxy.

To discern background galaxies and ambiguous emission (points 2 and 3), we used our RC images (RC_{NTH} where possible), and then applied the following procedures to determine which sources likely did not belong to our dwarf galaxy:

Isolating obvious background galaxies Background galaxies and SNRs look similar when unresolved, however SNRs are not expected to be very far from SF regions. This is because the stellar velocity dispersion in dwarf galaxies is $\gtrsim 7 \text{ km s}^{-1}$ (Mateo 1998, measures $\gtrsim 7 \text{ km s}^{-1}$, while Marín et al. 2007, find dispersions as low as 4 km s^{-1}) and is even lower for the population of high mass stars (i.e., the core-collapse supernova progenitors) since these generally sink to the bottom of gravitational potentials. Thus, we take 5 km s^{-1} as the stellar velocity dispersion for the stars that will eventually lead to the injection of CRe (and thus RC_{NTH} emission). Given that a SNe progenitor may live up to 50 Myr, we defined a maximum projected distance from obvious SFR regions (5σ FUV or $H\alpha$ emission—preferably FUV since it was the more sensitive) in which RC_{NTH} emission (e.g., SNRs) could exist—this was 250 pc or $10''$ for a face-on galaxy at a distance of 5 Mpc.

Any significant RC source, unresolved or extended, that was outside this region was marked as a background source and was removed by placing a mask over the source. Most images were made using `robust=0.0` which makes the synthesised beam Gaussian-like. For a Gaussian form, 99% of the power of an unresolved source is contained within $3 \times FWHM_{\text{native}}$. This was the size of the mask placed over the background source. Even for a strong background source (e.g., 1 mJy), this removal technique leaves at most $10 \mu\text{Jy}$ unmasked in the image, whilst not masking out too much of the dwarf galaxy.

Cross-matching with line-of-sight optical counterparts We manually cross matched unresolved sources of RC emission with the NASA/IPAC Extragalactic Database⁵ (NED). If an archived galaxy was found within $2''$ (approximately half the FWHM of the synthesised beam at the native resolution) of the unresolved RC

⁵<http://ned.ipac.caltech.edu/forms/nearposn.html>

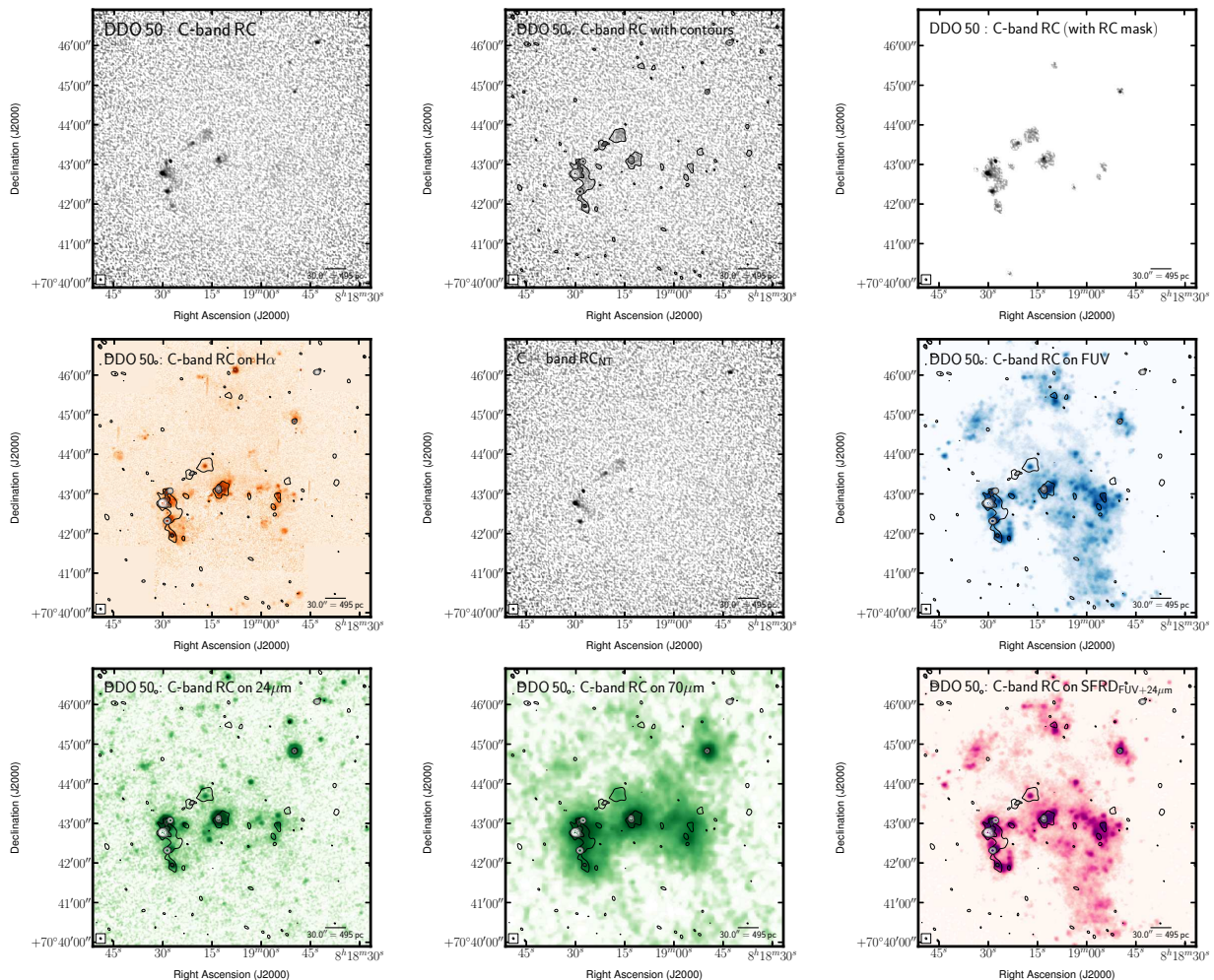


Fig. 1.— Multi-wavelength coverage of DDO 50 displaying a $7' \times 7'$ area. We show total RC flux density at the native resolution (top left) and again with contours (top centre). The lowest contour highlights low-surface brightness emission at a level of $21.9 \mu\text{Jy beam}^{-1}$ —this is 2.5 times the rms after smoothing the native image by a factor of 2.5. The other contours are placed following $(2 + 2^n)\sigma_{\text{native}}$, where $n \geq 0$ and both the rms ($\sigma_{\text{native}} = 6.11 \mu\text{Jy beam}^{-1}$) and the resolution ($\text{FWHM}_{\text{native}} = 3.1 \times 2.4$ arcsec) are taken from the native resolution image. These same contours are also superposed on ancillary LITTLE THINGS images where possible: $\text{H}\alpha$ (middle left); RC_{NTh} inferred from Deeg et al. 1997 (middle centre); *GALEX* FUV (middle right); *Spitzer* $24 \mu\text{m}$ (bottom left); *Spitzer* $70 \mu\text{m}$ (bottom centre); FUV+ $24 \mu\text{m}$ -inferred Σ_{SFR} from Leroy et al. 2012 (bottom right). We also show the RC that was isolated by the RC-based masking technique (top right). The greyscale intensity scales used are arbitrary to best highlight structure.

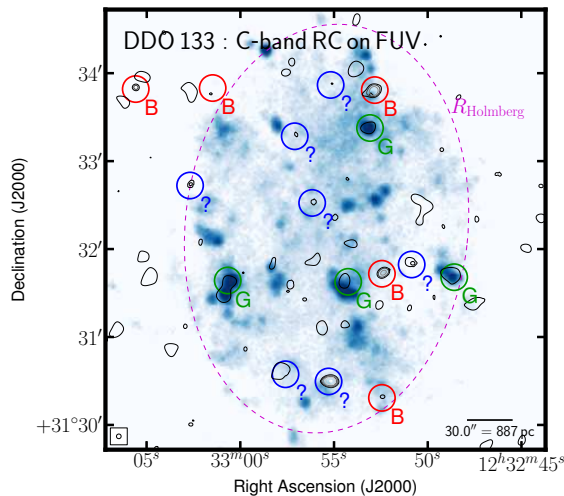


Fig. 2.— *GALEX* FUV emission of DDO 133 overlaid by our RC contours. Our procedures allowed us to attribute RC emission as being from: the galaxy itself (G; green); a background galaxy (B; red); an unknown or ambiguous source (?; Blue). We also overlay the optical disk size (defined by the Holmberg radius; purple).

source, we characterised that source as being a background galaxy.

‘Ambiguous’ sources After cross matching with NED, there remained sources that we could not attribute as coming from a background galaxy, but at the same time were not close enough to a SF site to be confidently classified as originating from the target galaxy; we refer to these sources of RC emission as ‘ambiguous’. To illustrate our definition of ‘ambiguous’ RC emission, we present four of our observations that contained such a source in Figure 3; we show DDO 46 and DDO 63 that each contained a strong unresolved source, and also DDO 69 and IC 1613 that each contained significant extended emission.

Most observations contained an ‘ambiguous’ source; none of these had a non-thermal luminosity that exceeded that of a known bright SNR ($1 \times 10^{19} \text{ W Hz}^{-1}$ or 3.3 mJy at 5 Mpc at 6 GHz), and so may indeed be SNRs.

This was based on SNR N4449-12 in the dwarf galaxy NGC 4449 having $S_{6\text{cm}} = 4.84 \text{ mJy}$ and $\alpha = -0.7$ between 20 cm and 6 cm at a distance of 4.2 Mpc in 2002 (Chomiuk & Wilcots 2009). For comparison, this is 10 times the luminosity of Cas A. Since the luminosity terminally declines

for the majority of the SNR’s lifetime, we treat the observed luminosity of SNR N4449-12 in 2002 as an approximate empirical upper limit to the luminosity of a supernova remnant. We justify our use of SNR N4449-12 as it was the most luminous from a sample of 43 SNRs from 4 irregular galaxies (35 of which are in galaxies that overlap with our sample—namely NGC 1569, NGC 2366, and NGC 4214).

3.2.2. Global quantities (over entire disk)

With background sources removed (see § 3.2.1), emission was integrated from within the dwarf galaxy optical disk (see Table 6 for the disk parameters). The semi-major axis of the disk was based on optical isophotes: using either the Holmberg radius (defined as the isophote where B -band surface brightness drops to a magnitude of 26.66; Hunter & Elmegreen 2006) or 3 times the V -band disk scale length (Hunter & Elmegreen 2006) if the B -band radius was not defined. The major-to-minor axis ratio and position angle were taken from Hunter & Elmegreen (2006). All emission outside this radius was masked. This technique isolates all emission that originates from the galaxy including any low surface brightness emission below our sensitivity limit.

Only $\sim 20\%$ of our RC observations yield a signal-to-noise of greater than 3.

3.3. Optimising the RC signal-to-noise

The majority of galaxies only exhibit significant RC in isolated pockets which is attributed to the episodic nature of SF in dwarf galaxies (e.g., Stinson et al. 2007) combined with the surface brightness sensitivity set by our observations. When integrated over the disk, the signal from most galaxies ends up being dominated by the contribution of noise from the individual beams within the integration area: the uncertainty, δN , is given by $\sigma_{\text{rms}} \sqrt{N}$, where σ_{rms} is the rms noise level and N is the number of individual beams. This motivates the use of masks to isolate genuine emission from background noise (i.e., reduce the integration area which is proportional to N) in order to improve the RC signal-to-noise.

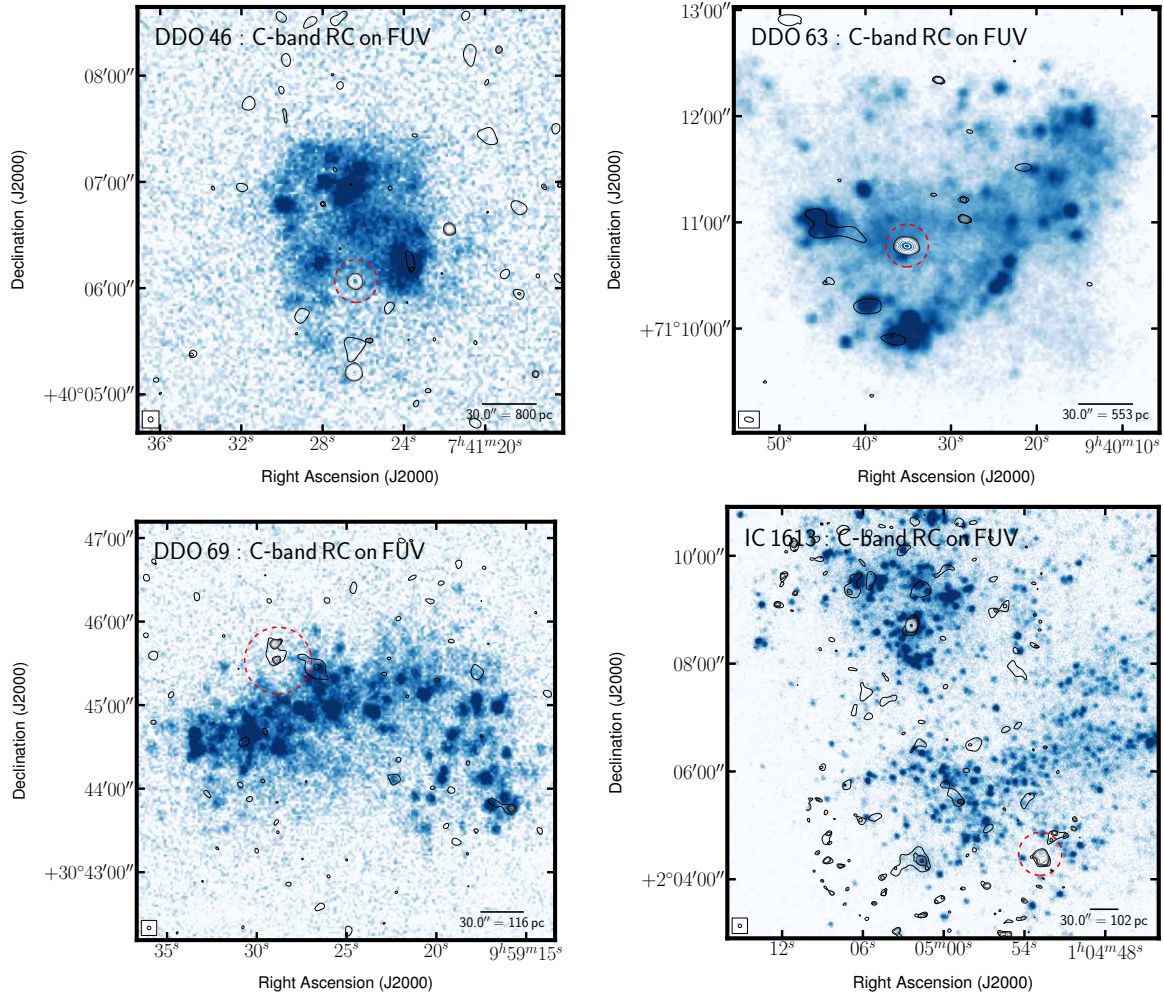


Fig. 3.— Examples of our definition of ‘ambiguous’ emission (red circles). We show DDO 46 and DDO 63 that each contain an unresolved source of 1 mJy (top-left panel) and 1.4 mJy (top-right panel), respectively. We also show DDO 69 and IC 1613 that both contain an extended source (bottom panels). The RC emission could not be attributed as definitely coming from a background galaxy, but at the same time was not close enough to a SF site to be confidently classified as originating from the target galaxy; accordingly, these sources were assigned ‘ambiguous’.

3.3.1. Optimising the RC signal-to-noise

Our resolved maps allow us to single out dwarf emission from background noise, and hence reduce the effects of signal dilution that can plague single dish studies.

Firstly, we note that given a Gaussian distribution of N independent thermal noise peaks, the deviation of the furthest peak from the mean is given by:

$$\sigma_{\max}(\sigma_{\text{rms}}, N) = \sigma_{\text{rms}} \times \sqrt{2} \operatorname{erf}^{-1}\left(1 - \frac{1}{N}\right), \quad (1)$$

where σ_{rms} is the rms of N beams and erf^{-1} is the inverse error function. That is to say, given a population of N independent beams, the probability that a randomly chosen beam is σ_{\max} from the mean is $1/N$. We define σ_{\max} as the most deviant that a ‘noise’ beam can be from the mean—any beams with flux density values higher than this are interpreted as significant. The total number of independent beams ranged between 200 and 20,000 per image, meaning that σ_{\max} ranged between 2.8σ and 4.1σ per image, respectively. Since analysis was performed on images of varying sizes and resolutions, defining σ_{\max} on an image-by-image basis was more robust than using a fixed value for all images as this technique removes subjectivity.

RC-based mask To isolate all unresolved (and strong extended) emission, we defined σ_{\max} in the native resolution image, and defined all pixels with a value greater than σ_{\max} to be significant unresolved (or strong extended) emission; that is to say, the mask was defined as:

$$S_{i,j} = \begin{cases} S_{i,j}, & \text{if } S_{i,j} > \sigma_{\max}(\sigma_{\text{rms}}, N), \\ \text{masked}, & \text{if } S_{i,j} \leq \sigma_{\max}(\sigma_{\text{rms}}, N), \end{cases} \quad (2)$$

where $S_{i,j}$ refers to the surface brightness (Jy beam^{-1}) in the RC image at the pixel coordinate (i, j) .

To catch faint extended emission, we first removed the pixels that exceeded σ_{\max} from the map, and then smoothed the image up to 2.5 times the native resolution. These pixels were removed since a significant point source when smoothed may still appear as significant, even though the area of sky into which we smooth is void of emission. This would detrimentally affect our S/N as we would interpret an unresolved source as originating from a larger area of sky. We define σ_{\max} in

the smoothed image (which is lower than that of the native resolution image since there are fewer independent beams), and define all pixels with a value greater than σ_{\max} to be significant extended emission.

In assuming that the RC background was void of emission (confusion limit not reached), the statistical fluctuations of the background follow a Gaussian distribution centred on zero. Accordingly, so as not to overestimate integrated flux (i.e., by including only positive peaks above our threshold), we also included peaks more negative than the negative threshold in the masked RC image.

For a given galaxy, identical masks were applied to all images (RC; H α ; FUV; 24 μm MIR; 70 μm FIR; SFR density, Σ_{SFR}) to maintain consistency. In all cases, masks (which until now, are based on (i, j) pixel positions) were extended appropriately to mimic the resolution of the image for which it was intended. We extend masks by $\sim 3 \times \text{FWHM}$ to ensure that $\sim 99\%$ of the flux in individual beams was isolated.

Background sources were masked. A mask of size $3 \times \text{FWHM}_{\text{native}}$ is sufficient to remove 99% of the flux from these sources.

As an example, we show the disk-integrated RC emission for a typical dwarf galaxy (DDO 168), and show the improvement we get when we use our masking technique (see Figure 4). When the RC is integrated over the entire disk, it is consistent with noise ($-403 \pm 456 \mu\text{Jy}$); when the RC-based mask is applied, we record a 5σ signal ($374 \pm 68 \mu\text{Jy}$). We note that the isolated RC tends to fall within significant regions of 70 μm emission or SF.

Our method of isolating RC emission is similar to, but more objective than, that employed by Chyży et al. (2011) who integrate emission in their dwarf galaxies by using “polygonal areas encompassing all visible radio emission”.

3.3.2. Global quantities

We used the RC-based mask to extract RC fluxes from the galaxy disk. For all other emission (H α , FUV, 24 μm , 70 μm , SFR), quantities were integrated over the entire galaxy disk without masking. Table 6 lists these integrated quantities.

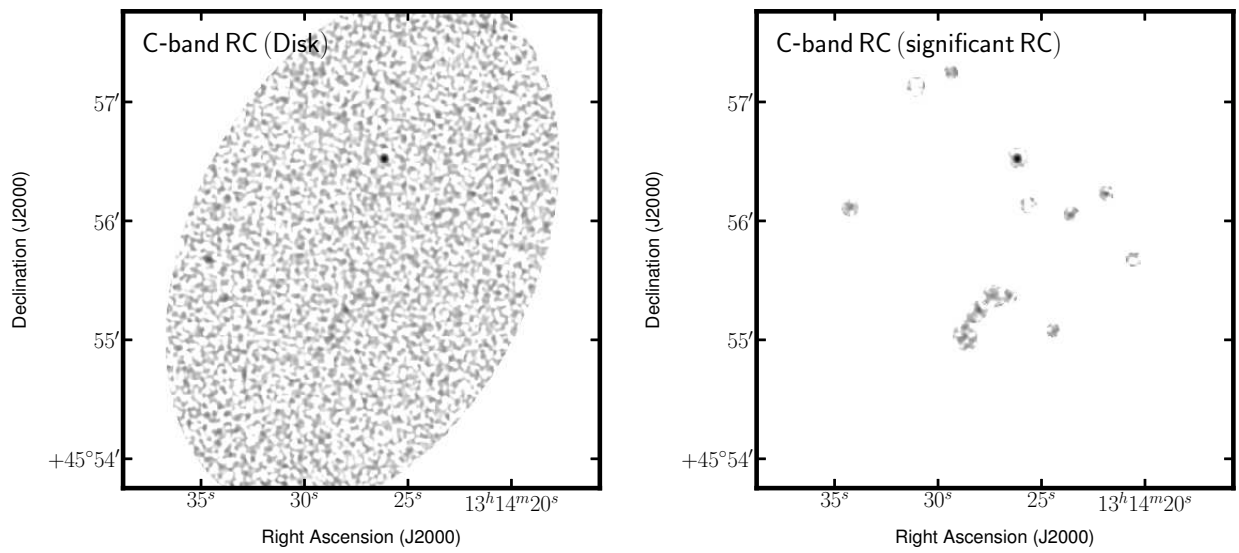


Fig. 4.— Image of RC emission from the disk (left panel) and that isolated using the RC-based masking technique (right panel) for DDO 168. An improvement in precision is gained when using this masking technique. Significant amounts of low surface brightness emission are not masked out.

A total of 26 out of the 40 LITTLE THINGS galaxies exhibit significant RC emission that originates from the dwarf—17 are new RC detections.

The RC-FIR relation traditionally samples the parameter space above FIR luminosities of $\sim 10^{22} \text{ W Hz}^{-1}$; we extend this to lower luminosities by 3 dex. Similarly, studies into the RC-SFR relation do not extend to the values typical of dwarf galaxies (e.g., Heesen et al. in prep.). We extend on their parameter space by 2 dex down to SFRs of $10^{-4} M_{\odot} \text{ year}^{-1}$.

Our aim is to increase our understanding of the RC-SFR and RC-FIR relations of low mass, low metallicity systems. As Figure 5 shows, our data provide the means by which to do so.

4. Discussion

4.1. The Radio Continuum

4.1.1. Comparison with literature flux densities

There are very few significant RC detections of dwarf galaxies in the literature. Of the galaxies that overlap with our sample, the literature is dominated by non-detections (e.g., Altschuler et al. 1984; Wynn-Williams & Becklin 1986; Klein et al. 1992; Höppe et al. 1994). On closer inspection, the seemingly high Klein (1986) detection

rate of 40% is actually dominated by $1-3\sigma$ detections and likely influenced by the unwitting inclusion of background galaxies in the large Effelsberg beam. Therefore, we are very limited by the number of dwarfs with flux densities in the literature which we can confidently compare with. The solid RC detections in the literature mostly come from deeper case-studies of individual dwarf galaxies e.g.;

NGC 1569 Lisenfeld et al. (2004) find a VLA 8.415 GHz flux density of $125 \pm 12 \text{ mJy}$ and spectral index of -0.47 , which makes its equivalent 6.2 GHz flux density $144 \pm 14 \text{ mJy}$ which agrees with ours;

NGC 4214 Kepley et al. (2011) find a VLA 4.86 GHz flux density of $34.0 \pm 6.8 \text{ mJy}$ (D-array) and spectral index of -0.43 , which makes its equivalent 6.2 GHz flux density $30 \pm 6 \text{ mJy}$ which agrees with ours. We note that there is the possibility that we have missed large scale emission;

DDO 50 Dale et al. (2009) find a 20 cm flux density of $20 \pm 3 \text{ mJy}$ and we find a 6.2 GHz flux density of $6.1 \pm 0.1 \text{ mJy}$. This implies a spectral index of -0.83 ± 0.02 which is a reasonable. We note that there is the possibility that we have missed large scale emission;

NGC 3738 Stil & Israel (2002) find a 1.4 GHz flux density of $13 \pm 2 \text{ mJy}$ and we find a 6.2 GHz flux density of $2.9 \pm 0.2 \text{ mJy}$. This implies a spectral index of -1.02 ± 0.04 which is quite high. Our image was strongly affected by artefacts from a nearby bright source, as would have been their image;

Haro 29 Condon et al. (1998) find a 1.4 GHz flux density of $4.5 \pm 0.5 \text{ mJy}$ and we find a 6.2 GHz flux density of $1.7 \pm 0.1 \text{ mJy}$. This implies a spectral index of -0.65 ± 0.08 which is reasonable;

NGC 2366 Condon et al. (2002) find a 1.4 GHz flux density of 19.9 mJy and we find a 6.2 GHz flux density of $11.6 \pm 0.2 \text{ mJy}$. This implies a spectral index of -0.36 ± 0.10 which is reasonable. We note that there is the possibility that we have missed large scale emission which would make the two results more discrepant;



TABLE 3

INTEGRATED EMISSION OVER THE DWARF DISK **SEE END OF DOCUMENT FOR HOW THIS TABLE SHOULD LOOK LIKE**

Galaxy	R.A.	Dec.	Size	P.A.	f_{disk}	C -band RC	$H\alpha$	FUV	$24\mu\text{m}$ MIR	$70\mu\text{m}$ FIR	C -band RC_{NTh}	B_{eq}
(1)	hh mm ss.s	dd mm ss.s	($'$)	($^{\circ}$)	(%)	(mJy)	($10^{-13} \text{ ergs s}^{-1} \text{ cm}^{-2}$)	(mJy)	(10^{-2} Jy)	(10^{-2} Jy)	(mJy)	(μG)
	(2)	(3)	(4)	(5)	(6)	(7)	(8)	(9)	(10)	(11)	(12)	(13)
CVn I dwA	12 38 40.2	+32 45 40	1.7×1.4	80	12	0.12 ± 0.04 (−0.01)	1.95 ± 0.03	0.99 ± 0.02	0.30 ± 0.01	3.58 ± 0.05	0.05 ± 0.04 (−0.01)	< 6
DDO 43	07 28 17.8	+40 46 13	1.8×1.2	6	5	0.28 ± 0.05 (0.00)	1.16 ± 0.02	0.66 ± 0.01	0.25 ± 0.05 (0.00)	10
DDO 46	07 41 26.6	+40 06 39	3.8×3.4	84	6	1.39 ± 0.08 (1.31)	1.00 ± 0.02	1.16 ± 0.01	1.35 ± 0.08 (1.31)	6
DDO 47	07 41 55.3	+16 48 08	4.5×2.3	−79	3	0.35 ± 0.05 (0.09)	2.88 ± 0.02	2.31 ± 0.01	0.32 ± 0.05 (0.09)	7
DDO 50	08 19 08.7	+70 43 25	7.9×5.7	18	3	6.09 ± 0.14 (0.59)	57.32 ± 0.46	32.24 ± 0.15	20.18 ± 0.03	359.90 ± 0.32	3.63 ± 0.14 (0.57)	10
DDO 52	08 28 28.5	+41 51 21	2.2×1.4	4	2	0.11 ± 0.04 (0.00)	0.27 ± 0.01	0.45 ± 0.00	$−0.04 \pm 0.00$	2.05 ± 0.06	0.11 ± 0.04 (0.00)	< 10
DDO 53	08 34 08.0	+66 10 37	2.7×1.4	81	4	0.41 ± 0.05 (0.14)	4.25 ± 0.04	1.99 ± 0.02	2.87 ± 0.00	28.53 ± 0.03	0.25 ± 0.05 (0.13)	8
DDO 63	09 40 30.4	+71 11 02	4.3×4.3	0	6	1.79 ± 0.07 (1.53)	4.12 ± 0.02	3.41 ± 0.02	2.09 ± 0.01	4.32 ± 0.11	1.64 ± 0.07 (1.52)	6
DDO 69	09 59 25.0	+30 44 42	4.8×2.7	−64	3	0.86 ± 0.08 (0.68)	1.66 ± 0.01	4.11 ± 0.02	$−0.75 \pm 0.01$	13.22 ± 0.08	0.85 ± 0.08 (0.68)	9
DDO 70	10 00 00.9	+05 19 50	7.4×4.4	88	2	1.92 ± 0.09 (1.54)	6.09 ± 0.04	9.07 ± 0.05	0.69 ± 0.02	70.15 ± 0.15	1.72 ± 0.09 (1.54)	6
DDO 75	10 10 59.2	−04 41 56	6.2×5.2	42	1	0.73 ± 0.13 (0.28)	43.30 ± 0.10	23.74 ± 0.07	0.31 ± 0.02	102.60 ± 0.25	0.39 ± 0.13 (0.26)	< 9
DDO 87	10 49 34.7	+65 31 46	2.3×1.3	76	8	0.12 ± 0.05 (0.10)	0.67 ± 0.01	0.59 ± 0.01	0.10 ± 0.00	6.78 ± 0.04	0.10 ± 0.05 (0.10)	< 7
DDO 101	11 55 39.4	+31 31 08	2.1×1.5	−69	4	0.00 ± 0.08 (0.00)	0.79 ± 0.01	0.33 ± 0.00	0.27 ± 0.01	$−0.77 \pm 0.04$	0.00 ± 0.08 (0.00)	< 10
DDO 126	12 27 06.5	+37 08 23	3.5×1.7	−41	3	0.31 ± 0.05 (0.00)	3.61 ± 0.04	2.62 ± 0.02	0.37 ± 0.01	17.12 ± 0.06	0.17 ± 0.05 (0.00)	7
DDO 133	12 32 55.4	+31 32 14	4.7×3.2	−6	5	0.68 ± 0.07 (0.52)	4.53 ± 0.04	3.72 ± 0.03	0.78 ± 0.02	35.31 ± 0.20	0.55 ± 0.07 (0.51)	6
DDO 154	12 54 06.2	+27 09 02	3.1×1.6	46	0	$−0.01 \pm 0.01$ (0.00)	2.18 ± 0.02	3.49 ± 0.02	0.29 ± 0.01	3.54 ± 0.05	$−0.01 \pm 0.01$ (0.00)	< 13
DDO 155	12 58 39.8	+14 13 10	1.9×1.3	51	7	0.23 ± 0.05 (0.00)	4.65 ± 0.06	...	0.24 ± 0.01	18.20 ± 0.08	0.04 ± 0.05 (0.00)	< 9
DDO 165	13 06 25.3	+67 42 25	4.3×2.3	89	6	0.16 ± 0.06 (0.01)	1.47 ± 0.01	...	0.05 ± 0.01	7.79 ± 0.06	0.16 ± 0.06 (0.01)	< 5
DDO 167	13 13 22.9	+46 19 11	1.5×1.0	−24	0	0.00 ± 0.00 (0.00)	0.79 ± 0.01	0.97 ± 0.01
DDO 168	13 14 27.2	+45 55 46	4.6×2.9	−25	2	0.37 ± 0.07 (0.11)	5.80 ± 0.03	4.91 ± 0.03	0.80 ± 0.01	44.96 ± 0.14	0.26 ± 0.07 (0.11)	7
DDO 187	14 15 56.7	+23 03 19	2.1×1.7	37	1	$−0.05 \pm 0.03$ (0.00)	0.55 ± 0.01	0.95 ± 0.01	$−0.02 \pm 0.01$	$−2.57 \pm 0.10$	$−0.05 \pm 0.03$ (0.00)	< 10
DDO 210	20 46 52.0	−12 50 50	2.6×1.3	−85	3	0.47 ± 0.03 (0.32)	...	0.53 ± 0.01	$−0.19 \pm 0.01$	6.08 ± 0.04
DDO 216	23 28 35.0	+14 44 30	8.0×3.6	−58	1	$−0.01 \pm 0.04$ (0.05)	0.10 ± 0.01	1.15 ± 0.01	$−0.01 \pm 0.01$	10.73 ± 0.09	$−0.01 \pm 0.04$ (0.05)	< 7
F564-V03	09 02 53.9	+20 04 29	1.3×1.0	7	7	0.06 ± 0.03 (−0.00)	...	0.08 ± 0.00
Haro 29	12 26 16.7	+48 29 38	1.7×1.4	85	17	1.70 ± 0.08 (0.00)	12.95 ± 0.36	8.91 ± 0.24	6.71 ± 0.01	36.08 ± 0.05	0.53 ± 0.08 (0.00)	9
Haro 36	12 46 56.3	+51 36 48	1.5×1.2	90	9	0.22 ± 0.05 (0.00)	2.19 ± 0.02	2.56 ± 0.05	1.07 ± 0.00	26.65 ± 0.06	0.15 ± 0.05 (0.00)	< 8
IC 1613	01 05 00.0	+02 06 55	18.2×14.7	71	17	1.72 ± 0.21 (0.50)	46.28 ± 0.19	54.47 ± 0.27	4.09 ± 0.05	364.30 ± 0.50	1.72 ± 0.21 (0.50)	6
IC 10	00 20 17.5	+59 18 14	11.6×9.1	−38	8	95.69 ± 0.30 (0.00)	90.78 ± 0.44	89.79 ± 0.30 (0.00)	19
LGS 3	01 03 55.2	+21 52 39	1.9×1.0	−3	1	0.02 ± 0.01 (0.00)	...	0.06 ± 0.00
M81 dwA	08 23 57.2	+71 01 51	1.5×1.1	86	1	0.02 ± 0.03 (0.00)	...	0.33 ± 0.00
Mrk 178	11 33 29.0	+49 14 24	2.0×0.9	−51	8	0.42 ± 0.05 (0.00)	0.49 ± 0.01	...	0.51 ± 0.00	0.51 ± 0.00	0.42 ± 0.05 (0.00)	10
NGC 1569	04 30 49.8	+64 50 51	2.3×1.3	−59	100	151.50 ± 0.24 (1.60)	156.70 ± 0.97	2.43 ± 0.04	802.60 ± 3.05	4069.00 ± 3.04	136.70 ± 0.25 (1.60)	24
NGC 2366	07 28 48.8	+69 12 22	9.4×4.0	33	6	11.62 ± 0.19 (0.07)	91.03 ± 1.08	27.69 ± 0.18	74.60 ± 0.02	572.10 ± 0.36	5.04 ± 0.21 (0.06)	9
NGC 3738	11 35 49.0	+54 31 23	4.8×4.8	0	19	2.87 ± 0.15 (0.00)	15.99 ± 0.17	10.31 ± 0.15	13.17 ± 0.01	279.70 ± 0.46	1.71 ± 0.15 (0.00)	10
NGC 4163	12 12 09.2	+36 10 13	2.9×1.9	18	2	0.06 ± 0.02 (0.02)	1.43 ± 0.02	2.27 ± 0.05	0.50 ± 0.01	10.93 ± 0.12	0.06 ± 0.02 (0.02)	< 7
NGC 4214	12 15 39.2	+36 19 38	9.3×8.5	16	6	23.40 ± 0.26 (0.45)	175.60 ± 0.89	68.53 ± 0.35	226.60 ± 0.06	2715.00 ± 1.26	11.57 ± 0.27 (0.77)	12
Sag DIG	19 30 00.6	−17 40 56	4.3×2.3	88	4	0.44 ± 0.11 (0.42)	1.04 ± 0.01	1.65 ± 0.01	0.44 ± 0.11 (0.42)	9
UGC 8508	13 30 44.9	+54 54 29	2.5×1.4	−60	3	0.58 ± 0.04 (0.51)	2.83 ± 0.04	...	0.45 ± 0.01	14.79 ± 0.06	0.53 ± 0.04 (0.50)	10
VIIZw 403	11 27 58.2	+78 59 39	2.2×1.1	−11	16	0.89 ± 0.07 (0.00)	7.06 ± 0.12	2.70 ± 0.05	2.14 ± 2.20	64.66 ± 1.26	0.31 ± 0.07 (0.00)	7
WLM	00 01 59.2	−15 27 41	11.6×5.1	−2	15	2.10 ± 0.20 (0.14)	15.80 ± 0.06	21.59 ± 0.07	4.97 ± 0.01	128.10 ± 0.20	1.41 ± 0.20 (0.14)	5

NOTE.—Column 1: Name of dwarf galaxy ; Columns 2/3: Celestial coordinates (J2000) of centre of optical disk; Column 4/5: Size (major and minor axes) and position angle (P.A.) of optical disk (Hunter & Elmegreen 1999); Column 6: Proportion of the disk isolated by the RC-based masking technique; Column 7: C -band (~ 6 GHz) radio continuum flux density. The RC quantity in parenthesis is the amount that was regarded as ‘ambiguous’; Column 8: $H\alpha$ flux; Column 9: *GALEX* FUV flux density; Column 10: *Spitzer* $24\mu\text{m}$ MIR flux density; Column 11: *Spitzer* $70\mu\text{m}$ FIR flux density; Column 12: C -band (~ 6 GHz) radio continuum non-thermal (synchrotron) flux density. All RC_{NTh} emission is assumed to be synchrotron and is inferred by subtracting the RC_{Th} component from the total RC (Deeg et al. 1997). The quantity in parenthesis is the amount that was regarded as ‘ambiguous’; Column 13: Equipartition magnetic field strength in the plane of the sky (see Equation 3 of Beck & Krause 2005).

^BDisk parameters are derived from the Holmberg radius of B -band images.

^V B -band data was not available, so disk parameters are derived from 3 times the V -band disk scale length.

^LWhen the RC emission was integrated over the entire disk, the S/N did not exceed 3.

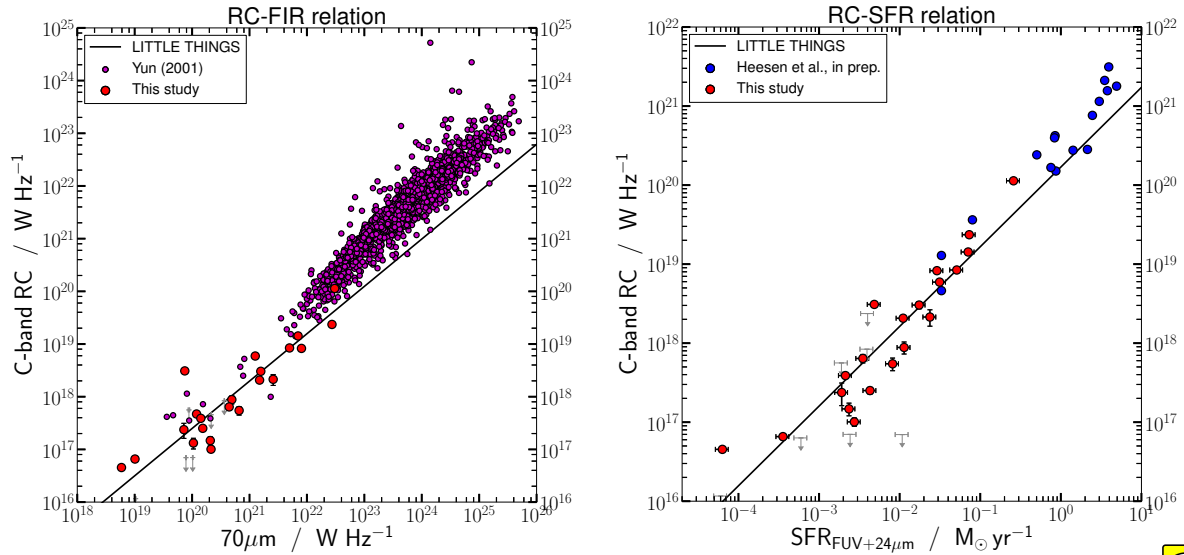


Fig. 5.— Our results in the context of previous studies. We compare our RC and FIR coverage with that of Yun et al. (2001) (left panel). Their VLA 1.4 GHz data have been corrected to 6 GHz and the *IRAS* 60 μm data to *Spitzer* 70 μm . We also compare our RC and SFR coverage with that of Heesen et al. in prep. (right panel). Their WSRT 22 cm data have been corrected to 6 GHz.

Others Klein (1986) find a number of $\sim 4\sigma$ detections at 6.3 GHz: 3.5 ± 1.0 mJy for DDO 126; 4 ± 1 mJy for DDO 133; 9 ± 2 mJy for DDO 52. However, we observe less than a mJy for each of these. In all cases, we find a nearby background galaxies that will have entered their $2'.48$ single dish beam and contributed to their flux density to some degree.

4.1.2. Composition of the radio continuum: Thermal and non-thermal

We assume that, in *C*-band, the total RC emission is comprised of two continua: the RC_{Th} and the RC_{NTh} . Since $\text{H}\alpha$ and the RC_{Th} both have their origins in hot ($\sim 10^4$ K) plasma, a tight spatial correlation between the two emissions is expected (e.g., Deeg et al. 1997; Murphy et al. 2011). The $\text{H}\alpha$ – RC_{Th} relation taken from Deeg et al. (1997) assumes the form:

$$\frac{\text{RC}_{\text{Th}}}{\text{W m}^{-2}} = 1.14 \times 10^{-25} \left(\frac{\nu}{\text{GHz}} \right)^{-0.1} \times \left(\frac{T_e}{10^4 \text{ K}} \right)^{0.34} \frac{F_{\text{H}\alpha}}{\text{ergs s}^{-1} \text{ cm}^{-2}}. \quad (3)$$

On a spatially resolved basis, the RC_{Th} flux density (see Equation 3) can be subtracted from the

total RC, yielding the RC_{NTh} flux density (we assumed an electron temperature of 10^4 K).

After the removal of known background galaxies and ‘ambiguous’ sources, the RC-based mask was used to isolate both RC emission and RC_{NTh} (scaled $\text{H}\alpha$) emission. When weighted by the mass of the galaxy, we find that the average thermal fraction for our sample is $(42 \pm 24)\%$ (upper limit), whilst the non-thermal fraction is $(58 \pm 24)\%$ (lower limit). For comparison, thermal fractions in dwarf galaxies have been quoted as 30% at 1.4 GHz for a sample of stacked faint dwarfs (Roychowdhury & Chengalur 2012), 50% in IC 10 at *C*-band (Heesen et al. 2011), 23% in NGC 1569 at 1.49 GHz (Lisenfeld et al. 2004), and 23% in NGC 4449 at 1.49 GHz (Niklas et al. 1997).

The RC_{NTh} fraction is quoted as a lower limit for two reasons: 1) our masking technique masks out regions that are consistent with noise—it is in these regions where low surface brightness RC_{NTh} is likely to exist, and 2) our interferometric observations may miss extended ($\gtrsim 4'$) emission due to lack of short spacing data— RC_{NTh} naturally diffuses through the ISM and so it is the RC_{NTh} component that is more prone to being missed (H II regions in our dwarf galaxies do not exceed scales of $4'$).

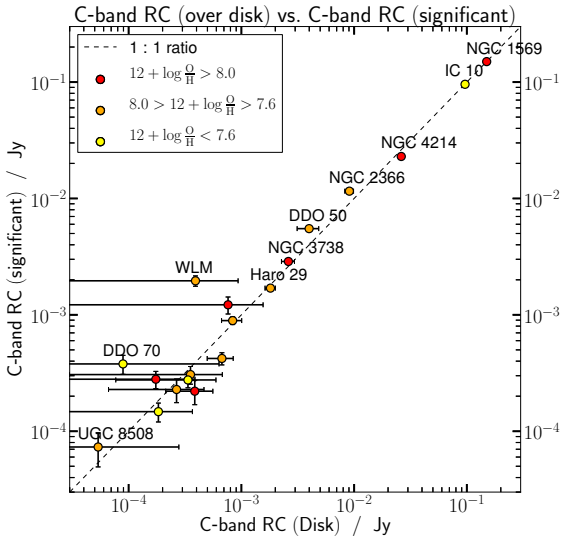


Fig. 6.— Significant amounts of low surface brightness emission are not masked out when using the RC-based mask—for the dwarf galaxies that show significant pockets of RC emission, this amount is consistent with the RC emission when integrated over the entire disk (right panel). Note, however, that uncertainties on disk-integrated quantities are very large.

In dwarf galaxies, the RC emission tied up in SNRs has a low contribution—Chomiuk & Wilcots (2009) find that, at 20 cm, discrete SNRs make up 6% of the non-thermal RC in NGC 1569 and NGC 4449, and 7% of the total RC in NGC 2366.

For a given SFR, the $H\alpha$ and therefore expected RC_{Th} produced is less in dwarf galaxies than in spirals (Lee et al. 2009). Despite this, the thermal fraction is high which implies that the non-thermal continuum too is deficient for the same SFR.

We do not remove any significant amount of low surface brightness RC emission through our masking procedure. For the dwarf galaxies that exhibit significant pockets of RC emission, this amount is consistent with the RC emission when integrated over the entire disk (see Figure 6). We note however, that uncertainties on disk-integrated quantities are very large.

For the more extended dwarf galaxies, RC_{NTh} may be missed due to lack of short spacing data from our interferometric observations. In particular, DDO 50 and NGC 2366 (disk size of 7.9 and 9.4', respectively) exhibit unrealistic non-thermal

fractions. Using the Deeg et al. (1997) $H\alpha$ -to- RC_{Th} conversion factor, we predict the RC_{Th} flux from within the disk of DDO 50 to be 5.4 mJy which exceeds the total C -band RC flux we observe (4.5 ± 0.9 mJy). Similarly, the RC_{Th} flux predicted for NGC 2366 is 8.7 mJy which implies an unrealistically high thermal fraction of 95% given that the total RC flux we observe is 9.2 ± 0.8 mJy.

This is evidence that a lack of short spacing data has led to extended emission being missed. Heesen et al. (2011) encounter similar problems with their VLA observations of the dwarf galaxy IC 10—their C -band C -configuration observations yield 30% less emission than their D -configuration observation, and even their D -configuration observations yield ???% less emission than Effelsberg single-dish observations.

Note that it is not just the RC_{NTh} that is prone to being tied up in diffuse structures. A ‘significant fraction’ of RC_{Th} tied up in ‘a diffuse component or in low-luminosity H II regions’, too (Chomiuk & Wilcots 2009).

4.2. The RC–SFR relation

Using the ancillary data, we are able to measure SFRs and compare them with our RC. We use FUV-inferred SFRs calculated through the Leroy et al. (2012) prescription for three reasons: 1) it corrects the FUV-inferred SFR by any internal dust that obscures the optical emission (which is relevant mostly for our more actively star forming dwarfs), 2) the FUV has been proven to be a reliable SF indicator at low SFR in comparison to $H\alpha$ -inferred SFRs (e.g., Lee et al. 2009; Ficut-Vicas et al. in prep.), and 3) the timescale of RC_{NTh} emission is more similar to FUV-inferred SF timescales than to, e.g., $H\alpha$ -inferred SF timescales. Galactic foreground extinction is taken into account through extinction corrections (see Hunter et al. 2012, for details). To correct for internal extinction, Bigiel et al. (2008) and Leroy et al. (2012) use *Spitzer* 24 μ m dust emission to empirically correct *GALEX* FUV fluxes for the fraction of dust-obscured SF on the assumption that a proportion of energy absorbed by internal dust is reradiated at 24 μ m (this is based on the original idea by Calzetti et al. 2007,

who use H α instead of FUV). They yield:

$$\frac{\Sigma_{\text{SFR}}}{\text{M}_{\odot} \text{ yr}^{-1} \text{ kpc}^{-2}} = 0.081 \frac{I_{\text{FUV}}}{\text{MJy sr}^{-1}} + 0.0032 \frac{I_{24\mu\text{m}}}{\text{MJy sr}^{-1}}. \quad (4)$$

This FUV+24 μm prescription was needed for our more actively forming galaxies and, to maintain consistency, the same prescription has been used on all galaxies.

Figure 7 shows our RC–SFR relation. We used FUV–inferred SFRs and, where *Spitzer* 24 μm was available, corrected for internal dust extinction using the prescription in Equation 4. **For those galaxies where *Spitzer* 24 μm was not available, we used the FUV–inferred SFR without any correction.** The RC–based masking technique was used to isolate the RC signal (see Section 3.3.1) thus providing the best measurement of the integrated RC emission; the FUV–inferred SFR was integrated over the entire galaxy disk. The left panel shows the relation when we include the ‘ambiguous’ RC sources, whereas the right panel shows the relation with ‘ambiguous’ sources removed.

We compare our RC–SFR relation with that derived by Condon et al. (2002) (see their Equation 28). They relate the integrated total RC of an unresolved galaxy to the SFR and find,

$$\frac{L_{6\text{GHz}}}{\text{W Hz}^{-1}} = (4.8 \pm 2.5) \times 10^{20} \frac{\text{SFR}}{\text{M}_{\odot} \text{ yr}^{-1}}. \quad (5)$$

Their relation is derived for high–mass star formation above $5M_{\odot}$, but is extrapolated down to $0.1M_{\odot}$ using a Salpeter stellar IMF. The SFR expressed by the Leroy et al. (2012) prescription is based on a Miller–Scalo stellar IMF however and their derived SFRs are lower than the Salpeter IMF by a factor of 1.59 in the same mass range, so we correct for this. We converted Condon et al. (2002)’s 1.4 GHz luminosity to *C*–band luminosity, $L_{6\text{GHz}}$, using a spectral index of -0.7 . The error (in Equation 5 and the grey band in Figure 7) takes into account the uncertainties of our conversion i.e., an uncertainty in the spectral index of 0.1 and a canonical factor of 2 uncertainty in the SFR (Leroy et al. 2012).

We performed a bivariate linear regression to quantify the relation between the RC luminosity and SFR. We first linearised the data—we took

the log of both the abscissa (RC)– and ordinal (SF indicator)–values assuming the data followed a power law function of the form $y = Ax^n$ or $\log(y) = n \log(x) + c$, where $c = \log(A)$. We used the `odr`⁶ module from `scipy`, which takes four arrays of the data points (the data points: $\log x$ and $\log y$; the 1σ errors in log–space: $\frac{\delta x}{x}$ and $\frac{\delta y}{y}$) and the model function, and works to minimise the squares of the orthogonal distance between data points and the model, ultimately returning best–fit values and their standard deviations. Data points with low significance (less than 3σ) were excluded from the fit as these were the images dominated by noise (including low–level image artefacts, RFI, etc.) and thus susceptible to recording image artefacts as genuine emission.

We find that the RC–SFR relation in Figure 7 (left panel) is not consistent with the Condon et al. (2002) relation—although, we find a linear power–law gradient of $\sim 1.0 \pm 0.1$ with a scatter of 0.24 dex, there is an indication that our galaxies are radio ‘quiet/dim’—for a given SFR, the dwarf galaxies consistently fall approximately a factor of 2 below the Condon et al. (2002) relation. The brightest galaxies are largely consistent with the Condon et al. (2002) RC–SFR relation; the majority of the deviation comes from the dwarf galaxies that have a SFR $\lesssim 2 \times 10^{-2} \text{M}_{\odot} \text{ yr}^{-1}$.

A number of dwarfs in Figure 7 (left panel) are significantly radio ‘bright/loud’ with respect to the rest of our sample. These data points (e.g., DDO 63, DDO 69, and DDO 210) are faint dwarf galaxies dominated by ‘ambiguous’ RC emission. If these ‘ambiguous’ sources are background galaxies that themselves lie on the Condon et al. (2002) RC–SFR relation, then we would infer that the dwarf too lies on the Condon relation. This would have been an important problem in earlier studies (e.g., de Jong et al. 1985): significant contamination from background galaxies (the kind of galaxies on which the RC–SFR is based) made the dwarf galaxies appear to stay true to the RC–SFR relation.

Given that our dwarf galaxies may be affected by contamination from the emission of unrelated background sources, we perform the same analysis but, this time, assuming that the ‘ambiguous’ sources of RC emission are of background origin

⁶<http://www.scipy.org/doc/api.docs/SciPy.odr.odrpack.html>

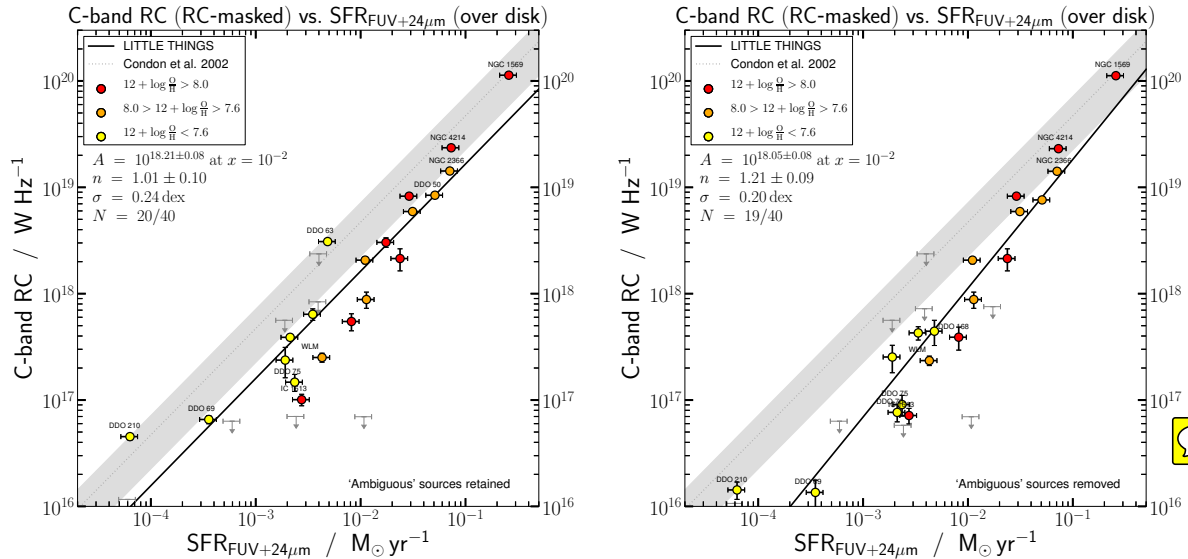


Fig. 7.— Galaxy-wide total C -band luminosity as a function of the FUV-inferred SFR (Leroy et al. 2012); SFRs have been corrected for internal extinction from dust if $24\mu\text{m}$ data was available using the Leroy et al. (2012) prescription. Note that the abscissa and ordinal values were yielded by integrating emission over distinct regions. Definite background sources have been removed, whilst the ‘ambiguous’ sources have been retained (left panel) and removed (right panel). The solid line is the best-fit power law to our sample. We show the Condon et al. (2002) RC–SFR relation as described in Equation 5 including the errors introduced by our conversion (grey shaded band).

and removing them before taking integrated quantities. In doing this, while we may remove, at worst, 10% of genuine RC emission (RC emission from SNRs contribute $< 10\%$ of the total RC in dwarf galaxies; Chomiuk & Wilcots 2009), contamination from background sources will be entirely removed. We present the RC–SFR relation (free from ‘ambiguous’ emission) in Figure 7 (right panel). This ensures that all of the isolated emission is from the dwarf itself, however, it is possible that we remove a fraction of dwarf emission (e.g., a SNR that we erroneously assume is a background galaxy).

We find that removing the ‘ambiguous’ source significantly alters our results—our RC–SFR diverges from the Condon et al. (2002) relation. The divergence starts for systems that have a SFR of about $0.1\text{--}1.0 M_{\odot} \text{yr}^{-1}$ and is characterised by a power-law index of 1.2 ± 0.1 with a scatter of 0.2 dex. Our brightest galaxies remain largely consistent with the Condon et al. (2002) RC–SFR relation, but as we probe lower SFR, the RC luminosity drops at a faster rate—not only are the dwarf galaxies radio ‘quiet/dim’ with respect to the Condon et al. (2002) RC–SFR rela-

tion, but this effect is stronger for lower SFRs—the RC luminosity observed in dwarfs with a SFR of $\sim 1 \times 10^{-3} M_{\odot} \text{yr}^{-1}$ is about a factor of 10 lower than that predicted by the Condon et al. (2002) relation. Interestingly, this is the same factor of 10 that $H\alpha$ -inferred SFRs undercut FUV-inferred SFRs in dwarf galaxies (Lee et al. 2009).

4.2.1. RC_{NTh} –SFR relation

Figure 7 shows our RC_{NTh} –SFR relation. We find a slope of 1.34 ± 0.08 which agrees with the 1.33 predicted for turbulent magnetic field amplification. The RC_{NTh} component is discussed in more detail in Section 4.5.1.

4.3. q -parameter

Yun et al. (2001) found that the log of the ratio of the $IRAS$ FIR (a weighted combination of 60 and $100\mu\text{m}$ flux) to VLA 1.4 GHz flux densities of his sample,

$$q_{\text{FIR:1.4}} = \log \frac{\text{FIR [Jy]}}{\text{RC [Jy]}}, \quad (6)$$

was 2.34 ± 0.01 . To match our own observations, their $q_{\text{FIR:1.4}}$ value is corrected making $q_{70:6} =$

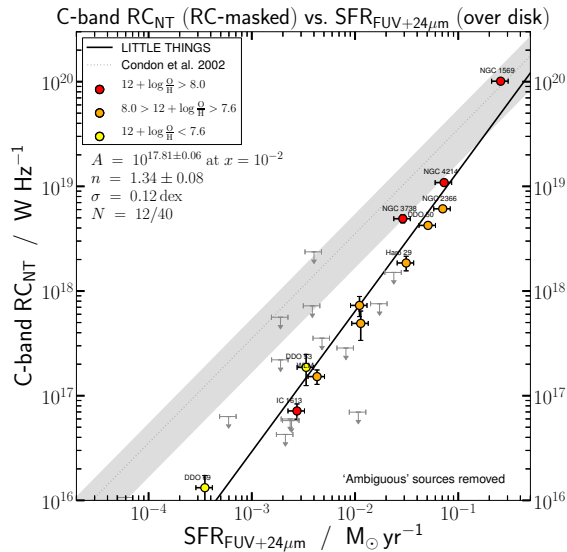


Fig. 8.— Galaxy-wide total C -band RC_{NT} luminosity as a function of the FUV-inferred SFR (Leroy et al. 2012); SFRs have been corrected for internal extinction from dust if $24\mu\text{m}$ data was available using the Leroy et al. (2012) prescription. Note that the abscissa and ordinal values were yielded by integrating emission over distinct regions. Both definite background sources and ‘ambiguous’ sources have been removed. The solid line is the best-fit power law to our sample. We show the Condon et al. (2002) RC-SFR relation as described in Equation 5 corrected by 0.75 (i.e., to represent just the RC_{NT} component) including the errors introduced by our conversion (grey shaded band).

2.68 ± 0.12 , where the subscript 70 : 6 refers to the ratio of $70\mu\text{m}$ FIR to 6 GHz RC. The uncertainty is calculated by assuming a 0.1 error on the spectral index between L - and C -band, and 15 K on the dust temperature. We compare our $q_{70:6}$ values with Yun et al. (2001) in Figure 9.

Figure 9 shows that our low-SFR galaxies ($70\mu\text{m} \lesssim 10^{21}\text{WHz}^{-1}$) may be continuing the trend of the Yun et al. (2001) sample to exhibit high $q_{70:6}$ values; however, our values are not accurate enough to state whether there is a deviation from $q_{70:6} = 2.68$ or whether they are consistent with it. If this is a genuine deviation, then this is further evidence that the RC is deficient for a given SFR (see Section 4.2 where we found evidence that our sample falls below the Condon et al. (2002) RC-SFR relation).

A tendency for dwarf galaxies to exhibit larger $q_{70:6}$ values could be evidence of the subtle difference between the mechanisms for generating RC

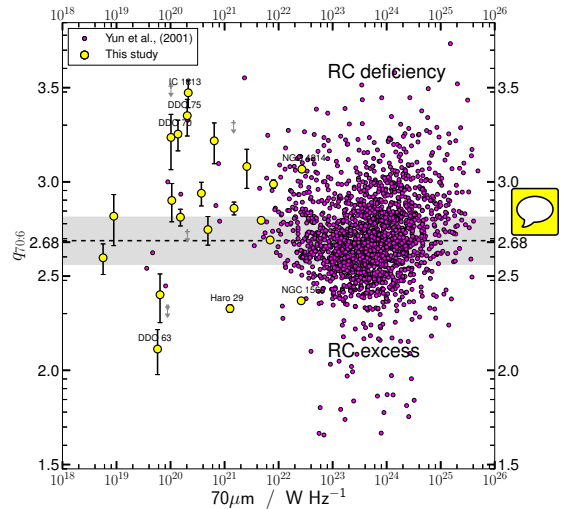


Fig. 9.— $q_{70:6}$ parameter as a function of $70\mu\text{m}$ luminosity. Both obvious and ‘ambiguous’ background sources have been removed. We also show the Yun et al. (2001) data points (purple) and their q -parameter appropriately corrected to our observation bands (dashed) including the errors introduced by our conversion (grey shaded band).

and FIR emission. While RC_{Th} emission is highly dependent on the truncated stellar IMF in dwarfs ($H\alpha$ emission under-predicts SFRs by a factor of 10 in galaxies with a SFR of $\sim 10^{-3}\text{M}_{\odot}\text{yr}^{-1}$; Lee et al. 2009), FIR emission is not as affected since a lower proportion of dust-heating comes from massive stars and, in fact, it is the ISRF that is the main contributor to dust-heating (Irwin et al. 2013).

4.4. The RC-FIR relation

The FIR is known to be well correlated with RC (e.g., de Jong et al. 1985; Price & Duric 1992). Figure 10 shows the RC-FIR relation for our sample. We use *Spitzer* $70\mu\text{m}$ emission for our FIR values. The left panel shows the relation when we include the ‘ambiguous’ sources, whereas the right panel shows the relation with ‘ambiguous’ sources removed.

We compare our RC-FIR relation with that derived by (Yun et al. 2001, see their Equation 4). They relate the integrated total 1.4 GHz RC of an unresolved galaxy to the *IRAS* $60\mu\text{m}$ luminosity

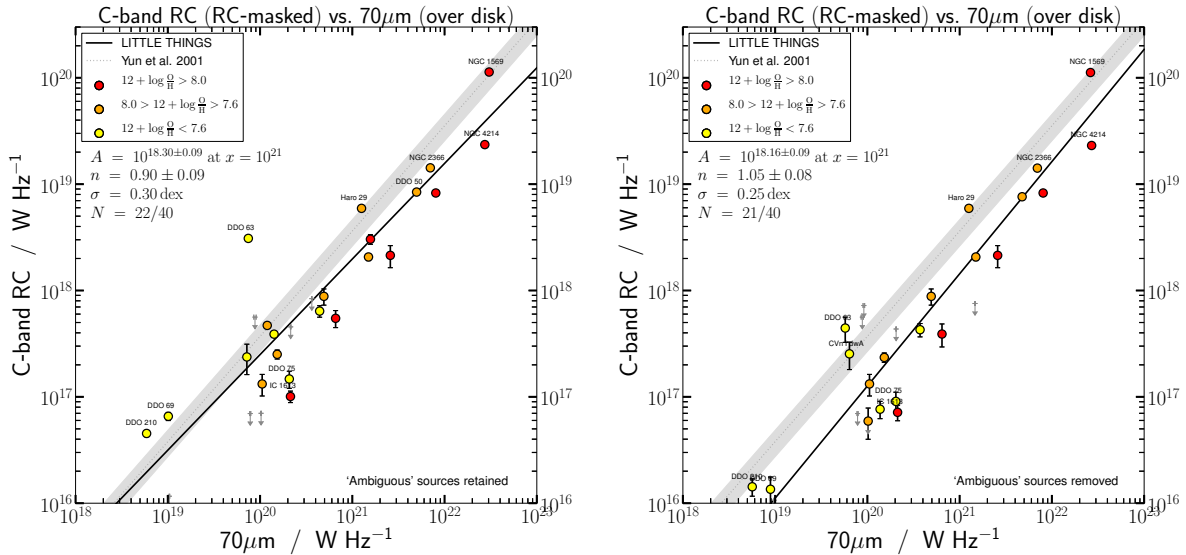


Fig. 10.— Galaxy-wide total C -band luminosity as a function of *Spitzer* $70\mu\text{m}$ FIR. Definite background sources have been removed, whilst the ‘ambiguous’ sources were retained in the left panel and removed in the right panels. The solid line is the best-fit power law to our sample. We show the Yun et al. (2001) RC–FIR relation as described in Equation 7 including the uncertainties introduced by our conversion (grey shaded band).

and find,

$$\frac{L_{6\text{GHz}}}{\text{W Hz}^{-1}} = (5.88 \pm 1.76) \times 10^{-3} \left(\frac{L_{70\mu\text{m}}}{\text{W Hz}^{-1}} \right)^{0.99}, \quad (7)$$

where we convert the *IRAS* $60\mu\text{m}$ luminosity to the equivalent *Spitzer* $70\mu\text{m}$ luminosity by scaling up by a factor of 1.27 (this assumes the Yun et al. 2001 galaxies are in a quiescent mode of SF, and that there is no significant emission from warm dust; $\beta = 1.82$ and $T_{\text{dust}} = 35\text{K}$). We also convert their VLA 1.4 GHz RC data by a factor of 2.83 to derive predicted equivalent JVLA 6 GHz flux densities assuming a constant spectral index of -0.7 between L - and C -band. The uncertainty given takes into account an uncertainty in the spectral index of 0.1 and a 15 K uncertainty in the dust temperature.

We find that the RC–FIR relation in Figure 10 (left panel) is slightly sub-linear—we find a power-law gradient of $\sim 0.9 \pm 0.1$ with a scatter of 0.3 dex.

A number of dwarfs in Figure 10 (left panel) are significantly radio ‘bright/loud’ even with respect to the Yun et al. (2001) sample. These data points (e.g., DDO 69, DDO 210, and Haro 29) har-

bour ‘ambiguous’ RC emission. Given that our dwarf galaxies may be affected by a RC excess introduced by including RC emission from unrelated background sources, we assume that the ‘ambiguous’ sources of RC emission are of background origin and remove them from our analysis. We present the RC–FIR relation (free from ‘ambiguous’ emission) in Figure 10 (right panel). This ensures that all of the isolated emission is from the dwarf itself, however, it is possible that we remove a fraction of dwarf emission (e.g., a SNR that we erroneously assume is a background galaxy).

We find that removing the ‘ambiguous’ sources does not significantly alter our results—our RC–FIR relation is characterised by a linear power-law index of 1.05 ± 0.08 with a scatter of 0.25 dex. Our RC–FIR relation shows a tentative divergence from the Yun et al. (2001) relation, although given the uncertainties in our power-law fit and the large scatter, we can not be conclusive on this. We do note that the dwarfs systematically fall under the Yun et al. (2001) relation—our dwarf galaxies are about a factor of 2 deficient in RC given what the FIR emission predicts. 

4.4.1. Thermal and non-thermal relations

We compare our RC_{Th} - and RC_{NTh} -FIR relations with those derived by Price & Duric (1992) in Figure 11. They found that, with the FIR luminosity, the RC_{Th} component has a linear nature whereas the RC_{NTh} component is related with a power-law index of 1.3.

4.5. The interplay between SF, RC and FIR

Current empirical relations derived from large populations of medium to large-sized galaxies (e.g., in this paper we concentrate particularly on the L -band RC: Yun et al. 2001; Condon et al. 2002) show that galaxy-wide RC emission is directly proportional to both the SFR and FIR emission of a galaxy. **In these types of galaxies, emission is bright meaning that contamination is a small issue.**

Since contamination is an issue in our dwarf galaxies (especially at the faint end), we decide to take the safe option by basing our results on the removal of all possible background sources sources (both obvious and ‘ambiguous’). **When doing this, we find that RC emission in dwarf galaxies is directly proportional to FIR, but not to SFR.**

The interplay between the SF, RC, and FIR can be summarised in three equations. First the RC-SFR relation we find to be:

$$\frac{\text{RC}}{\text{W Hz}^{-1}} = 10^{18.05 \pm 0.08} \left(\frac{\text{SFR}}{10^{-2} \text{M}_{\odot} \text{yr}^{-1}} \right)^{1.21 \pm 0.09}. \quad (8)$$

Then, there is the RC-FIR relation which we find to be:

$$\frac{\text{RC}}{\text{W Hz}^{-1}} = 10^{18.16 \pm 0.09} \left(\frac{70 \mu\text{m FIR}}{10^{21} \text{W Hz}^{-1}} \right)^{1.05 \pm 0.08}. \quad (9)$$

Equations 8 and 9 imply that the SFR and FIR are related by:

$$\frac{70 \mu\text{m FIR}}{\text{W Hz}^{-1}} = 10^{23.15} \left(\frac{\text{SFR}}{\text{M}_{\odot} \text{yr}^{-1}} \right)^{1.15}. \quad (10)$$

What do Equations 8, 9, and 10 mean in a physical sense?

There appears to be a change in the RC-SFR relation for systems forming stars at about 0.1–

1.0 $\text{M}_{\odot} \text{yr}^{-1}$. Above this star formation activity, galaxies follow a linear nature (e.g., Condon et al. 2002), whereas below this, the relation steepens to a power-law index of 1.2 ± 0.1 . Lee et al. (2009) found that, for SFRs $\lesssim 0.1 \text{M}_{\odot} \text{yr}^{-1}$, the $\text{H}\alpha$ emission in dwarfs is deficient for a given SFR when compared to larger galaxies. This can be explained by a truncated stellar IMF (see e.g., Weidner & Kroupa 2005; Plöckinger et al. in prep., for a chemo-dynamical model of truncated stellar IMFs in tidal dwarf galaxies), where a lack of ionising photons from fewer high mass ($\gtrsim 18 \text{M}_{\odot}$) stars results in less ionised H II for a given SFR. With a reduction in ionised regions, the free-free emission mechanism becomes less commonplace and accordingly the RC_{Th} too, underestimates the SFR.

4.5.1. Magnetic Fields

In spiral galaxies, the RC_{Th} fraction seldom exceeds 25% in C -band; however, the RC_{Th} fraction of our dwarf galaxies is about 40%. This is despite the fact that RC_{Th} emission, in an absolute sense, is reduced (Lee et al. 2009). For the dwarf galaxies to have a larger thermal fraction than larger galaxies (despite being deficient in RC_{Th}), there must be a [larger] reduction in their RC_{NTh} emission. To explain a reduction in the RC_{NTh} emission, we investigate the synchrotron emissivity in an optically thin region, ϵ_{NTh} :

$$\epsilon_{\text{NTh}} \propto n_{\text{CRe}} B_{\perp}^{\frac{\gamma+1}{2}} \quad (11)$$

where n_{CRe} is the number density of CRe present in the dwarf’s galactic magnetic field, B_{\perp} is the strength of the transverse magnetic field, and γ is the power-law slope of the CRe injection spectrum.

Usually, the assumption of equipartition is used in galaxies so that the energy densities of the magnetic field and the cosmic rays are in approximate equilibrium. It is, however, conceivable that dwarf galaxies in particular deviate from equipartition which would lead to a reduction in synchrotron emission (see Figure 8) in two different ways:

1) a low number density of CRe (n_{CRe}) present in the dwarf’s galactic magnetic field—galaxies are probably not electron calorimeters, with the possible exception of star burst galaxies (?). Dwarf galaxies in particular are prone to galac-

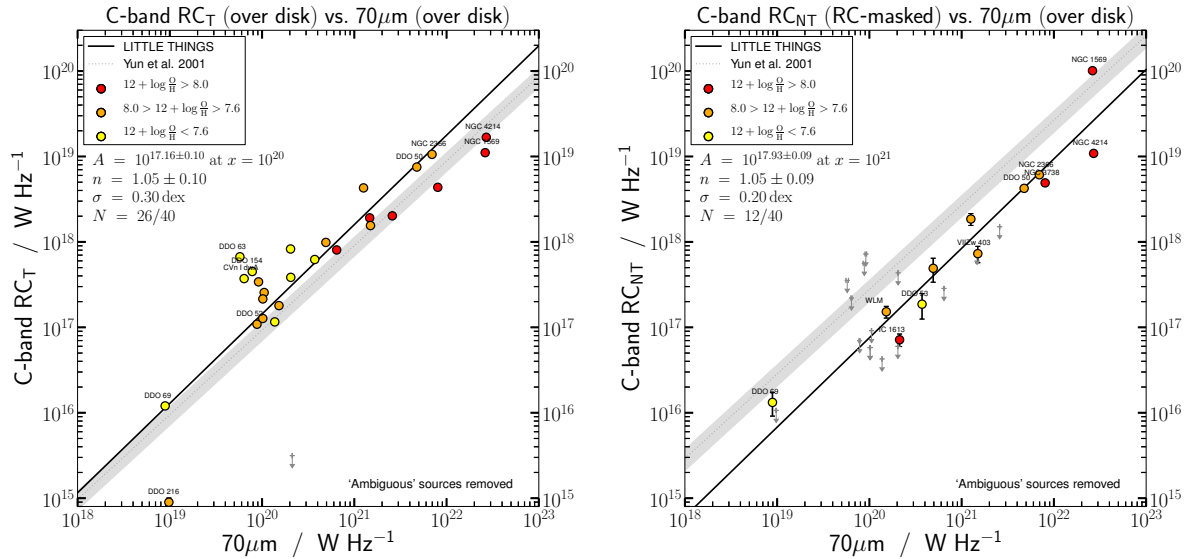


Fig. 11.— Galaxy-wide C -band RC_{Th} (left) and RC_{NTh} (right) luminosity as a function of *Spitzer* $70\mu m$ FIR. Both definite background and ‘ambiguous’ sources have been removed. The solid line is the best-fit power law to our sample. We show the Yun et al. (2001) RC–FIR relation as described in Equation 7 corrected by 0.25 for the RC_{Th} component (left) and by 0.75 for the RC_{NTh} component (right) including the errors introduced by our conversion (grey shaded band).

tic outflows and winds (since they have low mass and small disk scale heights), which can carry plasma and resident CRE advectively away from the galaxy.

2) the magnetic field strength (B) being lower than the equipartition value at which the energy density of the magnetic field is equal to that of the cosmic rays (electrons and protons combined). Dwarf galaxies may be sites of weak magnetic fields. In the standard paradigm of a mean field α - ω dynamo, the key ingredients are turbulence and shear; these are both weak in dwarfs, so magnetic field amplification may be less efficient.

In the following, the magnetic field strength in our sample of dwarf galaxies is estimated under the assumption of equipartition; this is the only practical way of estimating the field strengths. We used `bfield`⁷ which uses the equipartition formula for the total magnetic field (see Equation 3 from Beck & Krause 2005):

$$B_{eq} = \left[4\pi (1 - 2\alpha) (K_0 + 1) I_\nu E_p^{1+2\alpha} (\nu/2c_1)^{-\alpha} / (-2\alpha - 1) c_2(\alpha) l c_4(i) \right]^{1/(3-\alpha)}, \quad (12)$$

where α is the spectral index of the synchrotron

⁷<http://www3.mpifr-bonn.mpg.de/staff/mkrause/>

continuum⁸, I_ν is the synchrotron surface brightness at the frequency ν , K_0 is the proton-to-electron number density ratio (taken to be 100 for populations accelerated by the Fermi shock acceleration mechanism; Beck & Krause 2005), l is the line-of-sight distance through the emitting medium (assuming the disk of the dwarf galaxy has a scale height of 400 pc; Banerjee et al. 2011), E_p is the proton rest energy, $c_1 = 3e/(4\pi m_e^3 c^5)$, $c_2 = \frac{1}{4}c_3(\gamma + \frac{7}{3})/[(\gamma + 1)\Gamma(\frac{3\gamma-1}{12})\Gamma(\frac{3\gamma+7}{12})]$, $c_3 = \sqrt{3}e^3/(4\pi m_e c^2)$, and c_4 corrects for the inclination—for a regular field with constant inclination, this value is equal to $(\cos i)^{\gamma+1}/2$ where $\gamma = 1 - 2\alpha$ is the injection slope of the CRE.

The average B_{eq} inverse magnetic field strength of our sample is $(5.3 \pm 4.2)\mu G$ (see column 13 of Table 6) which is in excess of the $\sim 2\mu G$ found in ~ 50 faint dwarf galaxies from the NVSS catalogue (Roychowdhury & Chengalur 2012). Our high values come from the manner in which RC_{NTh} flux densities were extracted—we used the RC-based mask to isolate significant regions of RC_{NTh} emis-

⁸note that whilst the spectral index of *total* RC is about -0.5 in dwarfs, the spectral index of just the synchrotron component is expected to be -0.7 or steeper

sion which means we were generally looking at just regions of active SF.



The transverse field strength we measured is identical to that found in the WSRT SINGS sample ($9.7\mu\text{G}$; Heesen et al. 2014). This suggests that the magnetic field may not be too low in comparison with equipartition; rather, the cosmic rays are escaping leading to less synchrotron emission. This escape does not even need to be facilitated by winds or outflows; CRe may diffuse out of the dwarf easier than in spirals simply because the magnetic field scale height is probably lower.

5. Summary

We used the VLA in C-array to make C-band ($\nu = 6\text{ GHz}$ or $\lambda = 5\text{ cm}$) observations of 40 dwarf galaxies taken from LITTLE THINGS (Hunter et al. 2012). Our images have a resolution of $3''$ and an rms noise of $\sim 6\mu\text{Jy beam}^{-1}$ (in the centre of the map prior to correction for primary beam attenuation).

We summarise our findings as follows:

- Contamination from background sources was a prominent issue in earlier, low resolution studies. Linear relations (e.g. RC–SFR; the RC–FIR ‘conspiracy’) in dwarf galaxies could, in part, be attributed to contamination from background galaxies that themselves fall on such relations;
- Our resolution allowed us to single out background sources. A total of 26 out of the 40 LITTLE THINGS galaxies exhibit significant RC emission originating from the galaxy itself—17 are new RC detections. The flux densities of our brighter dwarfs agree with the literature, not differing by more than a factor of 2;
- We find that the average thermal fraction is $(42 \pm 24)\%$, whilst the non-thermal fraction is $(58 \pm 24)\%$. The RC_{NTh} fraction is lower than that found in larger spirals; this is despite the fact that the RC_{Th} emission is reduced, in an absolute sense (Lee et al. 2009), in dwarf galaxies;
- The LITTLE THINGS galaxies diverge from the Condon et al. (2002) RC–SFR relation at a SFR of $0.1\text{--}1.0M_{\odot}\text{ yr}^{-1}$. The sample

has a power-law slope of $\sim 1.2 \pm 0.1$ with a scatter of 0.2 dex. For SFRs of about $10^{-4}\text{--}10^{-3}M_{\odot}\text{ yr}^{-1}$, the observed RC is a factor of 10 deficient with that predicted from the Condon et al. (2002) relation—a similar factor to how H α -derived SFRs undercut FUV-inferred SFRs (Lee et al. 2009). We interpret this as an underproduction of both the RC_{Th} due to a truncated stellar IMF (see e.g., Lee et al. 2009) and the RC_{NTh} component due to CRe escape or low magnetic field strengths (typically $\lesssim 2.5\mu\text{G}$ over the entire disk);

- Within the uncertainties, we cannot conclusively say whether the dwarf galaxies continue the Yun et al. (2001) trend of deviating from $q_{70:6}$, or whether they are consistent with it. If there is a deviation, then this could be evidence that, while RC_{Th} emission is highly dependent on the truncated stellar IMF in dwarfs (Lee et al. 2009), FIR emission is not as affected since it is the ISRF that is the main contributor to dust-heating (Irwin et al. 2013).
- The LITTLE THINGS galaxies also fall below the Yun et al. (2001) RC–FIR relation. The observed RC is a factor of 2 deficient with the extrapolated Yun et al. (2001) relation; this deficiency is constant across our range of dwarf galaxies. We observe a power-law slope of $\sim 1.05 \pm 0.08$ with a scatter of 0.25 dex—within the uncertainties, our data are consistent with a linear trend suggesting that the ‘conspiracy’ of the RC–FIR relation continues to hold even for dwarf galaxies.
- The typical strength of the transverse magnetic field is $\sim 9.3\mu\text{G}$ (from only the regions that exhibited significant RC emission). This value is similar to larger galaxies (e.g., $9.7\mu\text{G}$ in WSRT SINGS; Heesen et al. 2014), which suggests that it is the escape of CRe that is responsible for the deficient RC_{NTh} emission. The escape of CRe is probably facilitated by a small magnetic field scale height.

6. Acknowledgements

We thank Dan Smith for some insight on the RC–FIR relation, and his help with FIR–related work. We also appreciate Min Yun for his willingness to provide us with his *IRAS* and VLA data from the Yun et al. (2001) study.

REFERENCES

- Altschuler, D. R., Giovanardi, C., Giovanelli, R. & Haynes, M. P., 1984, *AJ*, 89, 224
- Appleton, P. N., Fadda, D. T., Marleau, F. R., Frayer, D. T., Helou, G., Condon, J. J., Choi, P. I., Yan, L., Lacy, M., Wilson, G., Armus, L., Chapman, S. C., Fang, F., Heinrichson, I., Im, M., Jannuzi, B. T., Storrie-Lombardi, L. J., Shupe, D., Soifer, B. T., Squires, G. & Teplitz, H. I., 2004, *ApJS*, 154, 147
- Baars, J. W. M., Genzel, R., Pauliny-Toth, I. I. K. & Witzel, A., 1977, *A&A*, 61, 99
- Banerjee, A., Jog, C. J., Brinks, E. & Bagetakos, I., 2011, *MNRAS*, 415, 687
- Beck, R. & Krause, M., 2005, *Astronomisch*, 326, 414
- Beck, R., 2009, *Astrophysic*, 5, 43
- Bell, E. F., 2003, *ApJ*, 586, 794
- Bigiel, F., Leroy, A., Walter, F., Brinks, E., de Blok, W. J. G., Madore, B. & Thornley, M. D., 2008, *AJ*, 136, 2846
- Burstein, D. & Heiles, C., 1982, *AJ*, 87, 1165
- Calzetti, D., Kennicutt, R. C., Engelbracht, C. W., Leitherer, C., Draine, B. T., Kewley, L., Moustakas, J., Sosey, M., Dale, D. A., Gordon, K. D., Helou, G. X., Hollenbach, D. J., Armus, L., Bendo, G., Bot, C., Buckalew, B., Jarrett, T., Li, A., Meyer, M., Murphy, E. J., Prescott, M., Regan, M. W., Rieke, G. H., Roussel, H., Sheth, K., Smith, J. D. T., Thornley, M. D. & Walter, F., 2007, *ApJ*, 666, 870
- Calzetti, D., Wu, S.-Y., Hong, S., Kennicutt, R. C., Lee, J. C., Dale, D. A., Engelbracht, C. W., van Zee, L., Draine, B. T., Hao, C.-N., Gordon, K. D., Moustakas, J., Murphy, E. J., Regan, M., Begum, A., Block, M., Dalcanton, J., Funes, J., Gil de Paz, A. and Johnson, B., Sakai, S., Skillman, E., Walter, F., Weisz, D., Williams, B., Wu, Y., 2010, *ApJ*, 714, 1256
- Cardelli, J. A., Clayton, G. C. & Mathis, J. S., 1989, *ApJ*, 345, 245
- Chomiuk, L. & Wilcots, E. M., 2009, *AJ*, 137, 3869
- Chyży, K. T., Wezgowiec, M., Beck, R. & Bomans, D. J., 2011, *A&A*, 529, A94
- Condon, J. J., Cotton, W. D., Greisen, E. W., Yin, Q. F., Perley, R. A., Taylor, G. B. & Broderick, J. J., 1998, *AJ*, 115, 1693
- Condon, J. J., Cotton, W. D. & Broderick, J. J., 2002, *AJ*, 124, 675
- Condon, J. J., Cotton, W. D., Fomalont, E. B., Kellermann, K. I., Miller, N., Perley, R. A., Scott, D., Vernstrom, T. & Wall, J. V., 2012, *ApJ*, 758, 23
- Condon, J. J., 1992, *ARA&A*, 30, 575
- Dale, D. A., Cohen, S. A., Johnson, L. C., Schuster, M. D., Calzetti, D., Engelbracht, C. W., Gil de Paz, A., Kennicutt, R. C., Lee, J. C., Begum, A., Block, M., Dalcanton, J. J., Funes, J. G., Gordon, K. D., Johnson, B. D., Marble, A. R., Sakai, S., Skillman, E. D., van Zee, L., Walter, F., Weisz, D. R., Williams, B., Wu, S.-Y. & Wu, Y., 2009, *ApJ*, 703, 517
- Deeg, H.-J., Duric, N. & Brinks, E., 1997, *A&A*, 323, 323
- Draine, B. T. & Hensley, B., 2012, *ApJ*, 757, 103
- Dubois, Y. & Teyssier, R., 2010, *A&A*, 523, A72
- Duric, N., 1991, *Internationa*, 2, 392
- Engelbracht, C. W., Blaylock, M., Su, K. Y. L., Rho, J., Rieke, G. H., Muzerolle, J., Padgett, D. L., Hines, D. C., Gordon, K. D., Fadda, D., Noriega-Crespo, A., Kelly, D. M., Latter, W. B., Hinz, J. L., Misselt, K. A., Morrison, J. E., Stansberry, J. A., Shupe, D. L., Stolovy, S., Wheaton, W. A., Young, E. T., Neugebauer, G., Wachter, S., Pérez-González, P. G., Frayer, D. T., Marleau, F. R., 2007, *PASP*, 119, 994
- Fenech, D. M., Muxlow, T. W. B., Beswick, R. J., Pedlar, A. & Argo, M. K., 2008, *MNRAS*, 391, 1384
- Ferguson, A. M. N., Wyse, R. F. G., Gallagher, III, J. S. & Hunter, D. A., 1996, *AJ*, 111, 2265
- Filipovic, M. D., Haynes, R. F., White, G. L., Jones, P. A., Klein, U. & Wielebinski, R., 1995, *A&AS*, 111, 311

- Filipovic, M. D., Haynes, R. F., White, G. L. & Jones, P. A., 1998, *A&AS*, 130, 421
- Gallagher, III, J. S. & Hunter, D. A., 1984, *ARA&A*, 22, 37
- Gehrels, N., 1986, *ApJ*, 303, 336
- Gil de Paz, A., Boissier, S., Madore, B. F., Seibert, M., Joe, Y. H., Boselli, A., Wyder, T. K., Thilker, D., Bianchi, L., Rey, S.-C., Rich, R. M., Barlow, T. A., Conrow, T., Forster, K., Friedman, P. G., Martin, D. C., Morrissey, P., Neff, S. G., Schiminovich, D., Small, T., Donas, J., Heckman, T. M., Lee, Y.-W., Milliard, B., Szalay, A. S. & Yi, S., 2007, *ApJS*, 173, 185
- Heesen, V., Beck, R., Krause, M. & Dettmar, R.-J., 2009, *A&A*, 494, 563
- Heesen, V., Rau, U., Rupen, M. P., Brinks, E. & Hunter, D. A., 2011, *ApJ*, 739, L23
- Helmboldt, J. F., Walterbos, R. A. M., Bothun, G. D. & O'Neil, K., 2005, *ApJ*, 630, 824
- Helou, G., Soifer, B. T. & Rowan-Robinson, M., 1985, *ApJ*, 298, L7
- Höppe, G., Brinks, E., Klein, U., Giovanardi, C., Altschuler, D. R., Price, R. M. & Deeg, H.-J., 1994, *AJ*, 108, 446
- Hunter, D. A. & Elmegreen, B. G., 2004, *AJ*, 128, 2170
- Hunter, D. A. & Elmegreen, B. G., 2006, *ApJS*, 162, 49
- Hunter, D. A. & Gallagher, III, J. S., 1992, *ApJ*, 391, L9
- Hunter, D. A., Ficut-Vicas, D., Ashley, T., Brinks, E., Cigan, P., Elmegreen, B. G., Heesen, V., Herrmann, K. A., Johnson, M., Oh, S.-H., Rupen, M. P., Schrubba, A., Simpson, C. E., Walter, F., Westpfahl, D. J., Young, L. M. & Zhang, H.-X., 2012, *AJ*, 144, 134
- Huynh, M. T., Hopkins, A. M., Lenc, E., Mao, M. Y., Middelberg, E., Norris, R. P. & Randall, K. E., 2012, *MNRAS*, 426, 2342
- Ilovaisky, S. A. & Lequeux, J., 1972, *A&A*, 20, 347
- Irwin, J. A., Brar, R. S., Saikia, D. J. & Henriksen, R. N., 2013, *MNRAS*, 433, 2958
- Kennicutt, Jr., R. C., 1998, *ARA&A*, 36, 189
- Kepley, A. A., Mühle, S., Everett, J., Zweibel, E. G., Wilcots, E. M., Klein, U., 2010, *ApJ*, 712, 536
- Kepley, A. A., Zweibel, E. G., Wilcots, E. M., Johnson, K. E. & Robishaw, T., 2011, *ApJ*, 736, 139
- Klein, U., Graeve, R. & Wielebinski, R., 1983, *A&A*, 117, 332
- Klein, U., Weiland, H. & Brinks, E., 1991, *A&A*, 246, 323
- Klein, U., Giovanardi, C., Altschuler, D. R. & Wunderlich, E., 1992, *A&A*, 255, 49
- Klein, U., 1986, *A&A*, 168, 65
- Kroupa, P., 2001, *MNRAS*, 322, 231
- Lacki, B. C., Thompson, T. A. & Quataert, E., 2010, *ApJ*, 717, 1
- Lagos, C. D. P., Lacey, C. G., Baugh, C. M., Bower, R. G. & Benson, A. J., 2011, *MNRAS*, 416, 1566
- Lee, J. C., Gil de Paz, A., Tremonti, C., Kennicutt, Jr., R. C., Salim, S., Bothwell, M., Calzetti, D., Dalcanton, J., Dale, D., Engelbracht, C., Funes, S. J. J. G., Johnson, B., Sakai, S., Skillman, E., van Zee, L., Walter, F. & Weisz, D., 2009, *ApJ*, 706, 599
- Leroy, A. K., Bigiel, F., de Blok, W. J. G., Boissier, S., Bolatto, A., Brinks, E., Madore, B., Muñoz-Mateos, J.-C., Murphy, E., Sandstrom, K., Schrubba, A. & Walter, F., 2012, *AJ*, 144, 3
- Lisenfeld, U. & Ferrara, A., 1998, *ApJ*, 496, 145
- Lisenfeld, U., Wilding, T. W. & Pooley, G. G. and 2004, *MNRAS*, 349, 1335
- Lozinskaya, T. A., Silchenko, O. K., Helfand, D. J. & Goss, W. M., 1998, *AJ*, 116, 2328
- Maeder, A. & Meynet, G., 1989, *A&A*, 210, 155

- Martin, N. F., Ibata, R. A., Chapman, S. C., Irwin, M. & Lewis, G. F., 2007, *MNRAS*, 380, 281
- Mateo, M. L., 1998, *ARA&A*, 36, 435
- Murphy, E. J., Helou, G., Braun, R., Kenney, J. D. P., Armus, L., Calzetti, D., Draine, B. T., Kennicutt, Jr., R. C., Roussel, H., Walter, F., Bendo, G. J., Buckalew, B., Dale, D. A., Engelbracht, C. W., Smith, J. D. T. & Thornley, M. D., 2006, *ApJ*, 651, L111
- Murphy, E. J., Helou, G., Kenney, J. D. P., Armus, L. & Braun, R., 2008, *ApJ*, 678, 828
- Murphy, E. J., Condon, J. J., Schinnerer, E., Kennicutt, R. C., Calzetti, D., Armus, L., Helou, G., Turner, J. L., Aniano, G., Beirão, P., Bolatto, A. D., Brandl, B. R., Croxall, K. V., Dale, D. A., Donovan Meyer, J. L., Draine, B. T., Engelbracht, C., Hunt, L. K., Hao, C.-N., Koda, J., Roussel, H., Skibba, R., Smith, J.-D. T., 2011, *ApJ*, 737, 67
- Niklas, S., Klein, U. & Wielebinski, R., 1997, *A&A*, 322, 19
- Oey, M. S., Meurer, G. R., Yelda, S., Furst, E. J., Caballero-Nieves, S. M., Hanish, D. J., Levesque, E. M., Thilker, D. A., Walth, G. L., Bland-Hawthorn, J., Dopita, M. A., Ferguson, H. C., Heckman, T. M., Doyle, M. T., Drinkwater, M. J., Freeman, K. C., Kennicutt, Jr., R. C., Kilborn, V. A., Knezek, P. M., Koribalski, B., Meyer, M., Putman, M. E., Ryan-Weber, E. V., Smith, R. C., Staveley-Smith, L., Webster, R. L., Werk, J. & Zwaan, M. A., 2007, *ApJ*, 661, 801
- Offringa, A. R., de Bruyn, A. G., Biehl, M., Zaroubi, S., Bernardi, G. & Pandey, V. N., 2010, *MNRAS*, 405, 155
- Offringa, A. R., de Bruyn, A. G. & Zaroubi, S., 2012, *MNRAS*, 422, 563
- Oskinova, L. M., Steinke, M., Hamann, W.-R., Sander, A., Todt, H. & Liermann, A., 2013, *MNRAS*, ,
- Owen, F. N. & Morrison, G. E., 2008, *AJ*, 136, 1889
- Padovani, P., 2011, *MNRAS*, 411, 1547
- Papadopoulos, P. P., 2010, *ApJ*, 720, 226
- Planck Collaboration, Ade, P. A. R., Aghanim, N., Arnaud, M., Ashdown, M., Aumont, J., Baccigalupi, C., Balbi, A., Banday, A. J. & Barreiro, R. B. and et al., 2011, *A&A*, 536, A20
- Price, R. & Duric, N., 1992, *ApJ*, 401, 81
- Rau, U. & Cornwell, T. J., 2011, *A&A*, 532, A71
- Rau, U., Bhatnagar, S., Voronkov, M. A. & Cornwell, T. J., 2009, *IEE*, 97, 1472
- Roychowdhury, S. & Chengalur, J. N., 2012, *MNRAS*, 423, L127
- Sanchez-Janssen, R. & Sanchez-Janssen, 2011, *non*, 277, 230
- Schlegel, D. J., Finkbeiner, D. P. & Davis, M., 1998, *ApJ*, 500, 525
- Stil, J. M. & Israel, F. P., 2002, *A&A*, 389, 29
- Stinson, G. S., Dalcanton, J. J., Quinn, T., Kaufmann, T. & Wadsley, J., 2007, *ApJ*, 667, 170
- Ulvestad, J. S., 2009, *AJ*, 138, 1529
- Völk, H. J., 1989, *A&A*, 218, 67
- Verdes-Montenegro, L., Sulentic, J., Lisenfeld, U. and Leon, S., Espada, D., Garcia, E., Sabater, J., Verley, S., 2005, *A&A*, 436, 443
- Verkhodanov, O. V. & Khabibullina, M. L., 2010, *Astronom*, 36, 7
- Walter, F., Cannon, J. M., Roussel, H., Bendo, G. J., Calzetti, D., Dale, D. A., Draine, B. T., Helou, G., Kennicutt, Jr., R. C., Moustakas, J., Rieke, G. H., Armus, L., Engelbracht, C. W., Gordon, K., Hollenbach, D. J., Lee, J., Li, A., Meyer, M. J., Murphy, E. J., Regan, M. W., Smith, J.-D. T., Brinks, E., de Blok, W. J. G., Bigiel, F. & Thornley, M. D., 2007, *ApJ*, 661, 102
- Weidner, C. & Kroupa, P., 2005, *ApJ*, 625, 754
- White, R. L., Becker, R. H., Helfand, D. J. & Gregg, M. D., 1997, *ApJ*, 475, 479

- Wyder, T. K., Martin, D. C., Schiminovich, D., Seibert, M., Budavári, T., Treyer, M. A., Barlow, T. A., Forster, K., Friedman, P. G., Morrissey, P., Neff, S. G., Small, T., Bianchi, L., Donas, J., Heckman, T. M., Lee, Y.-W., Madore, B. F., Milliard, B., Rich, R. M., Szalay, A. S., Welsh, B. Y., Yi, S. K., 2007, ApJS, 173, 293
- Wyder, T. K., Jackson, D. C., Skillman, E. D., Cannon, J. M. & Gehrz, R. D., 2009, , ,
- Wynn-Williams, C. G. & Becklin, E. E., 1986, ApJ, 308, 620
- Xu, C., Lisenfeld, U. & Völk, H. J., 1994, A&A, 285, 19
- Xu, C., 1990, ApJ, 365, L47
- Yun, M. S., Reddy, N. A. & Condon, J. J., 2001, ApJ, 554, 803
- Zhang, H.-X., Hunter, D. A., Elmegreen, B. G., Gao, Y. & Schrubba, A., 2012, AJ, 143, 47
- de Jong, T., Klein, U., Wielebinski, R. & Wunderlich, E., 1985, A&A, 147, L6
- Ficut-Vicas, D., 2013, ApJ, unknown, unknown

A. Individual Notes

In this section, we provide individual notes on our RC observations. We focus on prominent features, and also on notable diversions from our normal line of calibration and image generation.

CVnI dwA: There were not any notable deviations from our calibration/imaging pipeline.

DDO 43: A bright source (87GB[BWE91] 0724+4053; flux density of 37mJy located 2.5' from the image phase centre) exhibited prominent sidelobes which filled the FOV. DDO 43 was directly affected by, in particular, an E–W artefact.

DDO 46: Due to the uniform weighting method (`robust=0.0`) not yielding significant regions of galactic emission, another `clean` was performed using an approach closer to natural weighting (`robust=0.5`).

DDO 47: Due to the uniform weighting method (`robust=0.0`) not yielding significant regions of galactic emission, another `clean` was performed using an approach closer to natural weighting (`robust=0.5`).

DDO 50: A bright source (NVSS J081920 +704907; flux density of 18mJy located 5.5' from the image phase centre) exhibited weak sidelobes which filled the FOV. Selected parts of DDO 50 were directly affected by low–level artefacts. A single round of self–calibration was performed which was successful in minimising the prominent sidelobes originating from NVSS J081920+704907.

DDO 52: Two bright sources (NVSS J082842 +415056; flux density of 19mJy located 2.5' from the image phase centre and NVSS J082814+415353; flux density of 39mJy located 4' from the image phase centre) exhibited weak sidelobes which filled the FOV. DDO 52 was directly affected by the artefacts. Self–calibration was not performed as it was not deemed necessary.

DDO 63: Due to the uniform weighting method (`robust=0.0`) not yielding significant regions of galactic emission, another `clean` was performed using an approach closer to natural weighting (`robust=0.5`).

DDO 69: There were not any notable deviations from our calibration/imaging pipeline.

DDO 70: There were not any notable deviations from our calibration/imaging pipeline.

DDO 75: A bright source (NVSS J101030 -044006; flux density of unknown flux density located 7' from the image phase centre) exhibited weak sidelobes which filled the FOV. Parts of DDO 75 were directly affected by low–level artefacts. A single round of self–calibration was performed which was successful in minimising the prominent sidelobes originating from NVSS J101030-044006

DDO 101: A bright source (NVSS J115618 +312805; unknown flux density located 9' from the image phase centre) exhibited prominent sidelobes which filled the FOV. DDO 101 was directly affected by the artefacts. Self–calibration was not successful in minimising the effects of the sidelobes, which was attributed to the fact that the complex gain calibration of NVSS J115618+312805 became troublesome since it suffered from a time–varying effect whereby the interferometer picks up a strongly varying signal due to the source passing through sidelobe peaks, and then nulls. We decided to use just 3 spectral windows for which NVSS J115618+312805 fell near the primary beam null. This was successful in minimising the prominent sidelobes originating from NVSS J115618+312805.

DDO 126: A bright double–source (NVSS J122658 +370719; flux density of 4.6mJy located 1.5' from the image phase centre) exhibited prominent sidelobes which filled the FOV. DDO 126 was directly affected by the artefacts. A single round of self–calibration was performed which was successful in minimising the prominent sidelobes originating from NVSS J122658+370719.

DDO 133: Due to the uniform weighting method (`robust=0.0`) not yielding significant regions of galactic emission, another `clean` was performed using an approach closer to natural weighting (`robust=0.5`).

DDO 154: Two bright sources (NVSS J125401 +270357; flux density of 18mJy located 5.5' from the image phase centre and unknown; unknown flux density located 5.5' from the image phase centre) exhibited weak sidelobes which filled the FOV. DDO 154 was not affected by low–level artefacts. A single round of self–calibration was performed which was successful in minimising the prominent sidelobes originating from NVSS J125401+270357 and the other unknown source. Due to the uniform weighting method (`robust=0.0`) not yielding significant regions of galactic emission, another `clean` was performed using an approach closer

to natural weighting (`robust=0.5`).

DDO 165: Due to the uniform weighting method (`robust=0.0`) not yielding significant regions of galactic emission, another `clean` was performed using an approach closer to natural weighting (`robust=0.5`).

DDO 167: There were not any notable deviations from our calibration/imaging pipeline.

DDO 168: There were not any notable deviations from our calibration/imaging pipeline.

DDO 187: A bright double-source (NVSS J141556 +230730; flux density of 55mJy located 4.5' from the image phase centre) exhibited prominent sidelobes which filled the FOV. DDO 187 was directly affected by the artefacts. A single round of self-calibration was performed which was successful in minimising the prominent sidelobes originating from NVSS J141556+230730.

DDO 210: Due to the uniform weighting method (`robust=0.0`) not yielding significant regions of galactic emission, another `clean` was performed using an approach closer to natural weighting (`robust=0.5`).

DDO 216: Due to the uniform weighting method (`robust=0.0`) not yielding significant regions of galactic emission, another `clean` was performed using an approach closer to natural weighting (`robust=0.5`).

F564 V3: There were not any notable deviations from our calibration/imaging pipeline.

Haro 29: There were not any notable deviations from our calibration/imaging pipeline.

Haro 36: There were not any notable deviations from our calibration/imaging pipeline.

LGS 3: Due to the uniform weighting method (`robust=0.0`) not yielding significant regions of galactic emission, another `clean` was performed using an approach closer to natural weighting (`robust=0.5`).

M81 dwA: A bright source (NVSS J082451 +705808; unknown flux density located 5.5' from the image phase centre) exhibited prominent sidelobes which filled the FOV. M81 dwA was directly affected by the artefacts. Self-calibration was not successful in minimising the effects of the sidelobes, which was attributed to the fact that the complex gain calibration of NVSS J082451+705808 became troublesome since it suffered from a time-varying effect whereby the interferometer picks up a strongly varying signal due to the source passing through sidelobe peaks, and then nulls. We decided to use just 3 spectral windows for which NVSS J082451+705808 fell near the primary beam null. This was successful in minimising the prominent sidelobes originating from NVSS J082451+705808.

Mrk 178: There were not any notable deviations from our calibration/imaging pipeline. The *GALEX* FUV image was dropped from the analysis due to being of poor quality.

NGC 1569: There were not any notable deviations from our calibration/imaging pipeline. The *Spitzer* 24 μ m and 70 μ m images were dropped from the analysis due to being of poor quality.

NGC 2366: There were not any notable deviations from our calibration/imaging pipeline.

NGC 3738: A bright triple-source (NVSS J113545 +543319; combined flux density of 63mJy located 2' from the image phase centre) exhibited prominent sidelobes which filled the FOV. NGC 3738 was directly affected by the artefacts. A single round of self-calibration was performed which was successful in minimising the prominent sidelobes originating from NVSS J113545+543319.

NGC 4163: Due to the uniform weighting method (`robust=0.0`) not yielding significant regions of galactic emission, another `clean` was performed using an approach closer to natural weighting (`robust=0.5`).

NGC 4214: NGC 4214 itself (especially the H II region centred on 12^h15^m41^s.2 +36°19'04".6) was bright enough that prominent sidelobes were produced which filled the FOV. A single round of self-calibration was performed which was successful in minimising the prominent sidelobes originating from NGC 4214.

UGC 8508: Two sources (not coincident with H α emission) from the 4' square aperture were judged as *not* originating from UGC 8508 and were accordingly masked out.

VII Zw 403: There were not any notable deviations from our calibration/imaging pipeline. The *Spitzer* 24 μ m and 70 μ m images were dropped from the analysis due to being of poor quality.

WLM: A bright source (NVSS J000141-154040; unknown flux density located 13' from the image phase centre) exhibited prominent sidelobes which filled the FOV. WLM was directly affected by the artefacts. A single round of self-calibration was performed which was successful in minimising the prominent sidelobes

originating from NVSS J000141-154040.

B. Images

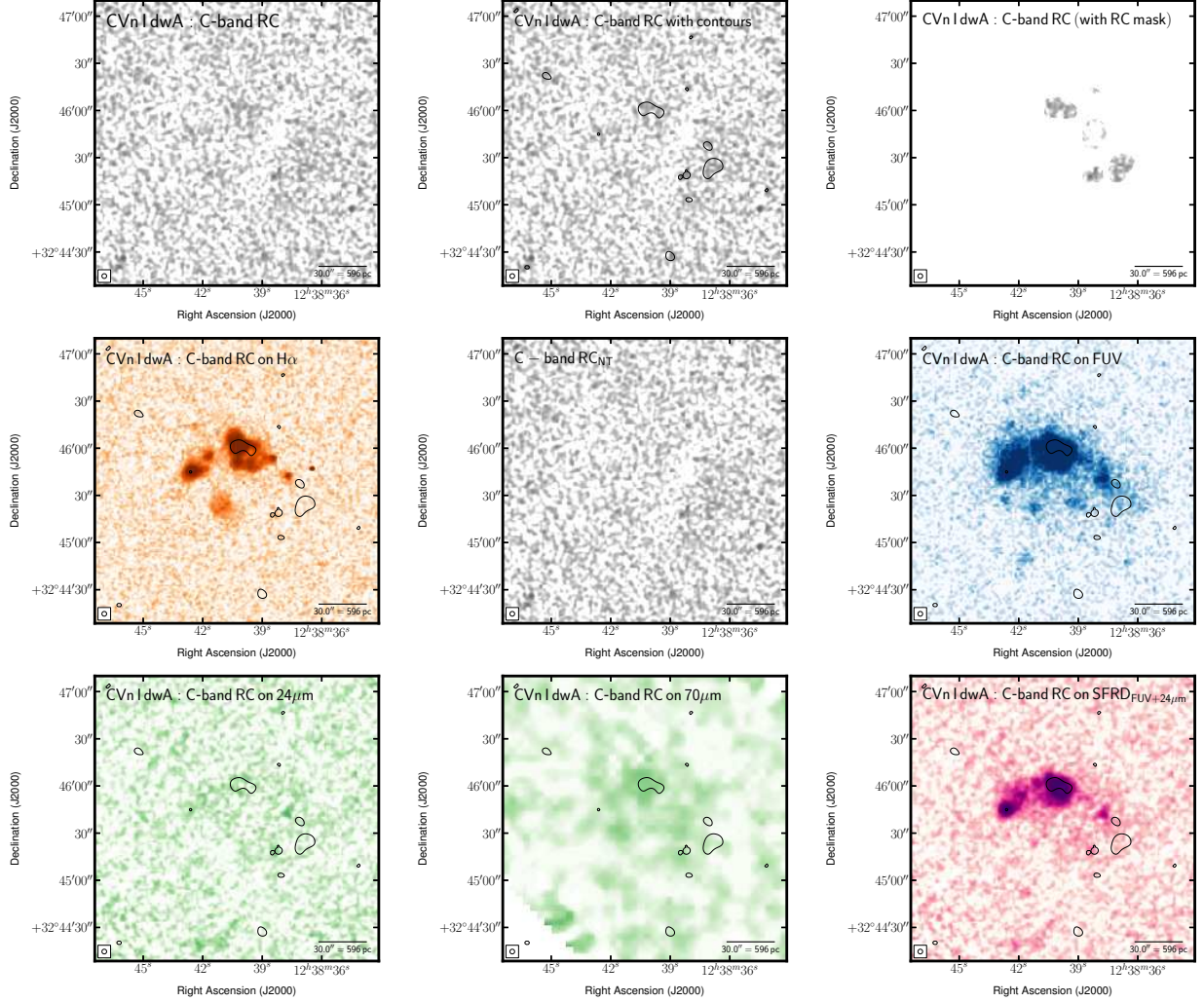


Fig. 12.— Multi-wavelength coverage of CVn I dwA displaying a $3' \times 3'$ area. We show total RC flux density at the native resolution (top left) and again with contours (top centre). The lowest contour highlights low-surface brightness emission at a level of $22.5 \mu\text{Jy beam}^{-1}$ —this is 2.5 times the rms after smoothing the native image by a factor of 2.5. The other contours are placed following $(2 + 2^n)\sigma_{\text{native}}$, where $n \geq 0$ and both the rms ($\sigma_{\text{native}} = 4.27 \mu\text{Jy beam}^{-1}$) and the resolution ($\text{FWHM}_{\text{native}} = 3.0 \times 3.0$ arcsec) are taken from the native resolution image. These same contours are also superposed on ancillary LITTLE THINGS images where possible: $\text{H}\alpha$ (middle left); RC_{NT} inferred from Deeg et al. 1997 (middle centre); *GALEX* FUV (middle right); *Spitzer* $24 \mu\text{m}$ (bottom left); *Spitzer* $70 \mu\text{m}$ (bottom centre); FUV+ $24 \mu\text{m}$ -inferred SFRD from Leroy et al. 2012 (bottom right). We also show the RC that was isolated by the RC-based masking technique (top right). The greyscale intensity scales used are arbitrary to best highlight structure.

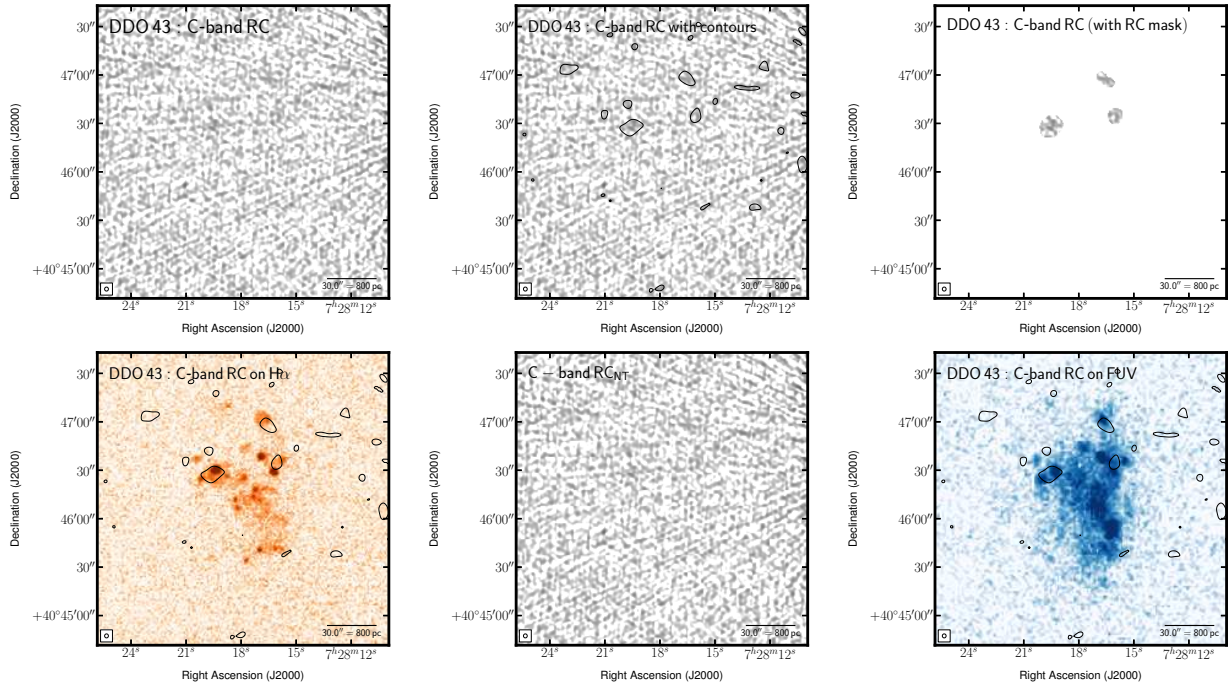


Fig. 13.— Multi-wavelength coverage of DDO 43 displaying a $3' \times 3'$ area. We show total RC flux density at the native resolution (top left) and again with contours (top centre). The lowest contour highlights low-surface brightness emission at a level of $27.6 \mu\text{Jy beam}^{-1}$ —this is 2.5 times the rms after smoothing the native image by a factor of 2.5. The other contours are placed following $(2 + 2^n)\sigma_{\text{native}}$, where $n \geq 0$ and both the rms ($\sigma_{\text{native}} = 6.89 \mu\text{Jy beam}^{-1}$) and the resolution ($\text{FWHM}_{\text{native}} = 2.5 \times 2.3 \text{ arcsec}$) are taken from the native resolution image. These same contours are also superposed on ancillary LITTLE THINGS images where possible: $\text{H}\alpha$ (middle left); RC_{NTh} inferred from Deeg et al. 1997 (middle centre); *GALEX* FUV (middle right). We also show the RC that was isolated by the RC-based masking technique (top right). The greyscale intensity scales used are arbitrary to best highlight structure.

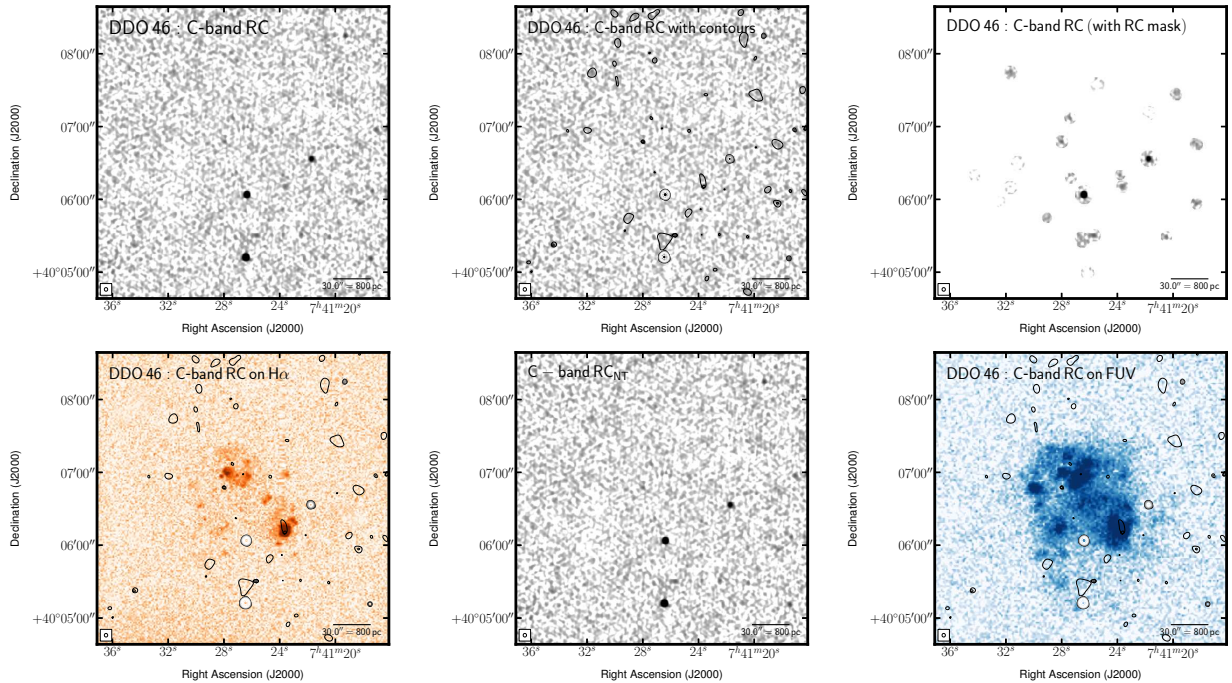


Fig. 14.— Multi-wavelength coverage of DDO 46 displaying a $4' \times 4'$ area. We show total RC flux density at the native resolution (top left) and again with contours (top centre). The lowest contour highlights low-surface brightness emission at a level of $22.0 \mu\text{Jy beam}^{-1}$ —this is 2.5 times the rms after smoothing the native image by a factor of 2.5. The other contours are placed following $(2 + 2^n)\sigma_{\text{native}}$, where $n \geq 0$ and both the rms ($\sigma_{\text{native}} = 5.06 \mu\text{Jy beam}^{-1}$) and the resolution ($\text{FWHM}_{\text{native}} = 3.0 \times 2.8$ arcsec) are taken from the native resolution image. These same contours are also superposed on ancillary LITTLE THINGS images where possible: $\text{H}\alpha$ (middle left); RC_{NTh} inferred from Deeg et al. 1997 (middle centre); *GALEX* FUV (middle right). We also show the RC that was isolated by the RC-based masking technique (top right). The greyscale intensity scales used are arbitrary to best highlight structure.

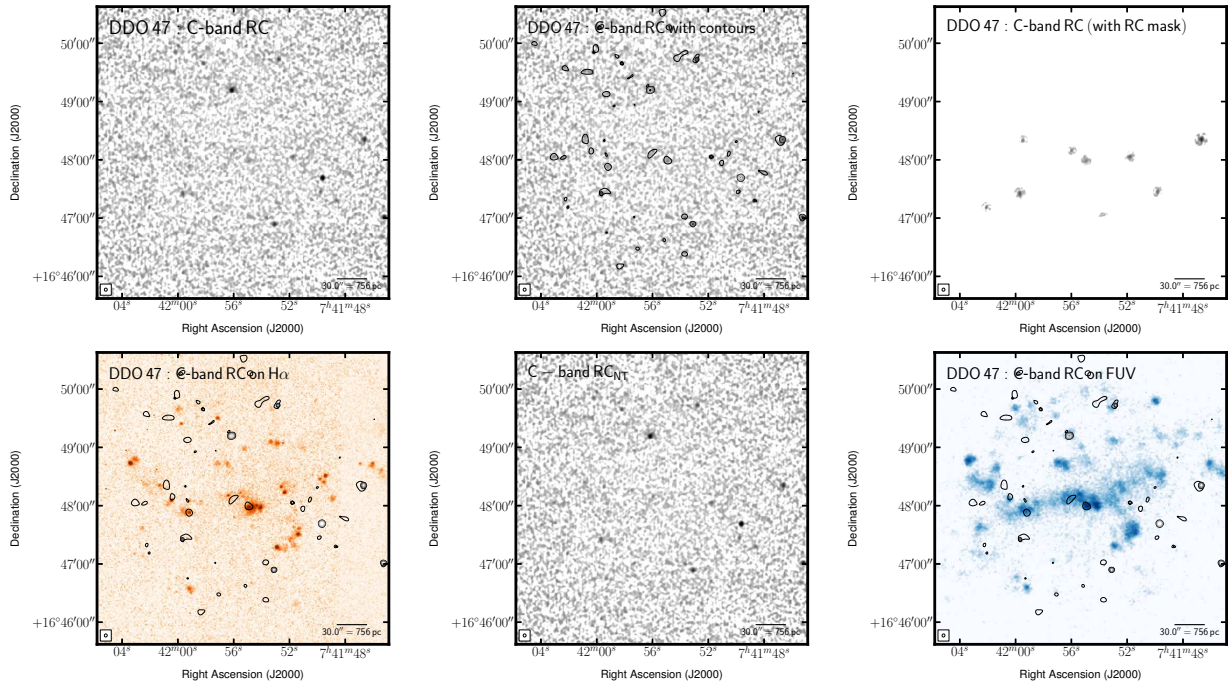


Fig. 15.— Multi-wavelength coverage of DDO 47 displaying a $5' \times 5'$ area. We show total RC flux density at the native resolution (top left) and again with contours (top centre). The lowest contour highlights low-surface brightness emission at a level of $19.5 \mu\text{Jy beam}^{-1}$ —this is 2.5 times the rms after smoothing the native image by a factor of 2.5. The other contours are placed following $(2 + 2^n)\sigma_{\text{native}}$, where $n \geq 0$ and both the rms ($\sigma_{\text{native}} = 4.98 \mu\text{Jy beam}^{-1}$) and the resolution ($\text{FWHM}_{\text{native}} = 3.2 \times 3.0 \text{ arcsec}$) are taken from the native resolution image. These same contours are also superposed on ancillary LITTLE THINGS images where possible: $\text{H}\alpha$ (middle left); RC_{NTh} inferred from Deeg et al. 1997 (middle centre); *GALEX* FUV (middle right). We also show the RC that was isolated by the RC-based masking technique (top right). The greyscale intensity scales used are arbitrary to best highlight structure.

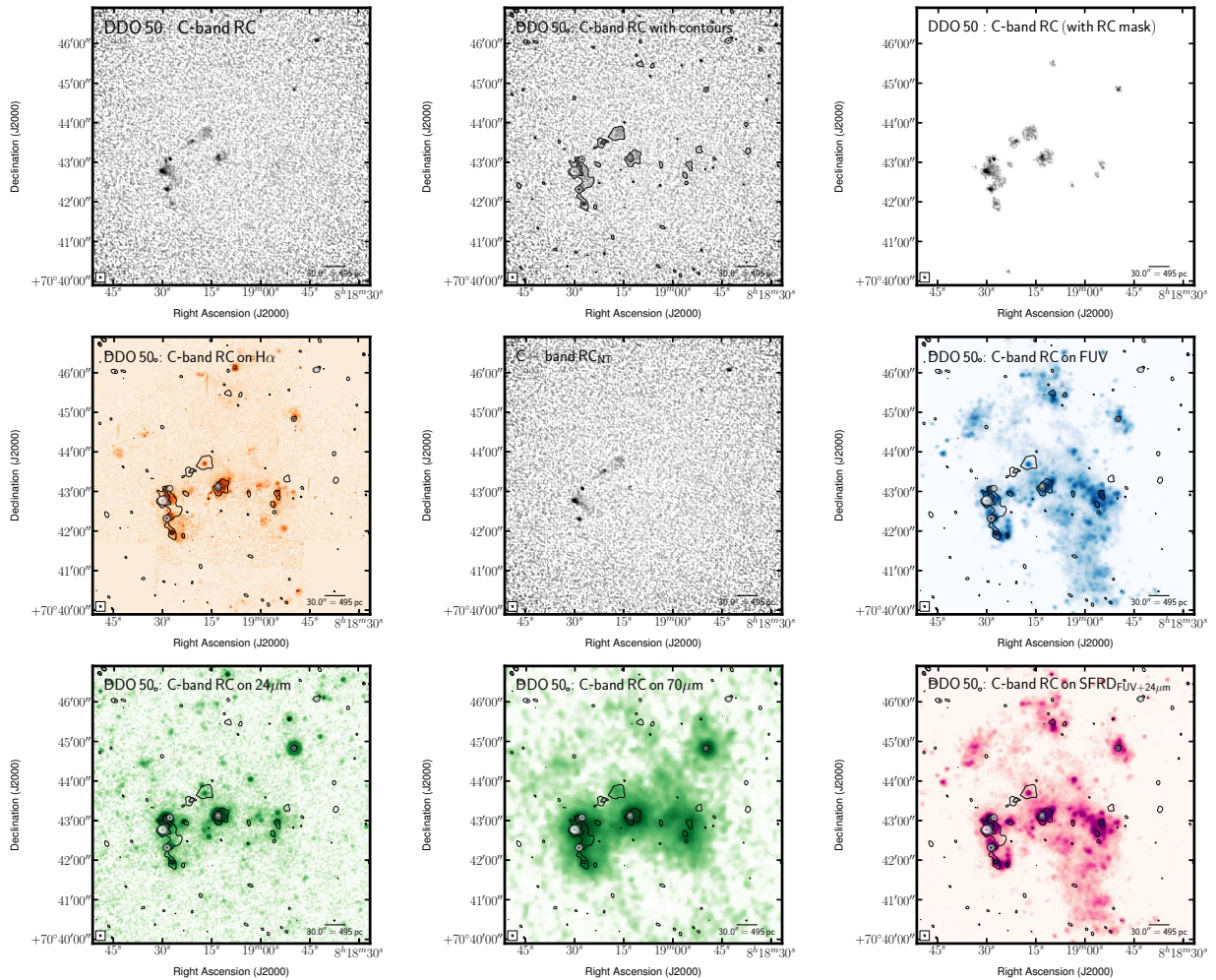


Fig. 16.— Multi-wavelength coverage of DDO 50 displaying a $7' \times 7'$ area. We show total RC flux density at the native resolution (top left) and again with contours (top centre). The lowest contour highlights low-surface brightness emission at a level of $21.9 \mu\text{Jy beam}^{-1}$ —this is 2.5 times the rms after smoothing the native image by a factor of 2.5. The other contours are placed following $(2 + 2^n)\sigma_{\text{native}}$, where $n \geq 0$ and both the rms ($\sigma_{\text{native}} = 6.11 \mu\text{Jy beam}^{-1}$) and the resolution ($\text{FWHM}_{\text{native}} = 3.1 \times 2.4$ arcsec) are taken from the native resolution image. These same contours are also superposed on ancillary LITTLE THINGS images where possible: $\text{H}\alpha$ (middle left); RC_{NTh} inferred from Deeg et al. 1997 (middle centre); *GALEX* FUV (middle right); *Spitzer* $24 \mu\text{m}$ (bottom left); *Spitzer* $70 \mu\text{m}$ (bottom centre); FUV+ $24 \mu\text{m}$ -inferred SFRD from Leroy et al. 2012 (bottom right). We also show the RC that was isolated by the RC-based masking technique (top right). The greyscale intensity scales used are arbitrary to best highlight structure.

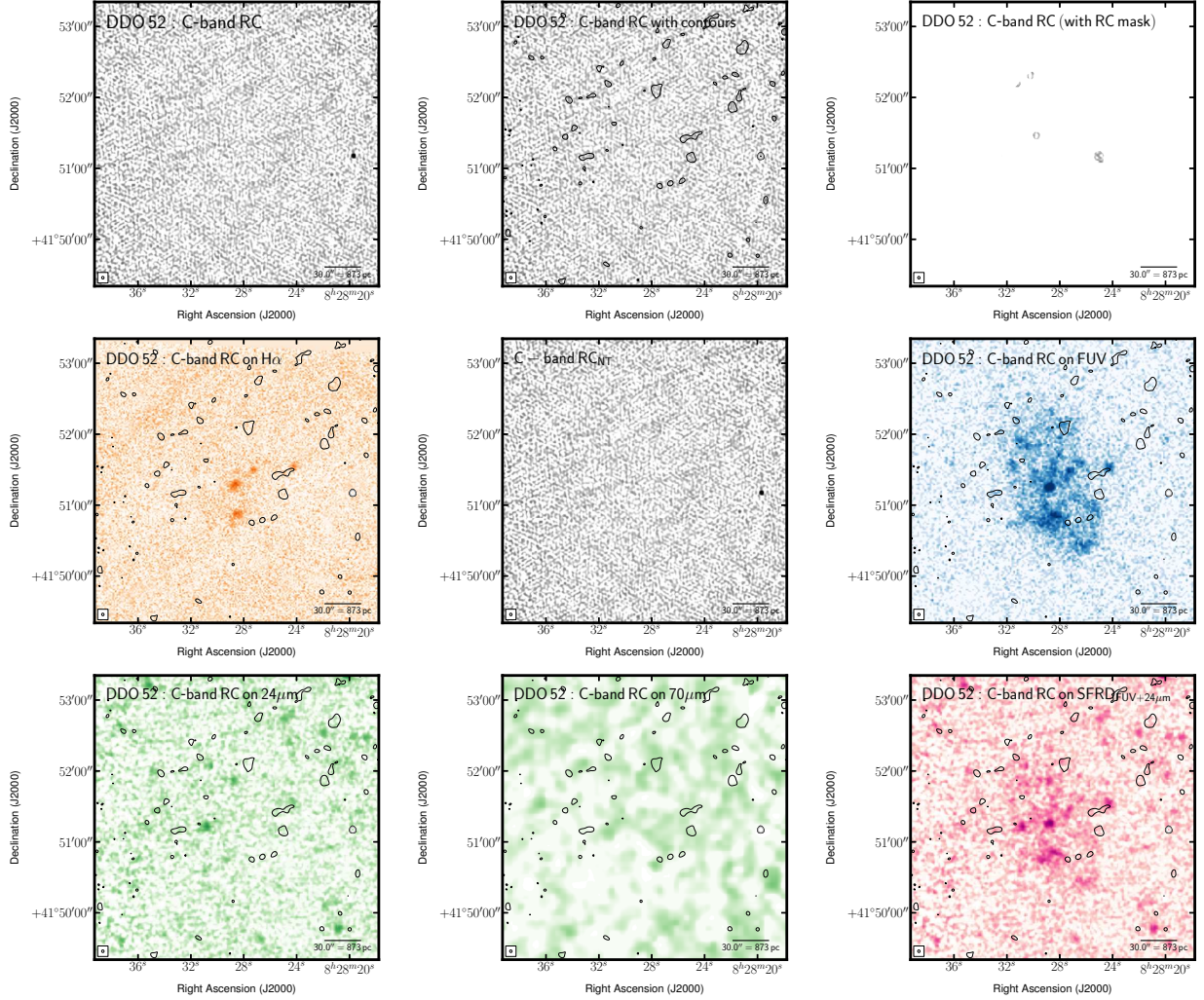


Fig. 17.— Multi-wavelength coverage of DDO 52 displaying a $4' \times 4'$ area. We show total RC flux density at the native resolution (top left) and again with contours (top centre). The lowest contour highlights low-surface brightness emission at a level of $29.8 \mu\text{Jy beam}^{-1}$ —this is 2.5 times the rms after smoothing the native image by a factor of 2.5. The other contours are placed following $(2 + 2^n)\sigma_{\text{native}}$, where $n \geq 0$ and both the rms ($\sigma_{\text{native}} = 8.29 \mu\text{Jy beam}^{-1}$) and the resolution ($\text{FWHM}_{\text{native}} = 2.2 \times 2.0$ arcsec) are taken from the native resolution image. These same contours are also superposed on ancillary LITTLE THINGS images where possible: $\text{H}\alpha$ (middle left); RC_{NTh} inferred from Deeg et al. 1997 (middle centre); *GALEX* FUV (middle right); *Spitzer* $24 \mu\text{m}$ (bottom left); *Spitzer* $70 \mu\text{m}$ (bottom centre); FUV+ $24 \mu\text{m}$ -inferred SFRD from Leroy et al. 2012 (bottom right). We also show the RC that was isolated by the RC-based masking technique (top right). The greyscale intensity scales used are arbitrary to best highlight structure.

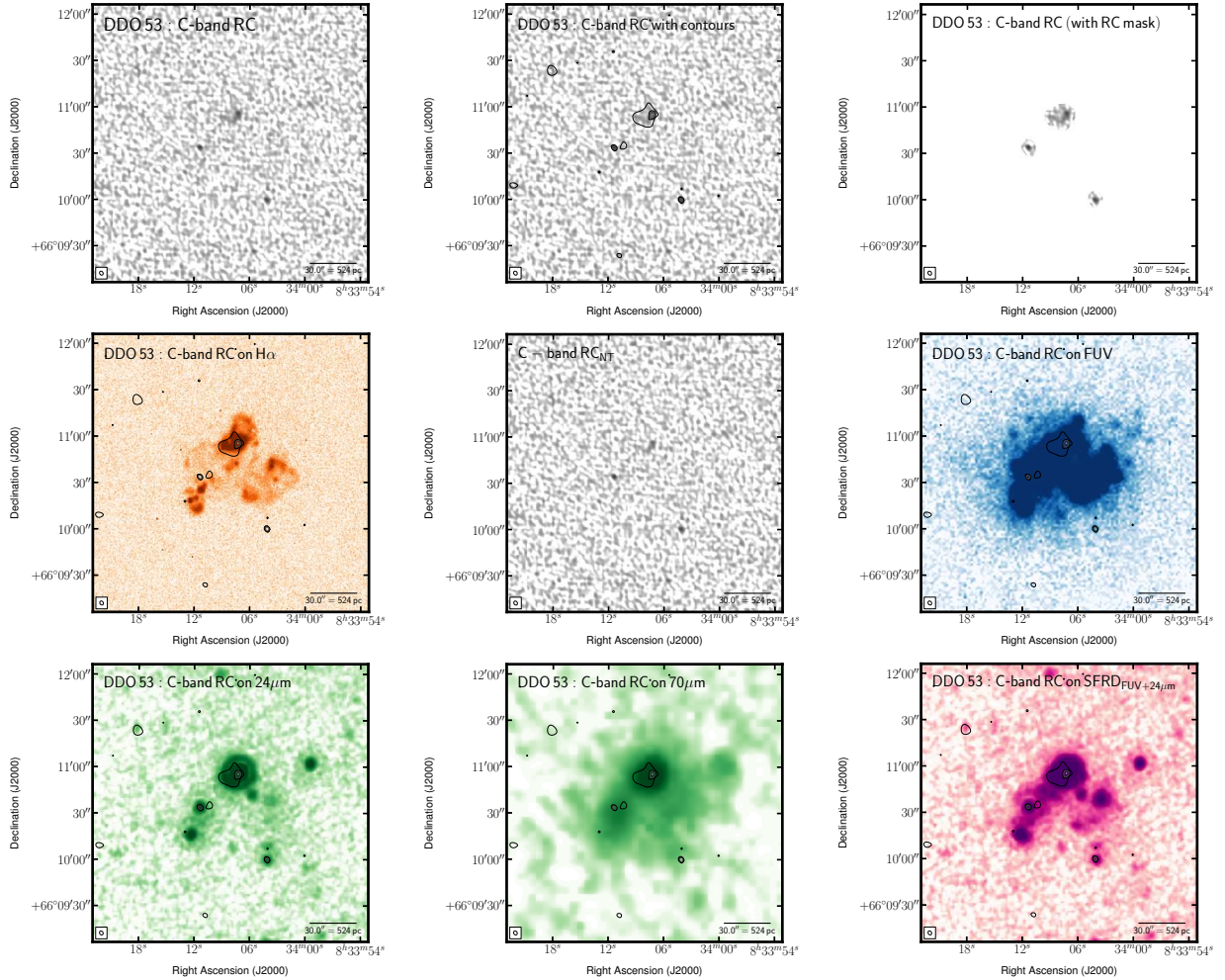


Fig. 18.— Multi-wavelength coverage of DDO 53 displaying a $3' \times 3'$ area. We show total RC flux density at the native resolution (top left) and again with contours (top centre). The lowest contour highlights low-surface brightness emission at a level of $28.6 \mu\text{Jy beam}^{-1}$ —this is 2.5 times the rms after smoothing the native image by a factor of 2.5. The other contours are placed following $(2 + 2^n)\sigma_{\text{native}}$, where $n \geq 0$ and both the rms ($\sigma_{\text{native}} = 6.49 \mu\text{Jy beam}^{-1}$) and the resolution ($\text{FWHM}_{\text{native}} = 2.8 \times 2.2$ arcsec) are taken from the native resolution image. These same contours are also superposed on ancillary LITTLE THINGS images where possible: $\text{H}\alpha$ (middle left); RC_{NTh} inferred from Deeg et al. 1997 (middle centre); *GALEX* FUV (middle right); *Spitzer* $24 \mu\text{m}$ (bottom left); *Spitzer* $70 \mu\text{m}$ (bottom centre); FUV+ $24 \mu\text{m}$ -inferred SFRD from Leroy et al. 2012 (bottom right). We also show the RC that was isolated by the RC-based masking technique (top right). The greyscale intensity scales used are arbitrary to best highlight structure.

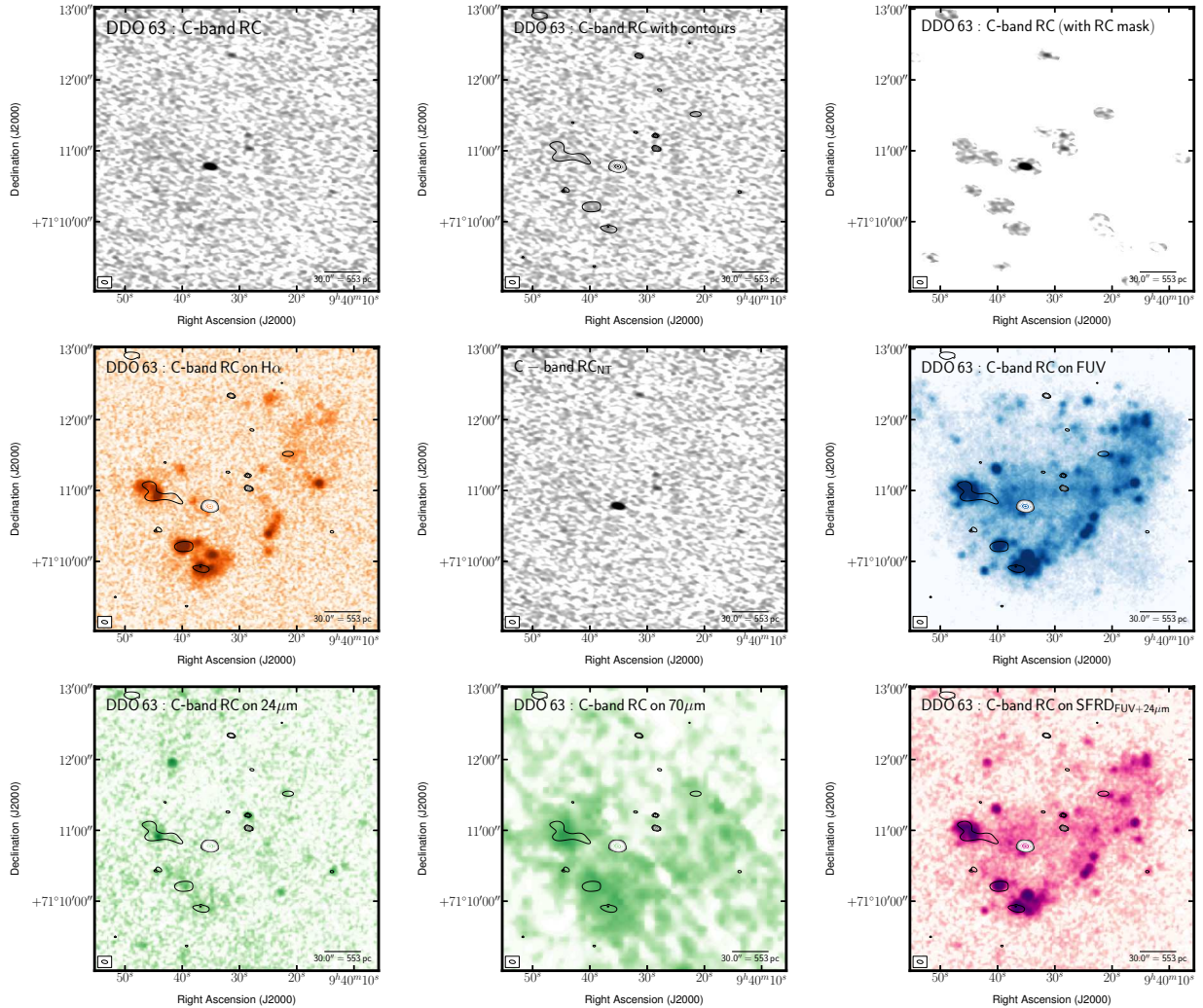


Fig. 19.— Multi-wavelength coverage of DDO 63 displaying a $4' \times 4'$ area. We show total RC flux density at the native resolution (top left) and again with contours (top centre). The lowest contour highlights low-surface brightness emission at a level of $24.6 \mu\text{Jy beam}^{-1}$ —this is 2.5 times the rms after smoothing the native image by a factor of 2.5. The other contours are placed following $(2 + 2^n)\sigma_{\text{native}}$, where $n \geq 0$ and both the rms ($\sigma_{\text{native}} = 4.96 \mu\text{Jy beam}^{-1}$) and the resolution ($\text{FWHM}_{\text{native}} = 5.1 \times 2.8 \text{ arcsec}$) are taken from the native resolution image. These same contours are also superposed on ancillary LITTLE THINGS images where possible: $\text{H}\alpha$ (middle left); RC_{NT} inferred from Deeg et al. 1997 (middle centre); *GALEX* FUV (middle right); *Spitzer* $24 \mu\text{m}$ (bottom left); *Spitzer* $70 \mu\text{m}$ (bottom centre); FUV+ $24 \mu\text{m}$ -inferred SFRD from Leroy et al. 2012 (bottom right). We also show the RC that was isolated by the RC-based masking technique (top right). The greyscale intensity scales used are arbitrary to best highlight structure.

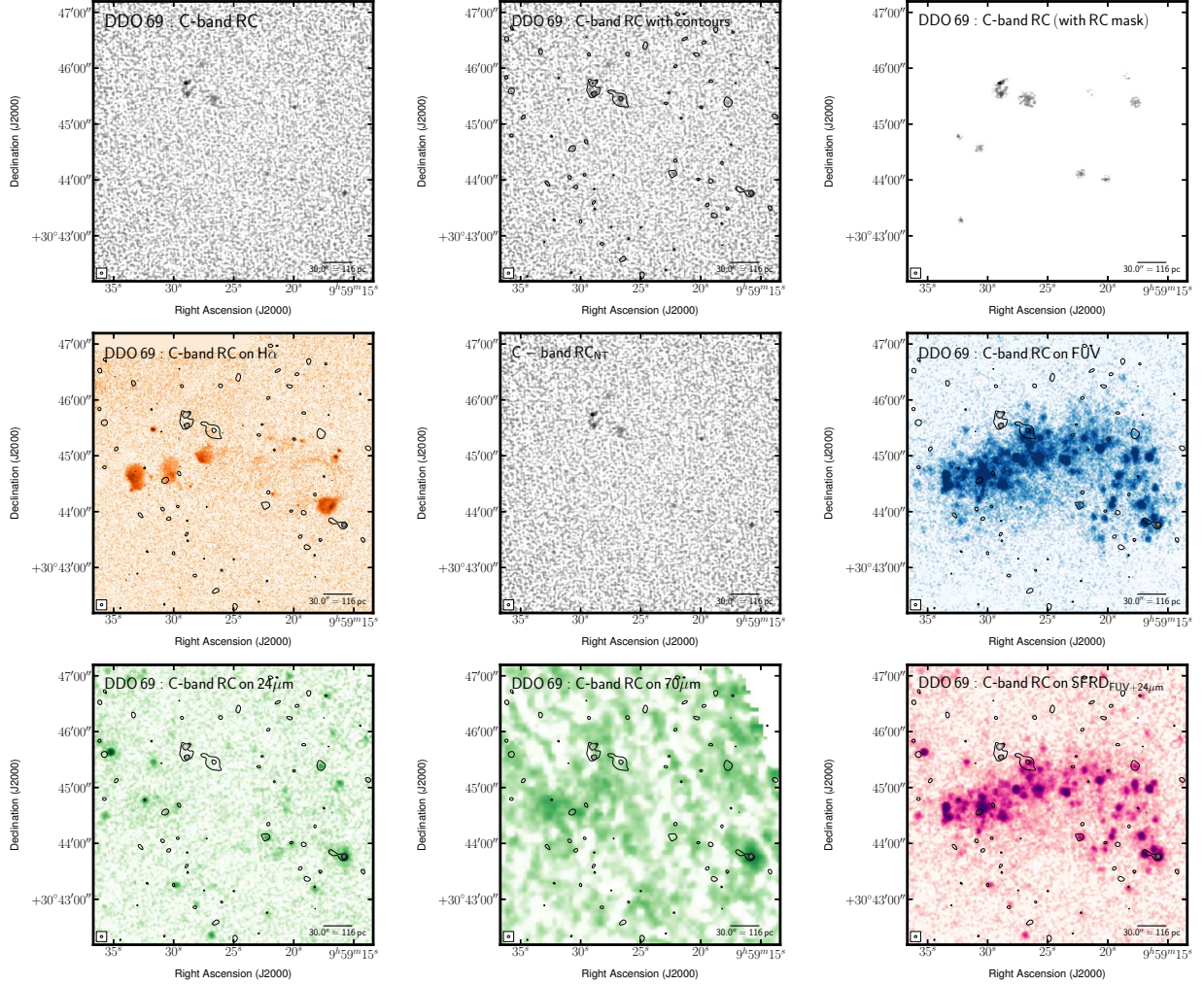


Fig. 20.— Multi-wavelength coverage of DDO 69 displaying a $5' \times 5'$ area. We show total RC flux density at the native resolution (top left) and again with contours (top centre). The lowest contour highlights low-surface brightness emission at a level of $18.1 \mu\text{Jy beam}^{-1}$ —this is 2.5 times the rms after smoothing the native image by a factor of 2.5. The other contours are placed following $(2 + 2^n)\sigma_{\text{native}}$, where $n \geq 0$ and both the rms ($\sigma_{\text{native}} = 5.88 \mu\text{Jy beam}^{-1}$) and the resolution ($\text{FWHM}_{\text{native}} = 2.7 \times 2.5$ arcsec) are taken from the native resolution image. These same contours are also superposed on ancillary LITTLE THINGS images where possible: $\text{H}\alpha$ (middle left); RC_{NTh} inferred from Deeg et al. 1997 (middle centre); *GALEX* FUV (middle right); *Spitzer* $24 \mu\text{m}$ (bottom left); *Spitzer* $70 \mu\text{m}$ (bottom centre); FUV+ $24 \mu\text{m}$ -inferred SFRD from Leroy et al. 2012 (bottom right). We also show the RC that was isolated by the RC-based masking technique (top right). The greyscale intensity scales used are arbitrary to best highlight structure.

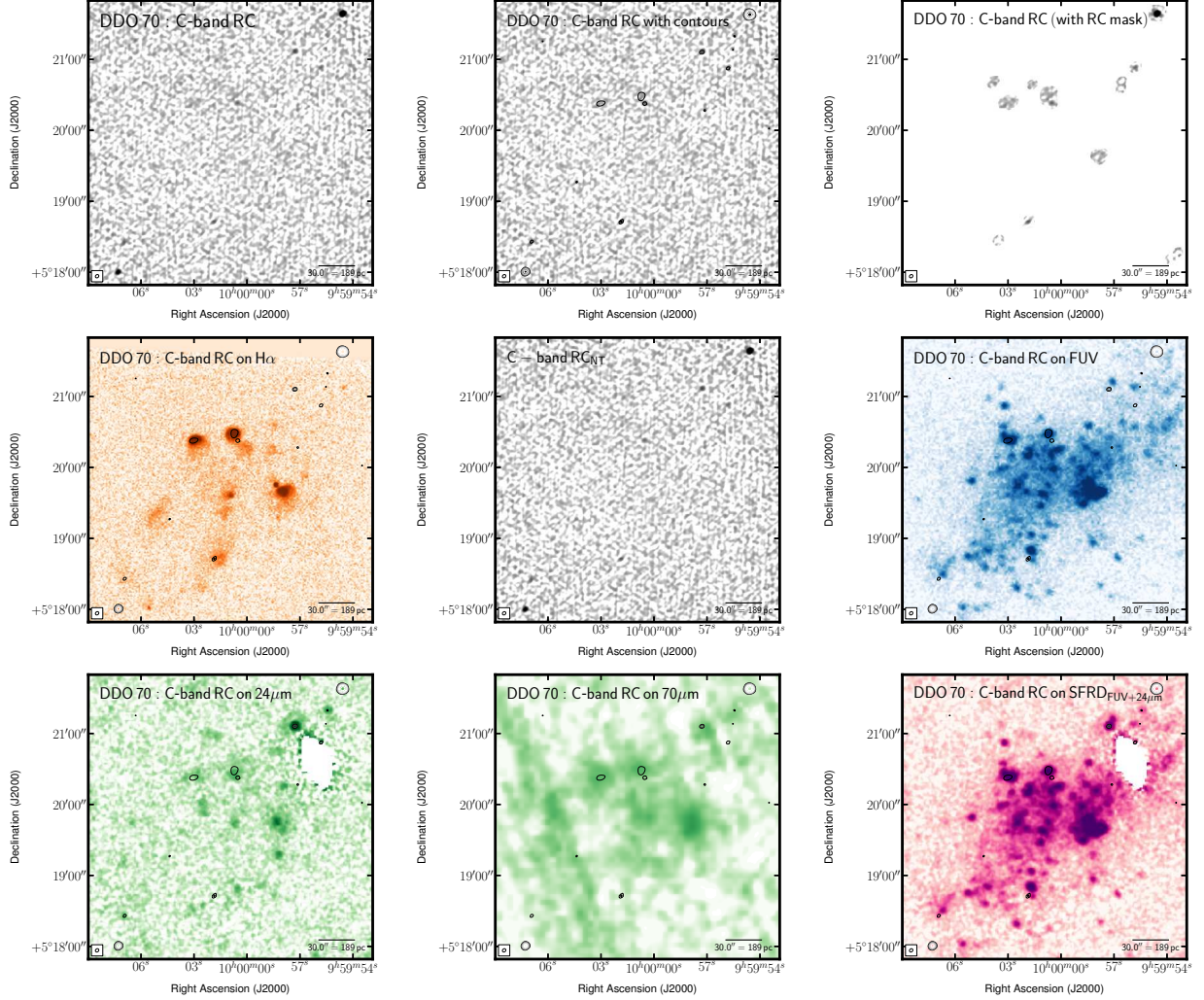


Fig. 21.— Multi-wavelength coverage of DDO 70 displaying a $4' \times 4'$ area. We show total RC flux density at the native resolution (top left) and again with contours (top centre). The lowest contour highlights low-surface brightness emission at a level of $41.7 \mu\text{Jy beam}^{-1}$ —this is 2.5 times the rms after smoothing the native image by a factor of 2.5. The other contours are placed following $(2 + 2^n)\sigma_{\text{native}}$, where $n \geq 0$ and both the rms ($\sigma_{\text{native}} = 6.33 \mu\text{Jy beam}^{-1}$) and the resolution ($\text{FWHM}_{\text{native}} = 3.1 \times 2.6$ arcsec) are taken from the native resolution image. These same contours are also superposed on ancillary LITTLE THINGS images where possible: $\text{H}\alpha$ (middle left); RC_{NT} inferred from Deeg et al. 1997 (middle centre); *GALEX* FUV (middle right); *Spitzer* $24 \mu\text{m}$ (bottom left); *Spitzer* $70 \mu\text{m}$ (bottom centre); FUV+ $24 \mu\text{m}$ -inferred SFRD from Leroy et al. 2012 (bottom right). We also show the RC that was isolated by the RC-based masking technique (top right). The greyscale intensity scales used are arbitrary to best highlight structure.

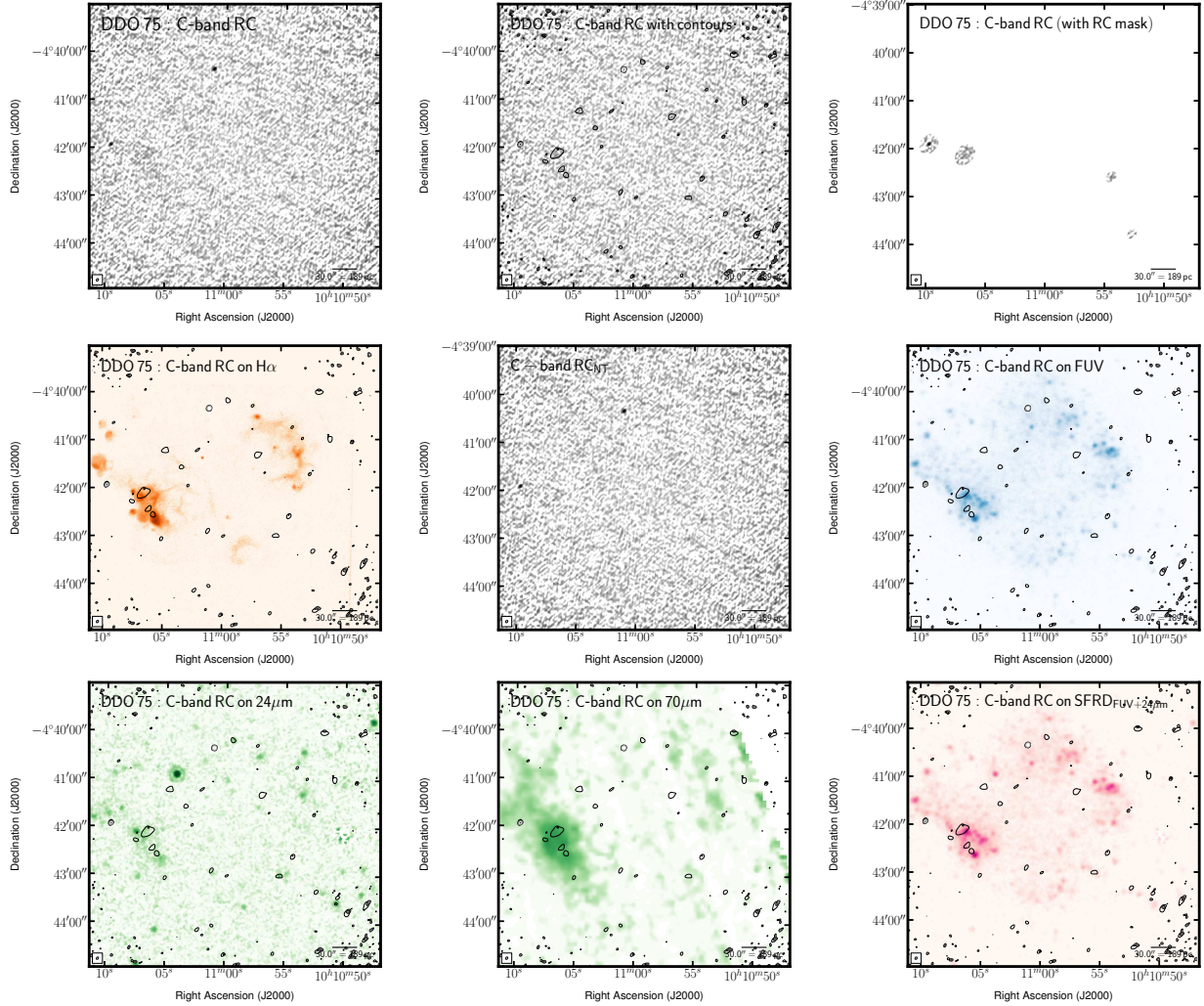


Fig. 22.— Multi-wavelength coverage of DDO 75 displaying a $7' \times 7'$ area. We show total RC flux density at the native resolution (top left) and again with contours (top centre). The lowest contour highlights low-surface brightness emission at a level of $48.7 \mu\text{Jy beam}^{-1}$ —this is 2.5 times the rms after smoothing the native image by a factor of 2.5. The other contours are placed following $(2 + 2^n)\sigma_{\text{native}}$, where $n \geq 0$ and both the rms ($\sigma_{\text{native}} = 9.66 \mu\text{Jy beam}^{-1}$) and the resolution ($\text{FWHM}_{\text{native}} = 3.3 \times 2.4$ arcsec) are taken from the native resolution image. These same contours are also superposed on ancillary LITTLE THINGS images where possible: $\text{H}\alpha$ (middle left); RC_{NTh} inferred from Deeg et al. 1997 (middle centre); *GALEX* FUV (middle right); *Spitzer* $24 \mu\text{m}$ (bottom left); *Spitzer* $70 \mu\text{m}$ (bottom centre); FUV+ $24 \mu\text{m}$ -inferred SFRD from Leroy et al. 2012 (bottom right). We also show the RC that was isolated by the RC-based masking technique (top right). The greyscale intensity scales used are arbitrary to best highlight structure.

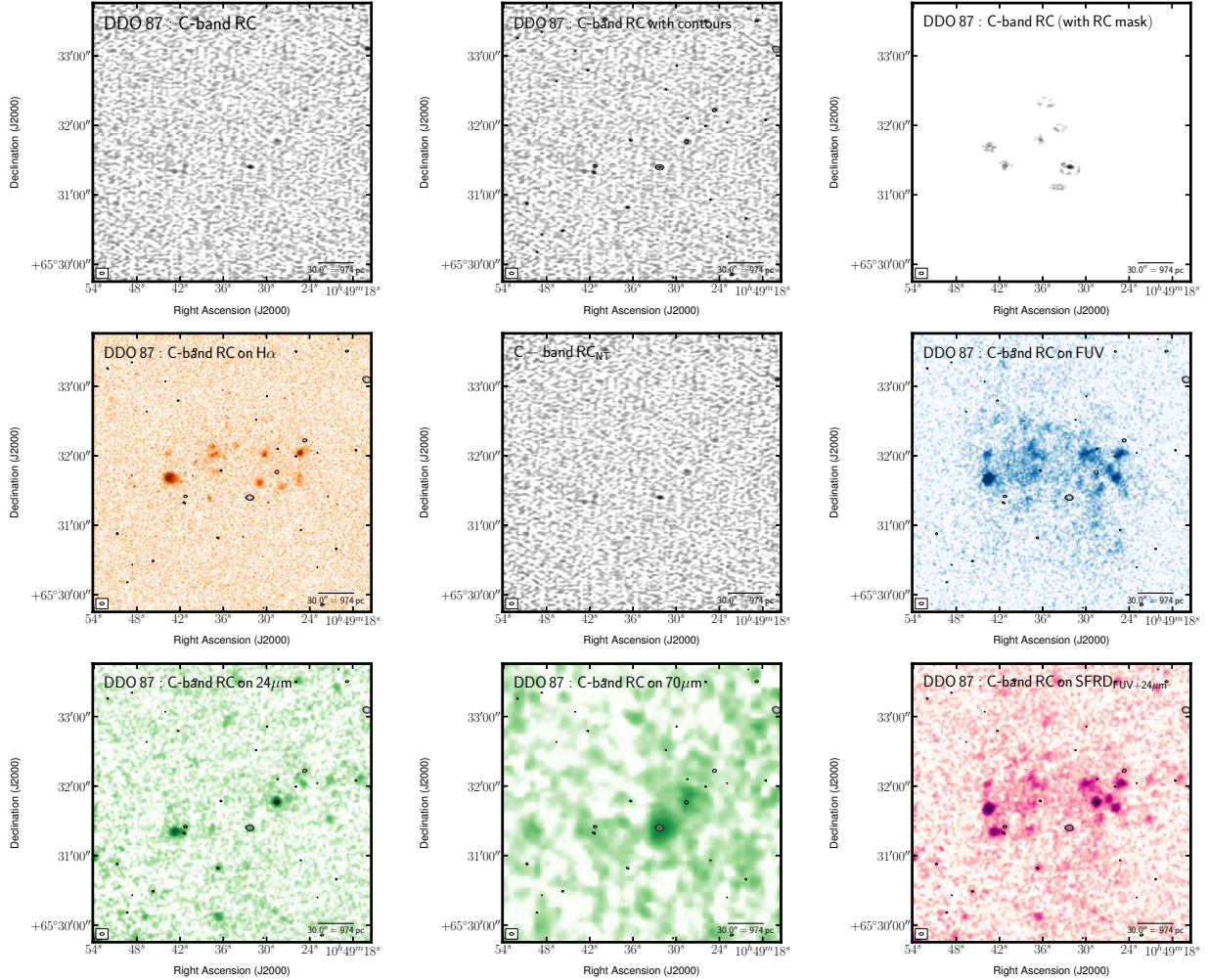


Fig. 23.— Multi-wavelength coverage of DDO 87 displaying a $4' \times 4'$ area. We show total RC flux density at the native resolution (top left) and again with contours (top centre). The lowest contour highlights low-surface brightness emission at a level of $30.1 \mu\text{Jy beam}^{-1}$ —this is 2.5 times the rms after smoothing the native image by a factor of 2.5. The other contours are placed following $(2 + 2^n)\sigma_{\text{native}}$, where $n \geq 0$ and both the rms ($\sigma_{\text{native}} = 6.21 \mu\text{Jy beam}^{-1}$) and the resolution ($\text{FWHM}_{\text{native}} = 3.8 \times 2.2 \text{ arcsec}$) are taken from the native resolution image. These same contours are also superposed on ancillary LITTLE THINGS images where possible: $\text{H}\alpha$ (middle left); RC_{NTh} inferred from Deeg et al. 1997 (middle centre); *GALEX* FUV (middle right); *Spitzer* $24 \mu\text{m}$ (bottom left); *Spitzer* $70 \mu\text{m}$ (bottom centre); FUV+ $24 \mu\text{m}$ -inferred SFRD from Leroy et al. 2012 (bottom right). We also show the RC that was isolated by the RC-based masking technique (top right). The greyscale intensity scales used are arbitrary to best highlight structure.

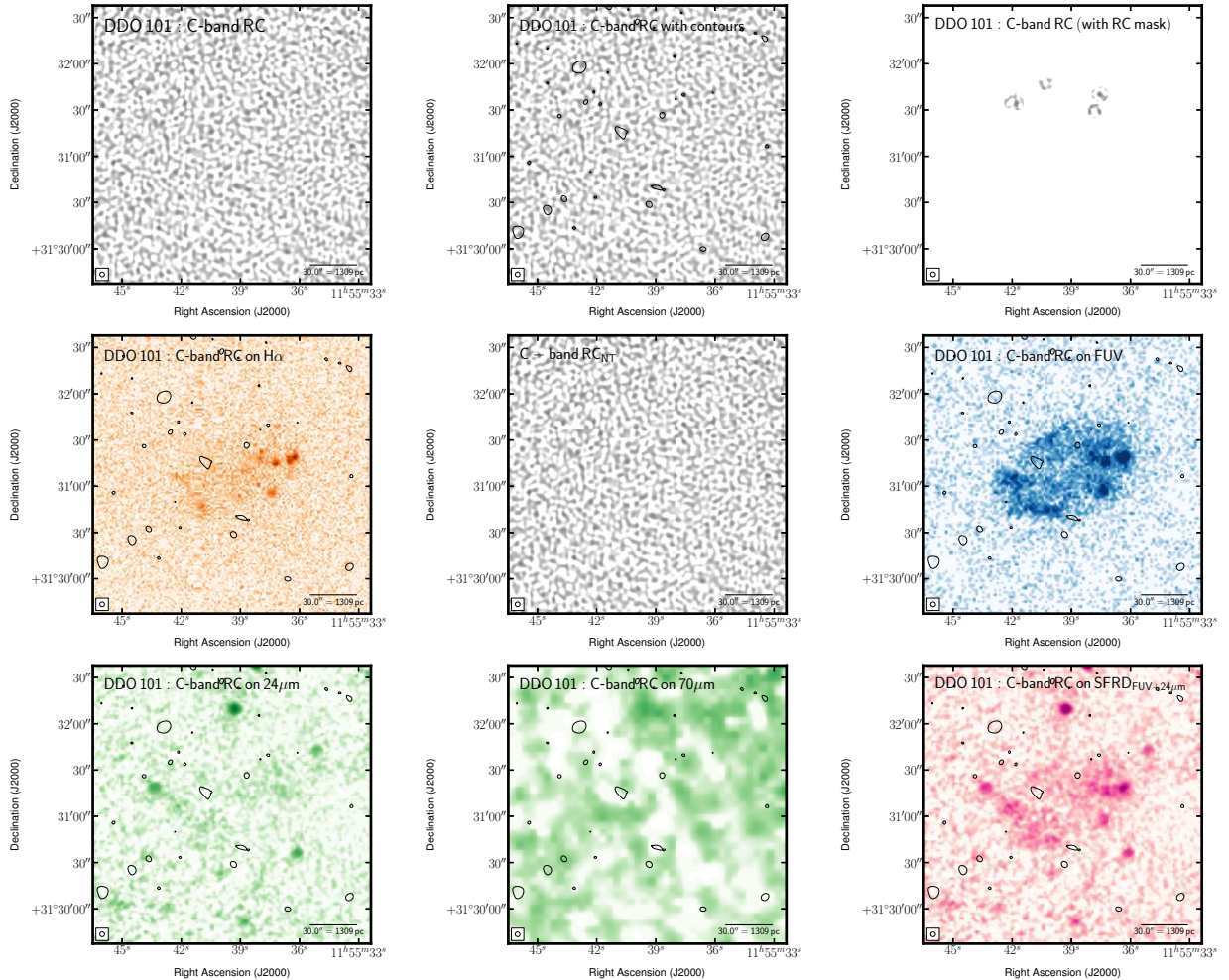


Fig. 24.— Multi-wavelength coverage of DDO 101 displaying a $3' \times 3'$ area. We show total RC flux density at the native resolution (top left) and again with contours (top centre). The lowest contour highlights low-surface brightness emission at a level of $39.8 \mu\text{Jy beam}^{-1}$ —this is 2.5 times the rms after smoothing the native image by a factor of 2.5. The other contours are placed following $(2 + 2^n)\sigma_{\text{native}}$, where $n \geq 0$ and both the rms ($\sigma_{\text{native}} = 15.09 \mu\text{Jy beam}^{-1}$) and the resolution ($\text{FWHM}_{\text{native}} = 3.1 \times 3.0$ arcsec) are taken from the native resolution image. These same contours are also superposed on ancillary LITTLE THINGS images where possible: $\text{H}\alpha$ (middle left); RC_{NTh} inferred from Deeg et al. 1997 (middle centre); *GALEX* FUV (middle right); *Spitzer* $24 \mu\text{m}$ (bottom left); *Spitzer* $70 \mu\text{m}$ (bottom centre); FUV+ $24 \mu\text{m}$ —inferred SFRD from Leroy et al. 2012 (bottom right). We also show the RC that was isolated by the RC-based masking technique (top right). The greyscale intensity scales used are arbitrary to best highlight structure.

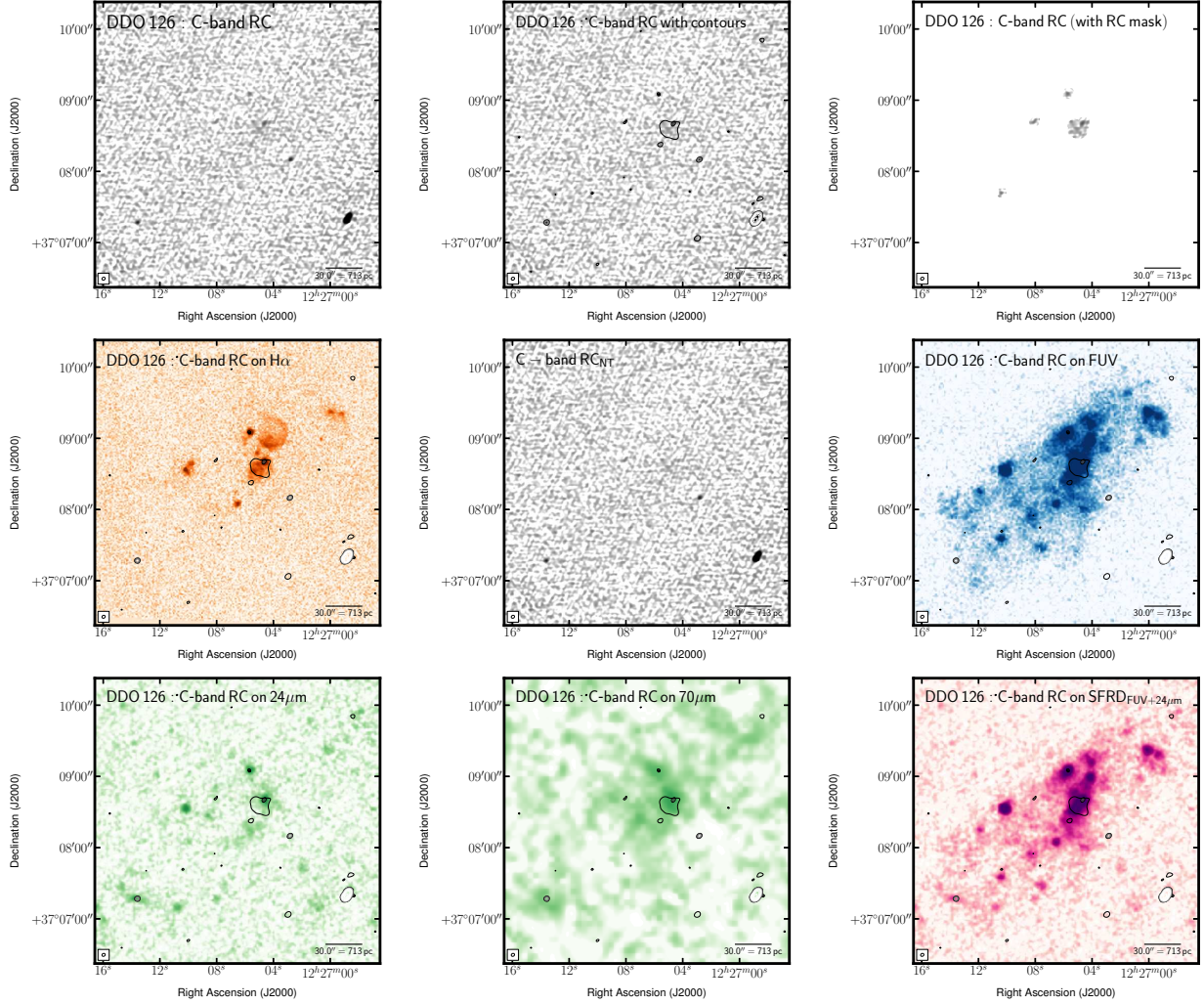


Fig. 25.— Multi-wavelength coverage of DDO 126 displaying a $4' \times 4'$ area. We show total RC flux density at the native resolution (top left) and again with contours (top centre). The lowest contour highlights low-surface brightness emission at a level of $30.6 \mu\text{Jy beam}^{-1}$ —this is 2.5 times the rms after smoothing the native image by a factor of 2.5. The other contours are placed following $(2 + 2^n)\sigma_{\text{native}}$, where $n \geq 0$ and both the rms ($\sigma_{\text{native}} = 6.90 \mu\text{Jy beam}^{-1}$) and the resolution ($\text{FWHM}_{\text{native}} = 2.9 \times 2.4$ arcsec) are taken from the native resolution image. These same contours are also superposed on ancillary LITTLE THINGS images where possible: $\text{H}\alpha$ (middle left); RC_{NT} inferred from Deeg et al. 1997 (middle centre); *GALEX* FUV (middle right); *Spitzer* $24 \mu\text{m}$ (bottom left); *Spitzer* $70 \mu\text{m}$ (bottom centre); FUV+ $24 \mu\text{m}$ —inferred SFRD from Leroy et al. 2012 (bottom right). We also show the RC that was isolated by the RC-based masking technique (top right). The greyscale intensity scales used are arbitrary to best highlight structure.

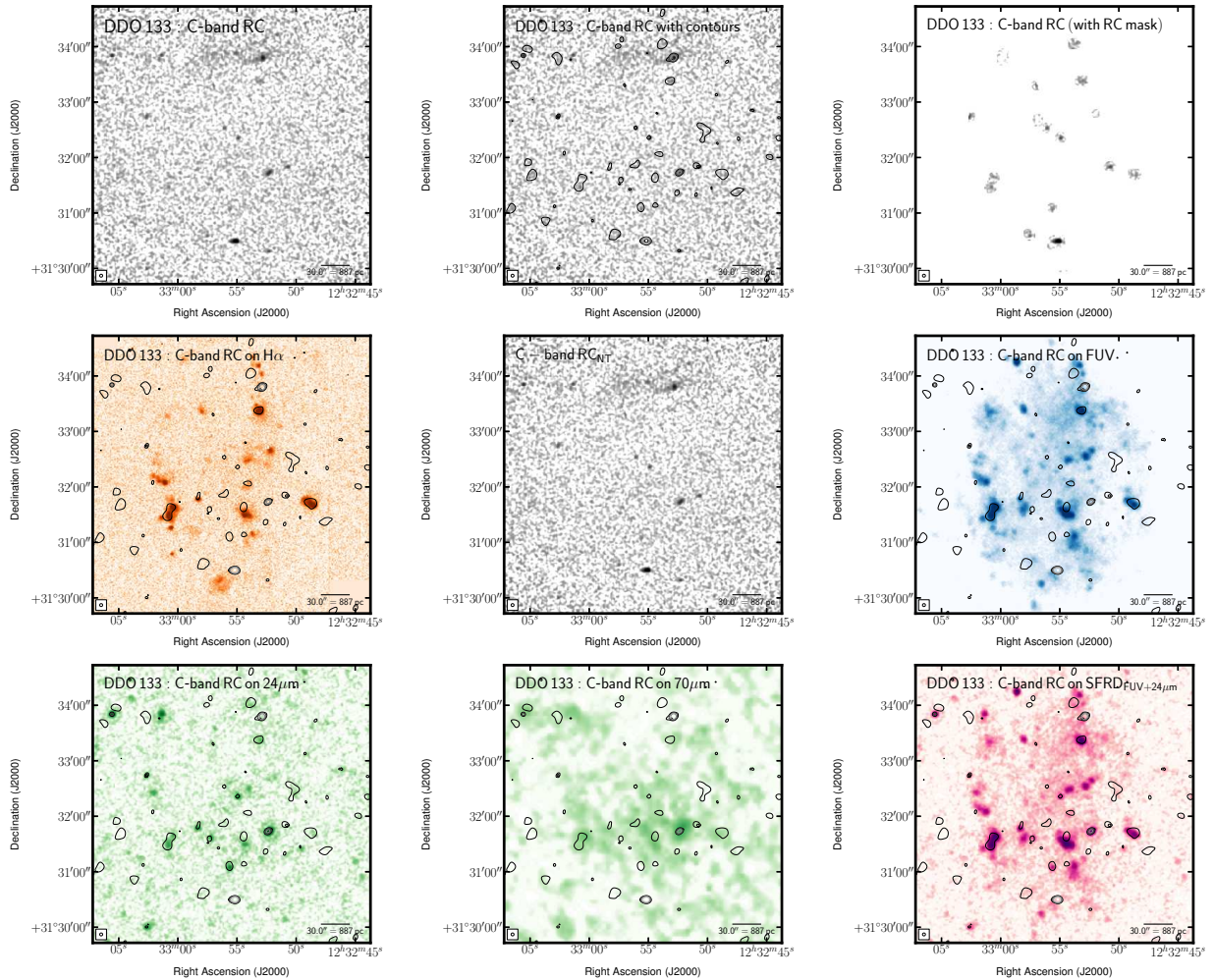


Fig. 26.— Multi-wavelength coverage of DDO 133 displaying a $5' \times 5'$ area. We show total RC flux density at the native resolution (top left) and again with contours (top centre). The lowest contour highlights low-surface brightness emission at a level of $16.8 \mu\text{Jy beam}^{-1}$ —this is 2.5 times the rms after smoothing the native image by a factor of 2.5. The other contours are placed following $(2 + 2^n)\sigma_{\text{native}}$, where $n \geq 0$ and both the rms ($\sigma_{\text{native}} = 4.92 \mu\text{Jy beam}^{-1}$) and the resolution ($\text{FWHM}_{\text{native}} = 3.2 \times 3.2 \text{ arcsec}$) are taken from the native resolution image. These same contours are also superposed on ancillary LITTLE THINGS images where possible: $\text{H}\alpha$ (middle left); RC_{NTh} inferred from Deeg et al. 1997 (middle centre); *GALEX* FUV (middle right); *Spitzer* $24 \mu\text{m}$ (bottom left); *Spitzer* $70 \mu\text{m}$ (bottom centre); FUV+ $24 \mu\text{m}$ —inferred SFRD from Leroy et al. 2012 (bottom right). We also show the RC that was isolated by the RC-based masking technique (top right). The greyscale intensity scales used are arbitrary to best highlight structure.

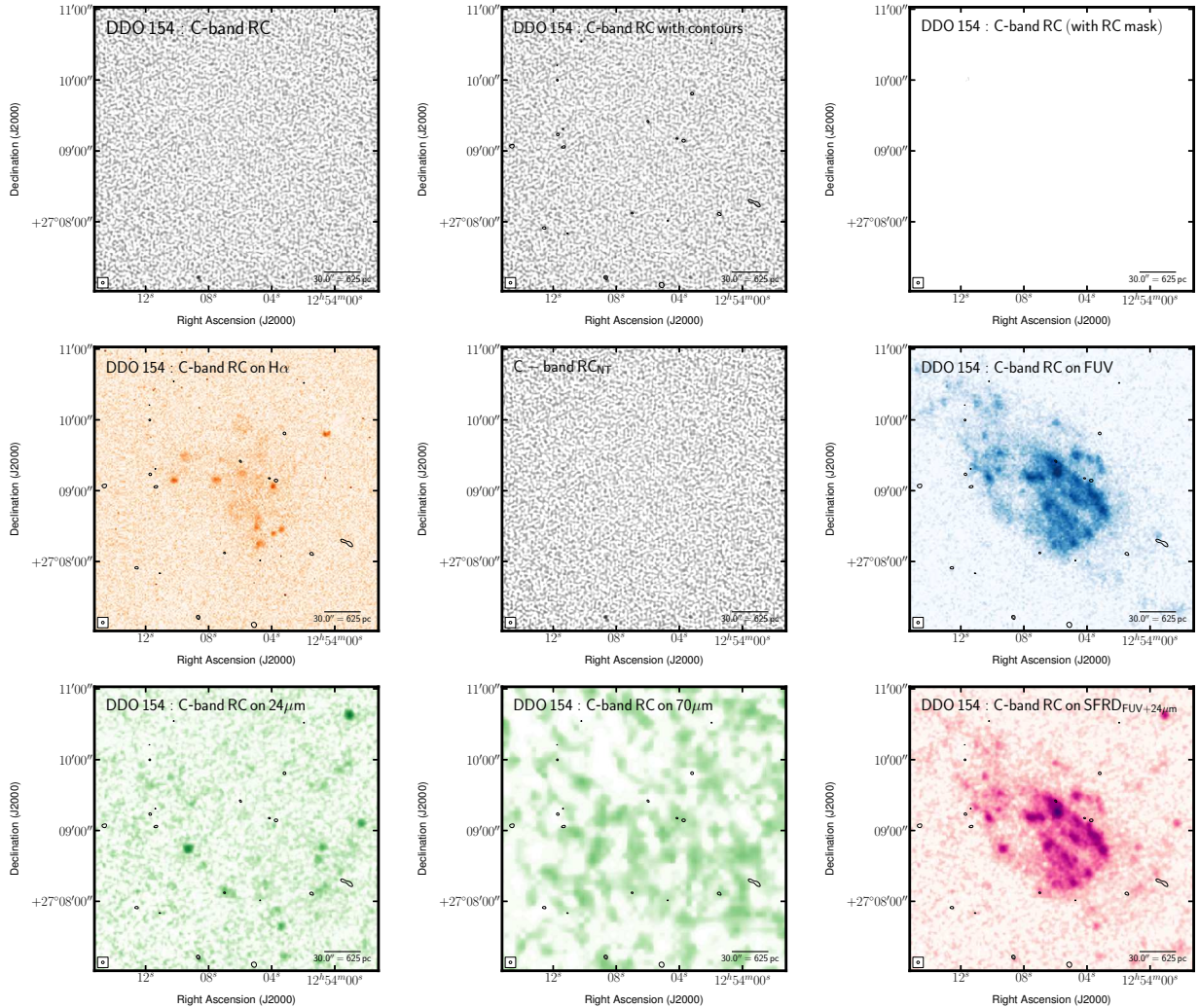


Fig. 27.— Multi-wavelength coverage of DDO 154 displaying a $4' \times 4'$ area. We show total RC flux density at the native resolution (top left) and again with contours (top centre). The lowest contour highlights low-surface brightness emission at a level of $19.0 \mu\text{Jy beam}^{-1}$ —this is 2.5 times the rms after smoothing the native image by a factor of 2.5. The other contours are placed following $(2 + 2^n)\sigma_{\text{native}}$, where $n \geq 0$ and both the rms ($\sigma_{\text{native}} = 7.29 \mu\text{Jy beam}^{-1}$) and the resolution ($\text{FWHM}_{\text{native}} = 2.2 \times 2.2$ arcsec) are taken from the native resolution image. These same contours are also superposed on ancillary LITTLE THINGS images where possible: $\text{H}\alpha$ (middle left); RC_{NTh} inferred from Deeg et al. 1997 (middle centre); *GALEX* FUV (middle right); *Spitzer* $24 \mu\text{m}$ (bottom left); *Spitzer* $70 \mu\text{m}$ (bottom centre); FUV+ $24 \mu\text{m}$ —inferred SFRD from Leroy et al. 2012 (bottom right). We also show the RC that was isolated by the RC-based masking technique (top right). The greyscale intensity scales used are arbitrary to best highlight structure.

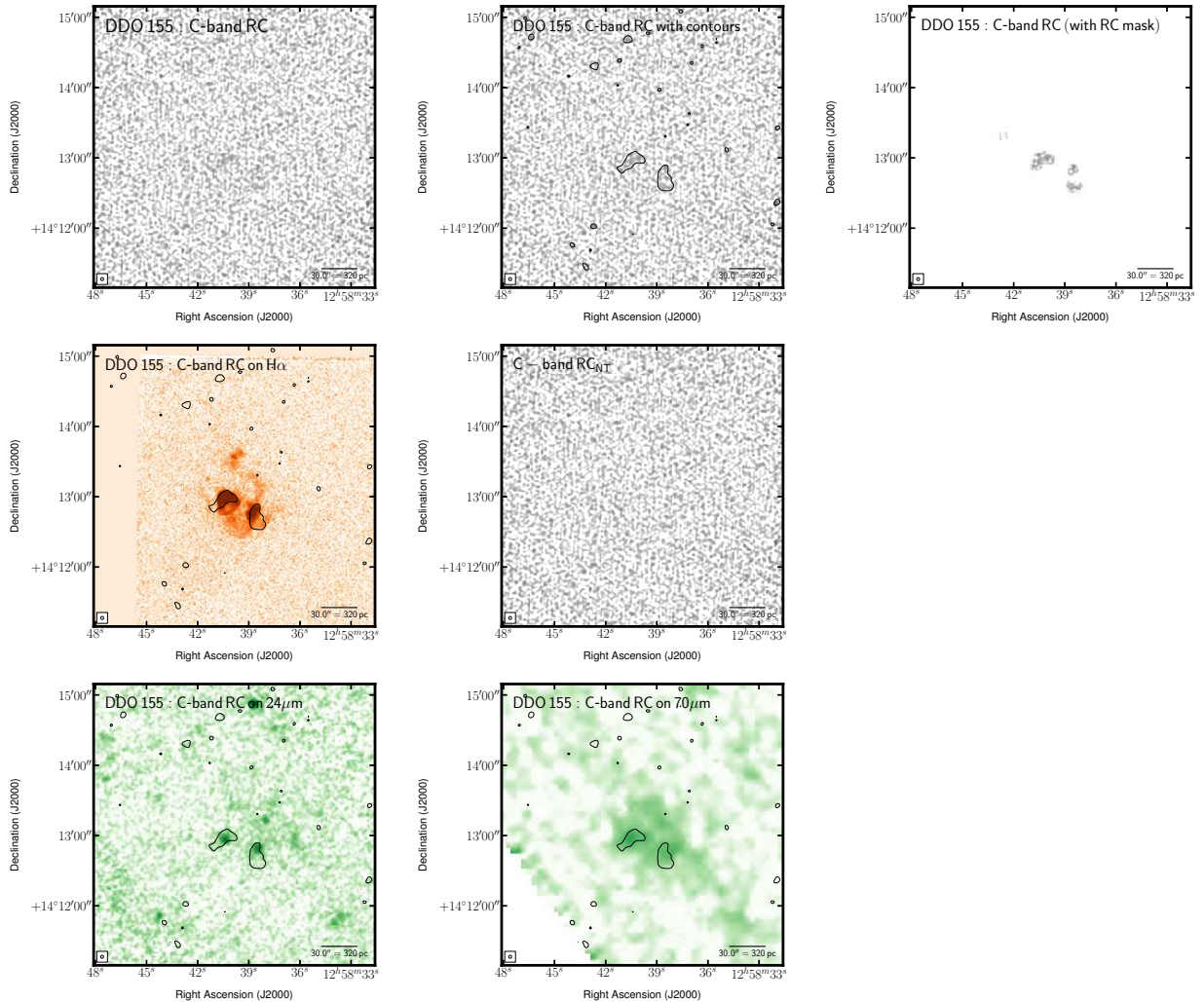


Fig. 28.— Multi-wavelength coverage of DDO 155 displaying a $4' \times 4'$ area. We show total RC flux density at the native resolution (top left) and again with contours (top centre). The lowest contour highlights low-surface brightness emission at a level of $21.1 \mu\text{Jy beam}^{-1}$ —this is 2.5 times the rms after smoothing the native image by a factor of 2.5. The other contours are placed following $(2 + 2^n)\sigma_{\text{native}}$, where $n \geq 0$ and both the rms ($\sigma_{\text{native}} = 6.36 \mu\text{Jy beam}^{-1}$) and the resolution ($\text{FWHM}_{\text{native}} = 2.6 \times 2.5 \text{ arcsec}$) are taken from the native resolution image. These same contours are also superposed on ancillary LITTLE THINGS images where possible: $\text{H}\alpha$ (middle left); RC_{NTh} inferred from Deeg et al. 1997 (middle centre); *Spitzer* $24 \mu\text{m}$ (bottom left); *Spitzer* $70 \mu\text{m}$ (bottom centre). We also show the RC that was isolated by the RC-based masking technique (top right). The greyscale intensity scales used are arbitrary to best highlight structure.

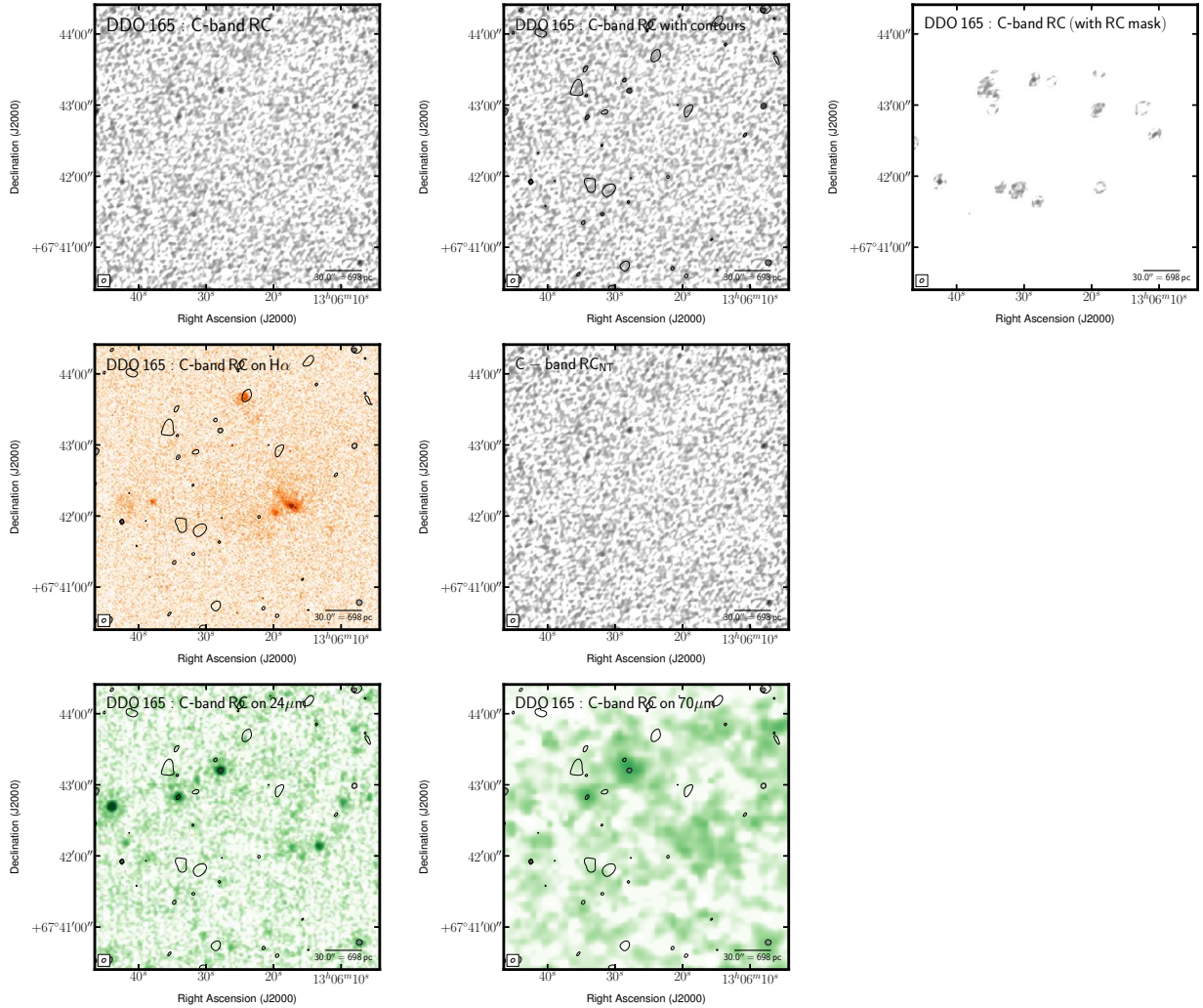


Fig. 29.— Multi-wavelength coverage of DDO 165 displaying a $4' \times 4'$ area. We show total RC flux density at the native resolution (top left) and again with contours (top centre). The lowest contour highlights low-surface brightness emission at a level of $19.0 \mu\text{Jy beam}^{-1}$ —this is 2.5 times the rms after smoothing the native image by a factor of 2.5. The other contours are placed following $(2 + 2^n)\sigma_{\text{native}}$, where $n \geq 0$ and both the rms ($\sigma_{\text{native}} = 4.54 \mu\text{Jy beam}^{-1}$) and the resolution ($\text{FWHM}_{\text{native}} = 3.7 \times 2.8 \text{ arcsec}$) are taken from the native resolution image. These same contours are also superposed on ancillary LITTLE THINGS images where possible: $\text{H}\alpha$ (middle left); RC_{NTh} inferred from Deeg et al. 1997 (middle centre); *Spitzer* $24 \mu\text{m}$ (bottom left); *Spitzer* $70 \mu\text{m}$ (bottom centre). We also show the RC that was isolated by the RC-based masking technique (top right). The greyscale intensity scales used are arbitrary to best highlight structure.

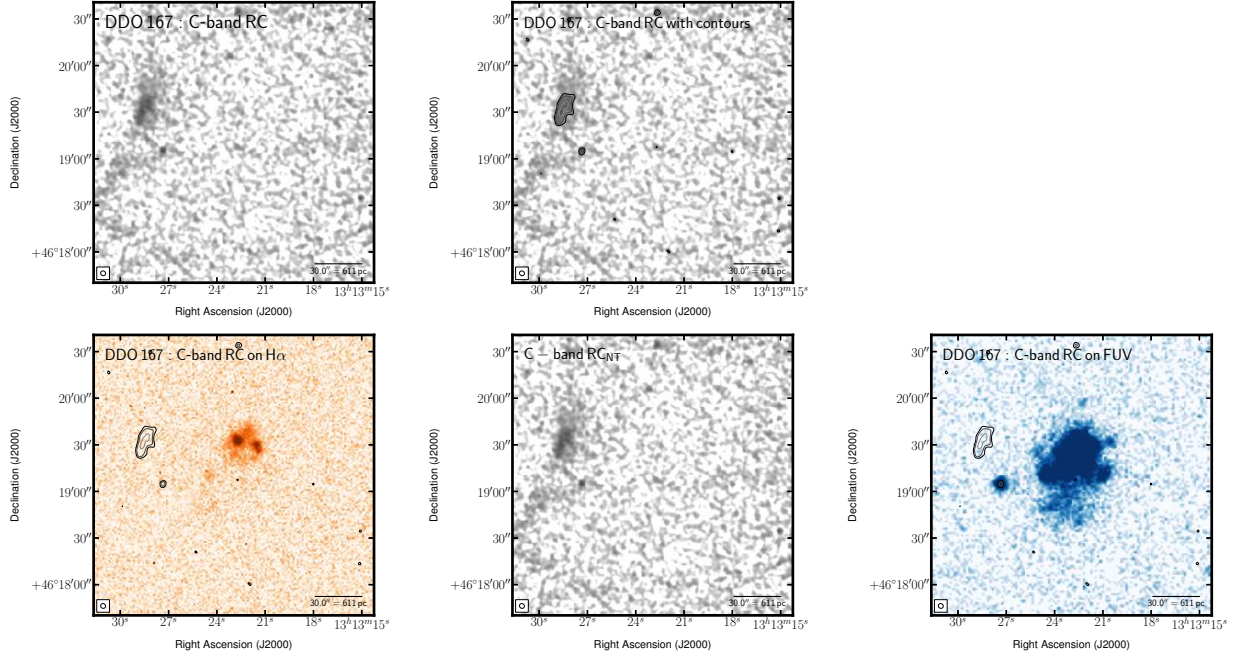


Fig. 30.— Multi-wavelength coverage of DDO 167 displaying a $3' \times 3'$ area. We show total RC flux density at the native resolution (top left) and again with contours (top centre). The lowest contour highlights low-surface brightness emission at a level of $38.6 \mu\text{Jy beam}^{-1}$ —this is 2.5 times the rms after smoothing the native image by a factor of 2.5. The other contours are placed following $(2 + 2^n)\sigma_{\text{native}}$, where $n \geq 0$ and both the rms ($\sigma_{\text{native}} = 5.11 \mu\text{Jy beam}^{-1}$) and the resolution ($\text{FWHM}_{\text{native}} = 3.3 \times 3.0 \text{ arcsec}$) are taken from the native resolution image. These same contours are also superposed on ancillary LITTLE THINGS images where possible: $\text{H}\alpha$ (middle left); RC_{NTTh} inferred from Deeg et al. 1997 (middle centre); *GALEX* FUV (middle right). No significant RC was observed. The greyscale intensity scales used are arbitrary to best highlight structure.

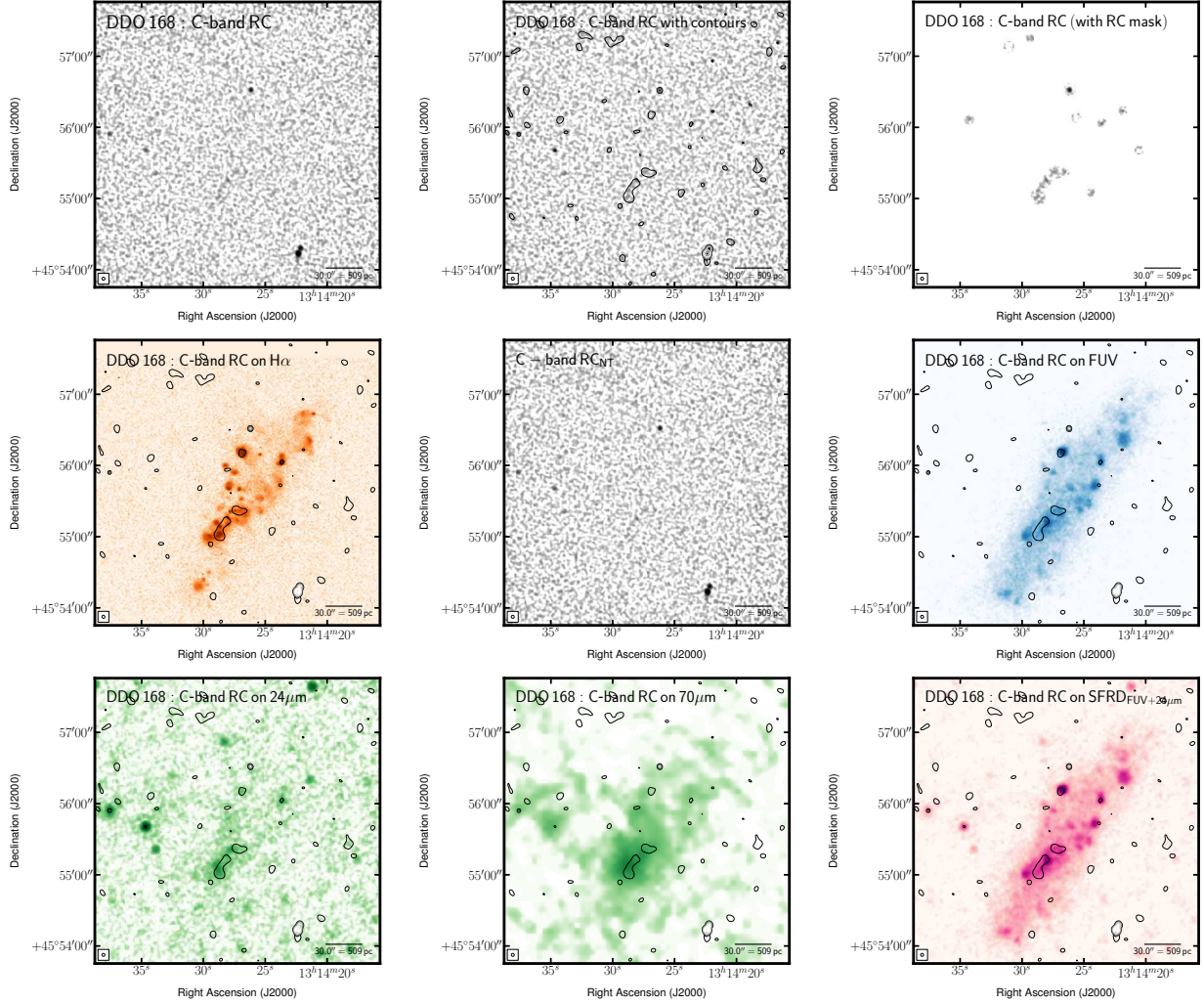


Fig. 31.— Multi-wavelength coverage of DDO 168 displaying a $4' \times 4'$ area. We show total RC flux density at the native resolution (top left) and again with contours (top centre). The lowest contour highlights low-surface brightness emission at a level of $18.3 \mu\text{Jy beam}^{-1}$ —this is 2.5 times the rms after smoothing the native image by a factor of 2.5. The other contours are placed following $(2 + 2^n)\sigma_{\text{native}}$, where $n \geq 0$ and both the rms ($\sigma_{\text{native}} = 6.04 \mu\text{Jy beam}^{-1}$) and the resolution ($\text{FWHM}_{\text{native}} = 2.6 \times 2.4$ arcsec) are taken from the native resolution image. These same contours are also superposed on ancillary LITTLE THINGS images where possible: $\text{H}\alpha$ (middle left); RC_{NTh} inferred from Deeg et al. 1997 (middle centre); *GALEX* FUV (middle right); *Spitzer* $24 \mu\text{m}$ (bottom left); *Spitzer* $70 \mu\text{m}$ (bottom centre); FUV+ $24 \mu\text{m}$ —inferred SFRD from Leroy et al. 2012 (bottom right). We also show the RC that was isolated by the RC-based masking technique (top right). The greyscale intensity scales used are arbitrary to best highlight structure.

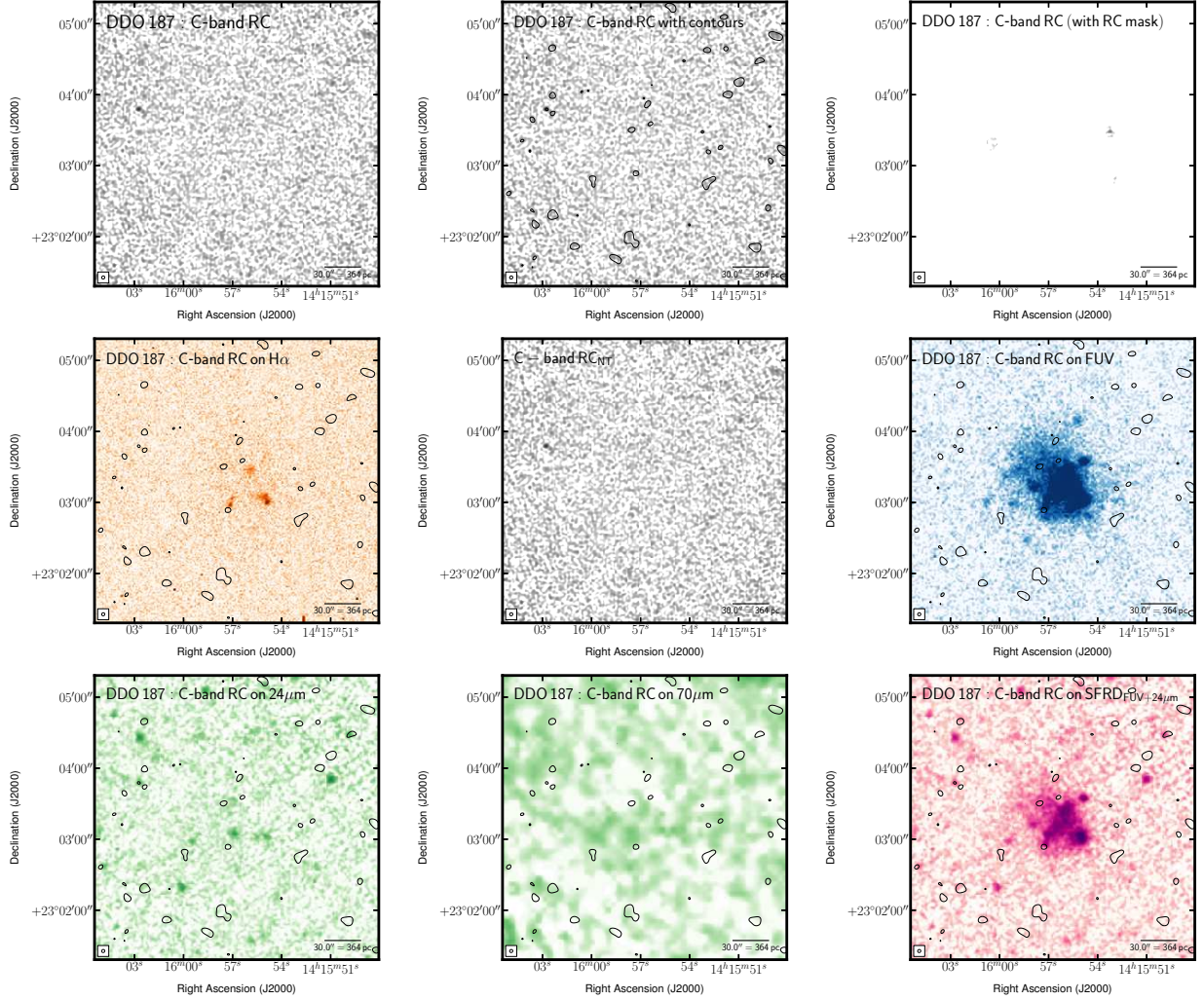


Fig. 32.— Multi-wavelength coverage of DDO 187 displaying a $4' \times 4'$ area. We show total RC flux density at the native resolution (top left) and again with contours (top centre). The lowest contour highlights low-surface brightness emission at a level of $26.2 \mu\text{Jy beam}^{-1}$ —this is 2.5 times the rms after smoothing the native image by a factor of 2.5. The other contours are placed following $(2 + 2^n)\sigma_{\text{native}}$, where $n \geq 0$ and both the rms ($\sigma_{\text{native}} = 6.90 \mu\text{Jy beam}^{-1}$) and the resolution ($\text{FWHM}_{\text{native}} = 2.7 \times 2.5$ arcsec) are taken from the native resolution image. These same contours are also superposed on ancillary LITTLE THINGS images where possible: $\text{H}\alpha$ (middle left); RC_{NTh} inferred from Deeg et al. 1997 (middle centre); *GALEX* FUV (middle right); *Spitzer* $24 \mu\text{m}$ (bottom left); *Spitzer* $70 \mu\text{m}$ (bottom centre); FUV+ $24 \mu\text{m}$ —inferred SFRD from Leroy et al. 2012 (bottom right). We also show the RC that was isolated by the RC-based masking technique (top right). The greyscale intensity scales used are arbitrary to best highlight structure.

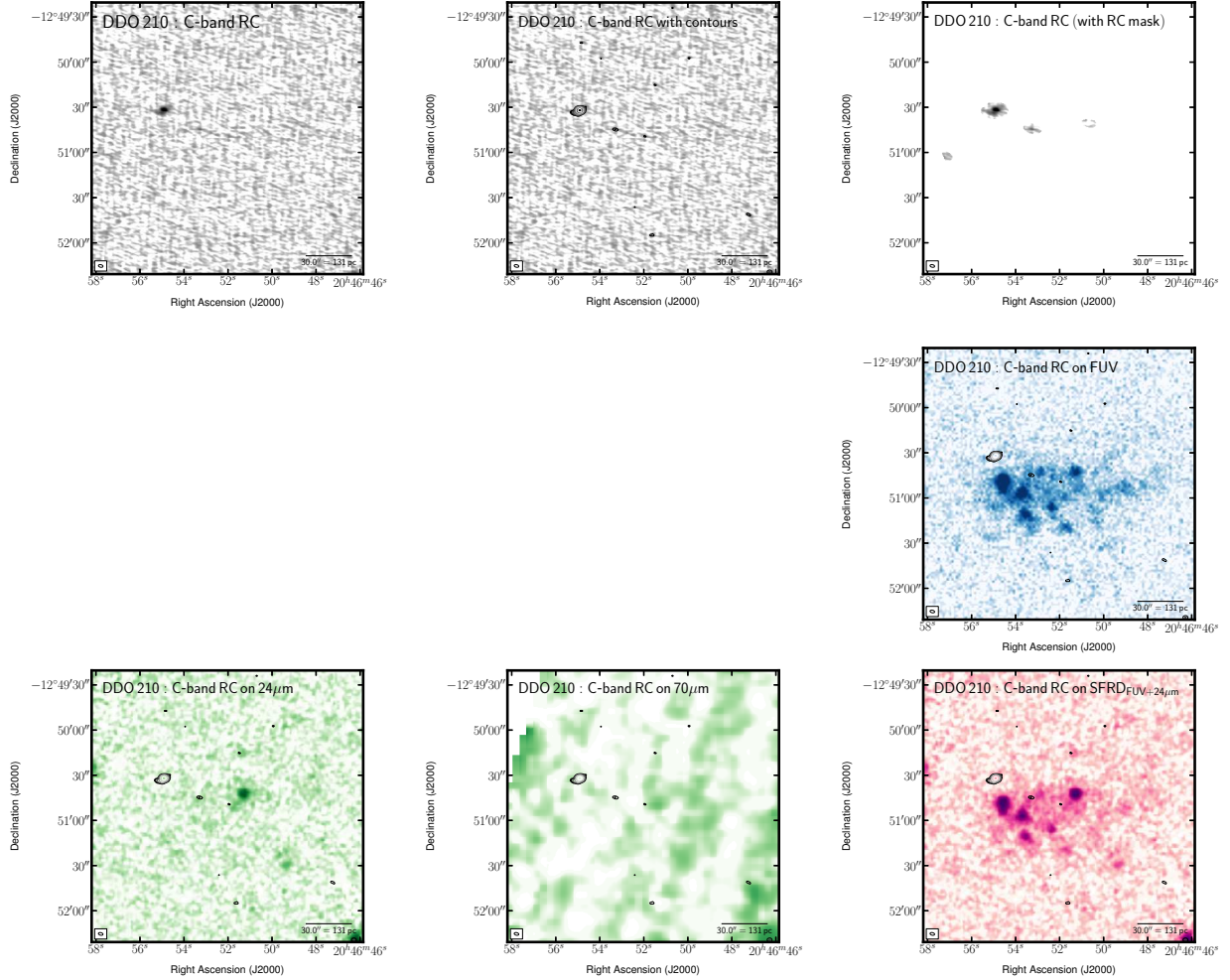


Fig. 33.— Multi-wavelength coverage of DDO 210 displaying a $2' \times 2'$ area. We show total RC flux density at the native resolution (top left) and again with contours (top centre). The lowest contour highlights low-surface brightness emission at a level of $39.3 \mu\text{Jy beam}^{-1}$ —this is 2.5 times the rms after smoothing the native image by a factor of 2.5. The other contours are placed following $(2 + 2^n)\sigma_{\text{native}}$, where $n \geq 0$ and both the rms ($\sigma_{\text{native}} = 4.65 \mu\text{Jy beam}^{-1}$) and the resolution ($\text{FWHM}_{\text{native}} = 3.1 \times 1.7$ arcsec) are taken from the native resolution image. These same contours are also superposed on ancillary LITTLE THINGS images where possible: *GALEX* FUV (middle right); *Spitzer* $24 \mu\text{m}$ (bottom left); *Spitzer* $70 \mu\text{m}$ (bottom centre); FUV+ $24 \mu\text{m}$ -inferred SFRD from Leroy et al. 2012 (bottom right). We also show the RC that was isolated by the RC-based masking technique (top right). The greyscale intensity scales used are arbitrary to best highlight structure.

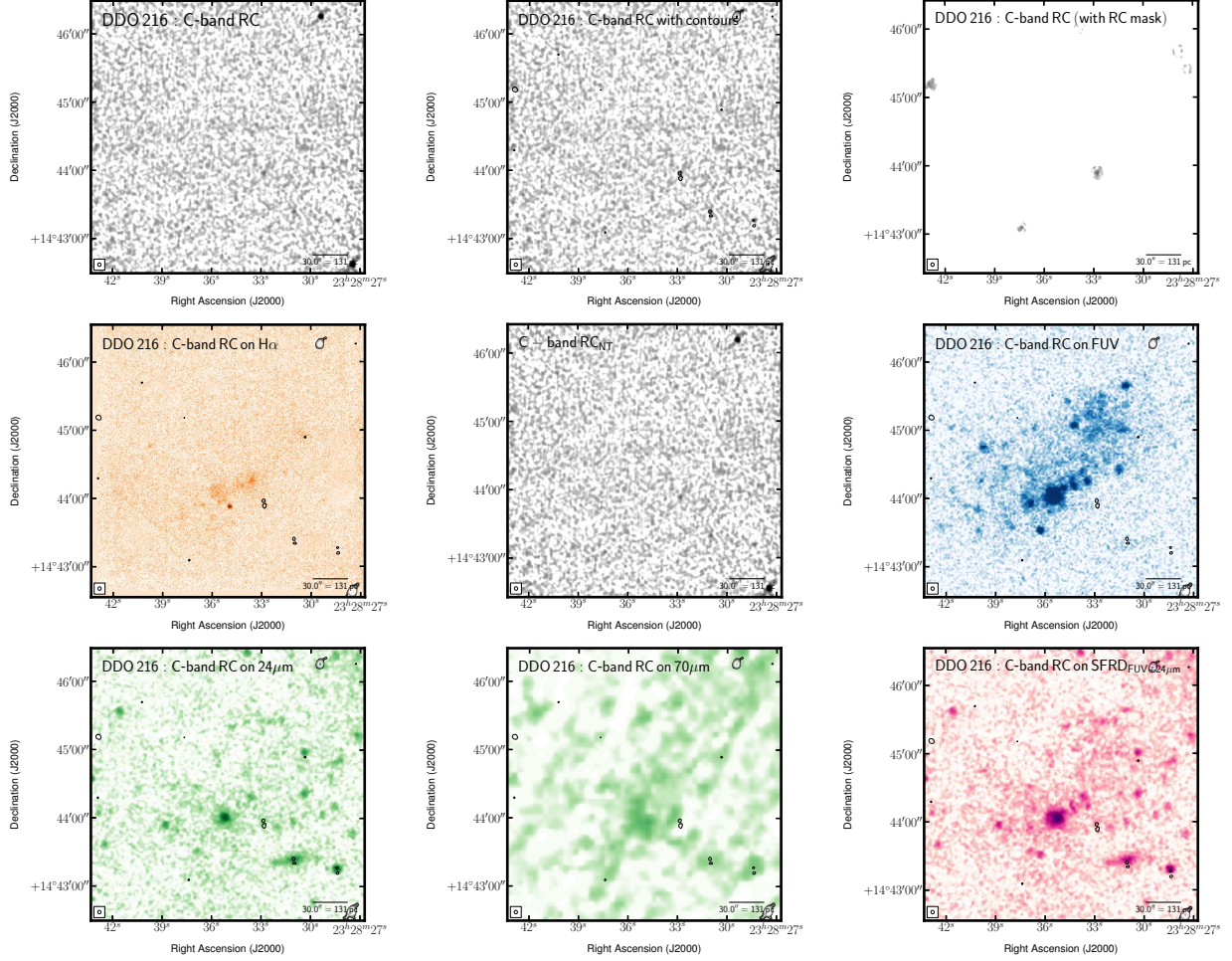


Fig. 34.— Multi-wavelength coverage of DDO 216 displaying a $-3' \times -3'$ area. We show total RC flux density at the native resolution (top left) and again with contours (top centre). The lowest contour highlights low-surface brightness emission at a level of $31.5 \mu\text{Jy beam}^{-1}$ —this is 2.5 times the rms after smoothing the native image by a factor of 2.5. The other contours are placed following $(2 + 2^n)\sigma_{\text{native}}$, where $n \geq 0$ and both the rms ($\sigma_{\text{native}} = 5.10 \mu\text{Jy beam}^{-1}$) and the resolution ($\text{FWHM}_{\text{native}} = 3.1 \times 2.9$ arcsec) are taken from the native resolution image. These same contours are also superposed on ancillary LITTLE THINGS images where possible: $\text{H}\alpha$ (middle left); RC_{NTTh} inferred from Deeg et al. 1997 (middle centre); *GALEX* FUV (middle right); *Spitzer* $24 \mu\text{m}$ (bottom left); *Spitzer* $70 \mu\text{m}$ (bottom centre); FUV+ $24 \mu\text{m}$ -inferred SFRD from Leroy et al. 2012 (bottom right). We also show the RC that was isolated by the RC-based masking technique (top right). The greyscale intensity scales used are arbitrary to best highlight structure.

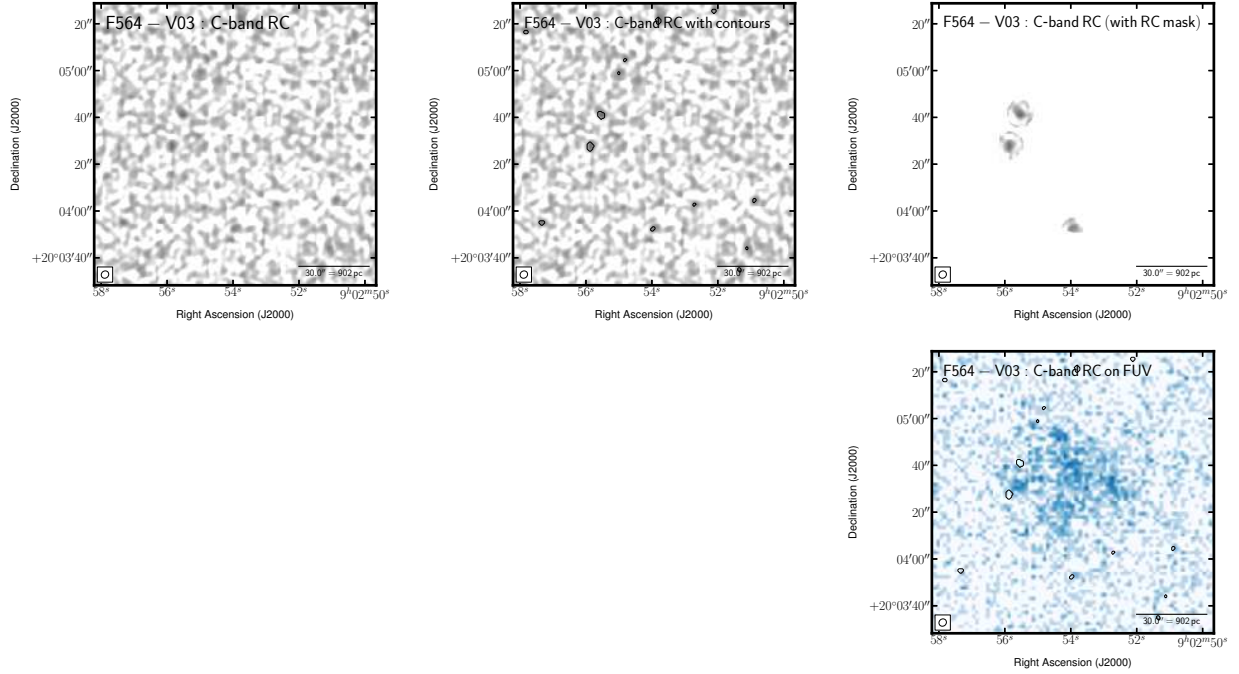


Fig. 35.— Multi-wavelength coverage of F564-V03 displaying a $2' \times 2'$ area. We show total RC flux density at the native resolution (top left) and again with contours (top centre). The lowest contour highlights low-surface brightness emission at a level of $45.2 \mu\text{Jy beam}^{-1}$ —this is 2.5 times the rms after smoothing the native image by a factor of 2.5. The other contours are placed following $(2 + 2^n)\sigma_{\text{native}}$, where $n \geq 0$ and both the rms ($\sigma_{\text{native}} = 5.44 \mu\text{Jy beam}^{-1}$) and the resolution ($\text{FWHM}_{\text{native}} = 3.3 \times 3.0$ arcsec) are taken from the native resolution image. These same contours are also superposed on ancillary LITTLE THINGS images where possible: *GALEX* FUV (middle right). We also show the RC that was isolated by the RC-based masking technique (top right). The greyscale intensity scales used are arbitrary to best highlight structure.

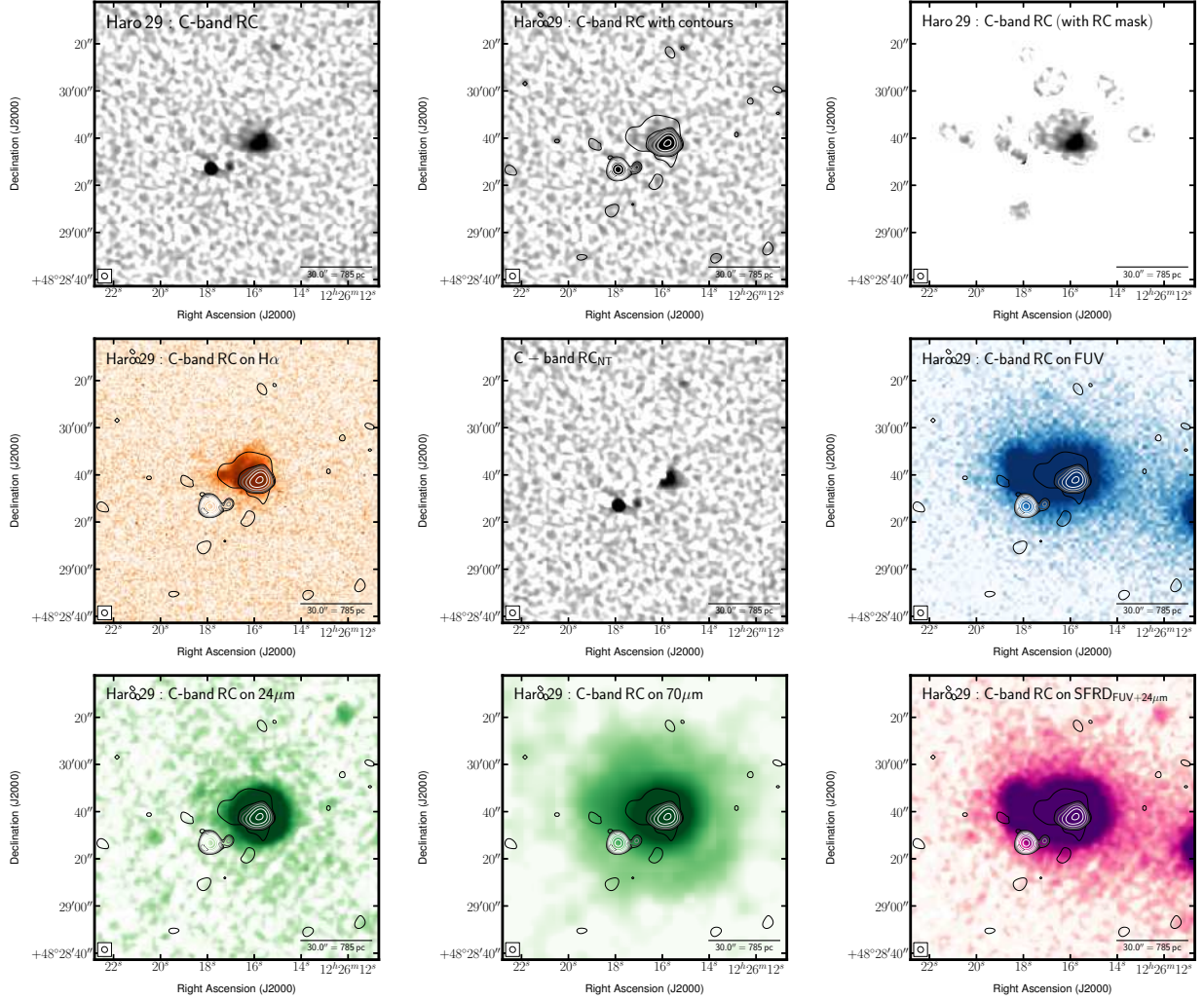


Fig. 36.— Multi-wavelength coverage of Haro 29 displaying a $2' \times 2'$ area. We show total RC flux density at the native resolution (top left) and again with contours (top centre). The lowest contour highlights low-surface brightness emission at a level of $19.1 \mu\text{Jy beam}^{-1}$ —this is 2.5 times the rms after smoothing the native image by a factor of 2.5. The other contours are placed following $(2 + 2^n)\sigma_{\text{native}}$, where $n \geq 0$ and both the rms ($\sigma_{\text{native}} = 6.13 \mu\text{Jy beam}^{-1}$) and the resolution ($\text{FWHM}_{\text{native}} = 2.6 \times 2.4$ arcsec) are taken from the native resolution image. These same contours are also superposed on ancillary LITTLE THINGS images where possible: $\text{H}\alpha$ (middle left); RC_{NT} inferred from Deeg et al. 1997 (middle centre); *GALEX* FUV (middle right); *Spitzer* $24 \mu\text{m}$ (bottom left); *Spitzer* $70 \mu\text{m}$ (bottom centre); FUV+ $24 \mu\text{m}$ —inferred SFRD from Leroy et al. 2012 (bottom right). We also show the RC that was isolated by the RC-based masking technique (top right). The greyscale intensity scales used are arbitrary to best highlight structure.

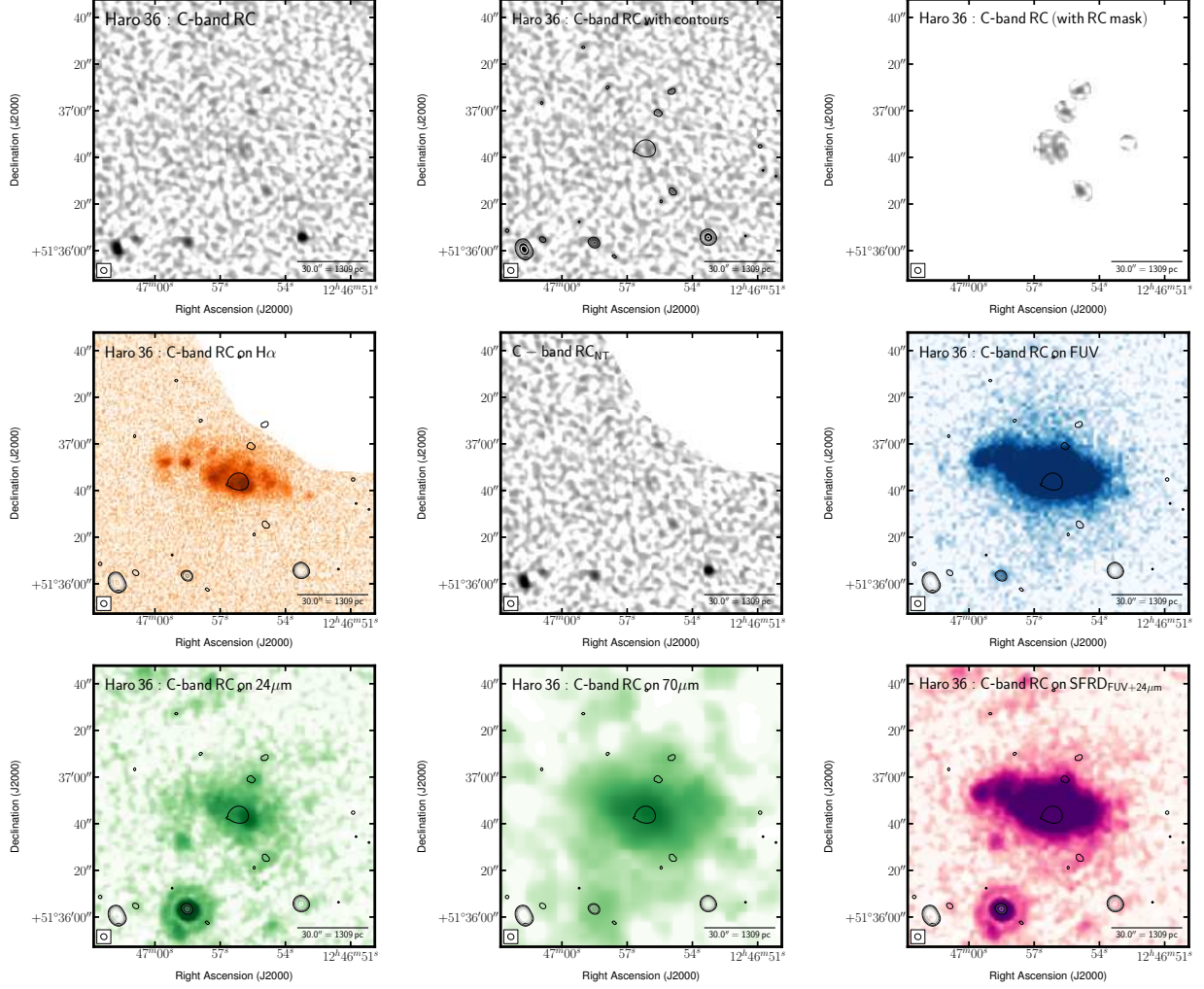


Fig. 37.— Multi-wavelength coverage of Haro 36 displaying a $2' \times 2'$ area. We show total RC flux density at the native resolution (top left) and again with contours (top centre). The lowest contour highlights low-surface brightness emission at a level of $38.2 \mu\text{Jy beam}^{-1}$ —this is 2.5 times the rms after smoothing the native image by a factor of 2.5. The other contours are placed following $(2 + 2^n)\sigma_{\text{native}}$, where $n \geq 0$ and both the rms ($\sigma_{\text{native}} = 6.68 \mu\text{Jy beam}^{-1}$) and the resolution ($\text{FWHM}_{\text{native}} = 2.7 \times 2.5$ arcsec) are taken from the native resolution image. These same contours are also superposed on ancillary LITTLE THINGS images where possible: $\text{H}\alpha$ (middle left); RC_{NT} inferred from Deeg et al. 1997 (middle centre); *GALEX* FUV (middle right); *Spitzer* $24 \mu\text{m}$ (bottom left); *Spitzer* $70 \mu\text{m}$ (bottom centre); FUV+ $24 \mu\text{m}$ –inferred SFRD from Leroy et al. 2012 (bottom right). We also show the RC that was isolated by the RC–based masking technique (top right). The greyscale intensity scales used are arbitrary to best highlight structure.

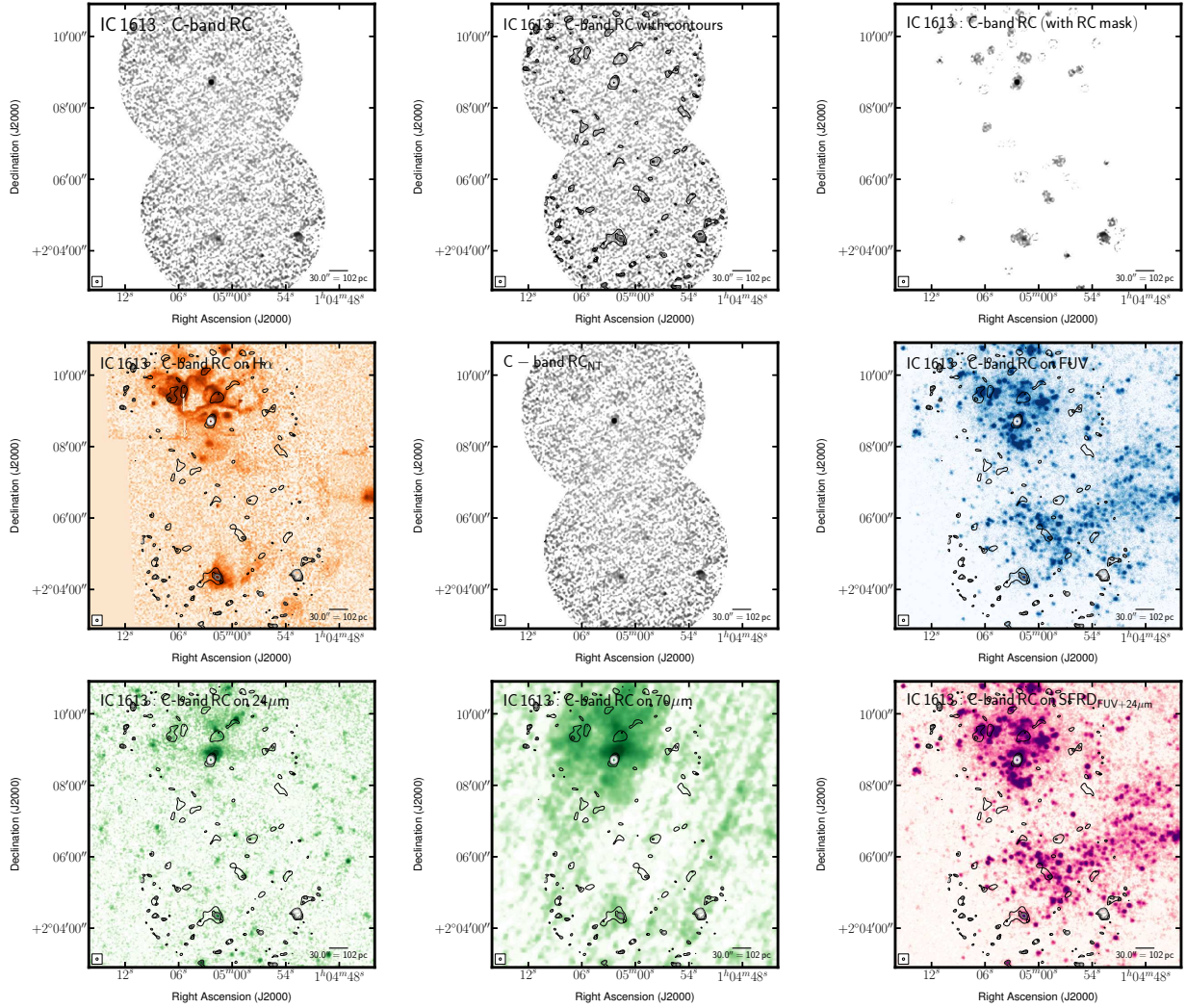


Fig. 38.— Multi-wavelength coverage of IC 1613 displaying a $12' \times 12'$ area. We show total RC flux density at the native resolution (top left) and again with contours (top centre). The lowest contour highlights low-surface brightness emission at a level of $20.7 \mu\text{Jy beam}^{-1}$ —this is 2.5 times the rms after smoothing the native image by a factor of 2.5. The other contours are placed following $(2 + 2^n)\sigma_{\text{native}}$, where $n \geq 0$ and both the rms ($\sigma_{\text{native}} = 6.12 \mu\text{Jy beam}^{-1}$) and the resolution ($\text{FWHM}_{\text{native}} = 3.9 \times 3.7 \text{ arcsec}$) are taken from the native resolution image. These same contours are also superposed on ancillary LITTLE THINGS images where possible: $\text{H}\alpha$ (middle left); RC_{NT} inferred from Deeg et al. 1997 (middle centre); *GALEX* FUV (middle right); *Spitzer* $24 \mu\text{m}$ (bottom left); *Spitzer* $70 \mu\text{m}$ (bottom centre); FUV+ $24 \mu\text{m}$ —inferred SFRD from Leroy et al. 2012 (bottom right). We also show the RC that was isolated by the RC-based masking technique (top right). The greyscale intensity scales used are arbitrary to best highlight structure.

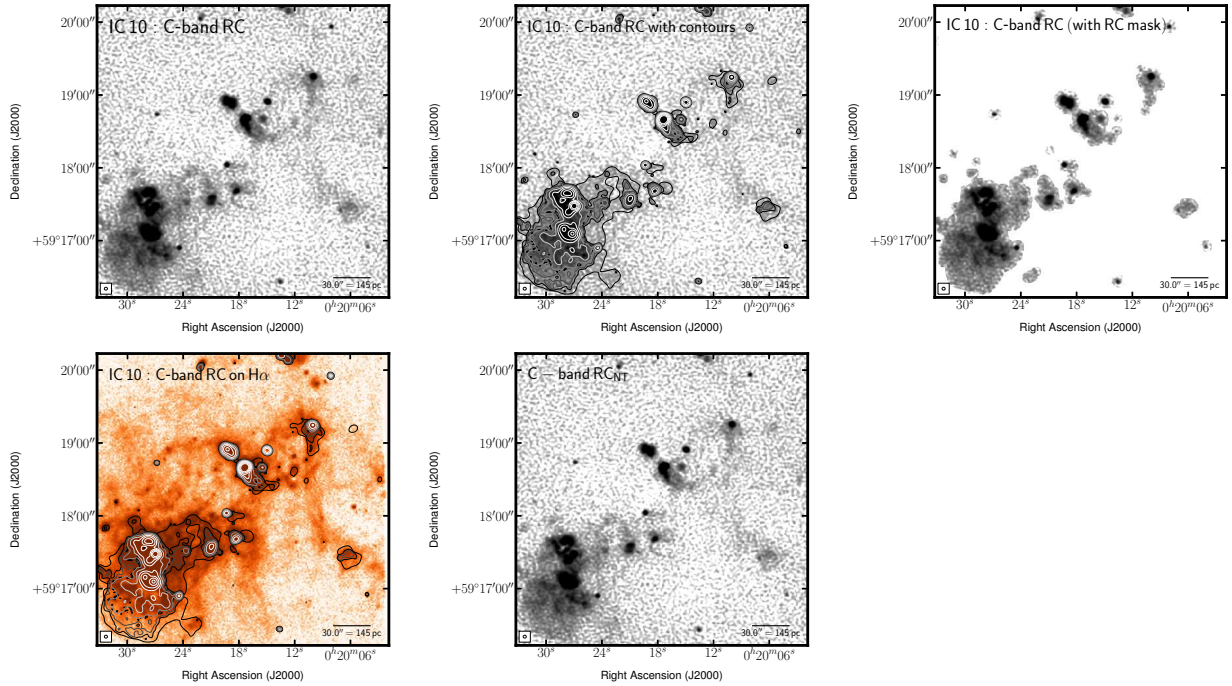


Fig. 39.— Multi-wavelength coverage of IC 10 displaying a $4' \times 4'$ area. We show total RC flux density at the native resolution (top left) and again with contours (top centre). The lowest contour highlights low-surface brightness emission at a level of $66.6 \mu\text{Jy beam}^{-1}$ —this is 2.5 times the rms after smoothing the native image by a factor of 2.5. The other contours are placed following $(2 + 2^n)\sigma_{\text{native}}$, where $n \geq 0$ and both the rms ($\sigma_{\text{native}} = 7.84 \mu\text{Jy beam}^{-1}$) and the resolution ($\text{FWHM}_{\text{native}} = 2.6 \times 2.3 \text{ arcsec}$) are taken from the native resolution image. These same contours are also superposed on ancillary LITTLE THINGS images where possible: $\text{H}\alpha$ (middle left); RC_{NT} inferred from Deeg et al. 1997 (middle centre). We also show the RC that was isolated by the RC-based masking technique (top right). The greyscale intensity scales used are arbitrary to best highlight structure.

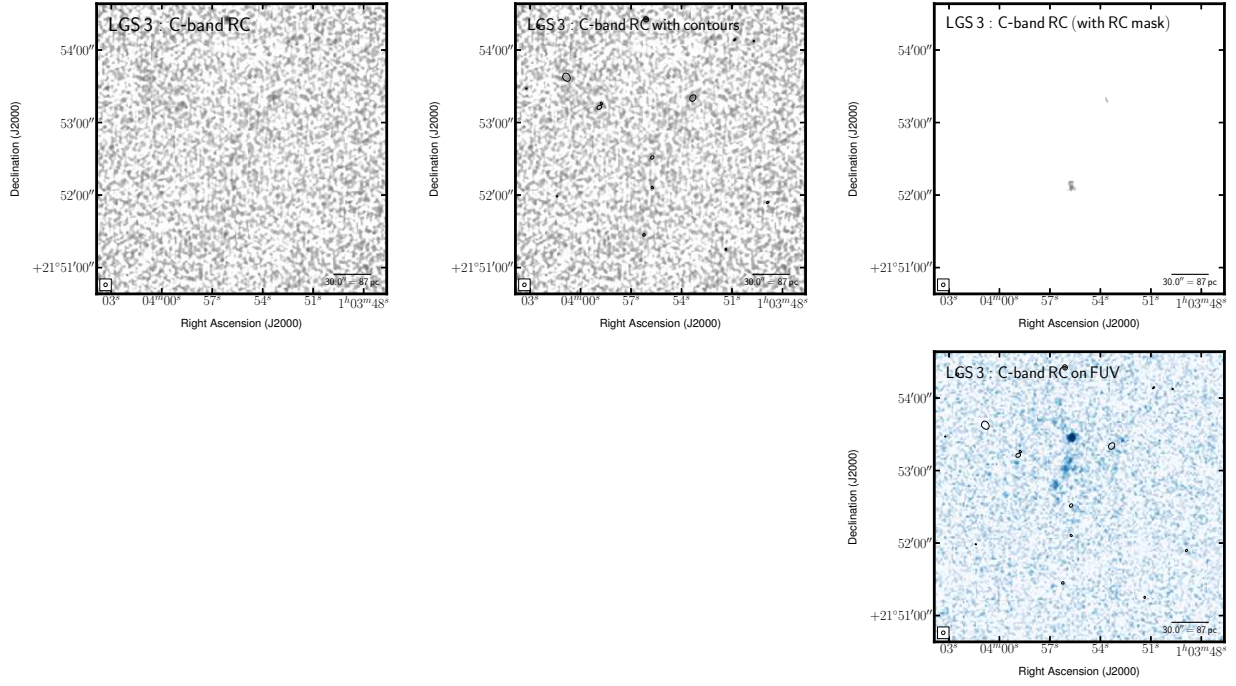


Fig. 40.— Multi-wavelength coverage of LGS 3 displaying a $4' \times 4'$ area. We show total RC flux density at the native resolution (top left) and again with contours (top centre). The lowest contour highlights low-surface brightness emission at a level of $33.4 \mu\text{Jy beam}^{-1}$ —this is 2.5 times the rms after smoothing the native image by a factor of 2.5. The other contours are placed following $(2 + 2^n)\sigma_{\text{native}}$, where $n \geq 0$ and both the rms ($\sigma_{\text{native}} = 5.54 \mu\text{Jy beam}^{-1}$) and the resolution ($\text{FWHM}_{\text{native}} = 3.0 \times 2.8 \text{ arcsec}$) are taken from the native resolution image. These same contours are also superposed on ancillary LITTLE THINGS images where possible: *GALEX* FUV (middle right). We also show the RC that was isolated by the RC-based masking technique (top right). The greyscale intensity scales used are arbitrary to best highlight structure.

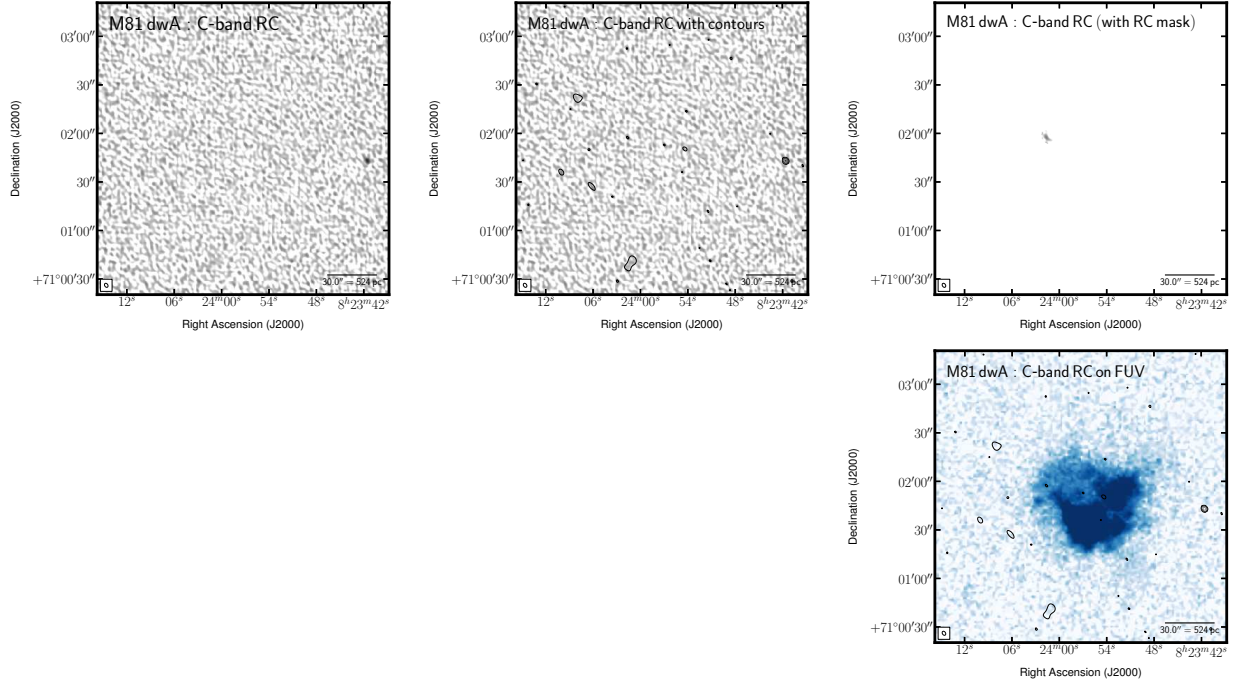


Fig. 41.— Multi-wavelength coverage of M81 dwA displaying a $3' \times 3'$ area. We show total RC flux density at the native resolution (top left) and again with contours (top centre). The lowest contour highlights low-surface brightness emission at a level of $39.2 \mu\text{Jy beam}^{-1}$ —this is 2.5 times the rms after smoothing the native image by a factor of 2.5. The other contours are placed following $(2+2^n)\sigma_{\text{native}}$, where $n \geq 0$ and both the rms ($\sigma_{\text{native}} = 10.77 \mu\text{Jy beam}^{-1}$) and the resolution ($\text{FWHM}_{\text{native}} = 2.7 \times 1.9 \text{ arcsec}$) are taken from the native resolution image. These same contours are also superposed on ancillary LITTLE THINGS images where possible: *GALEX* FUV (middle right). We also show the RC that was isolated by the RC-based masking technique (top right). The greyscale intensity scales used are arbitrary to best highlight structure.

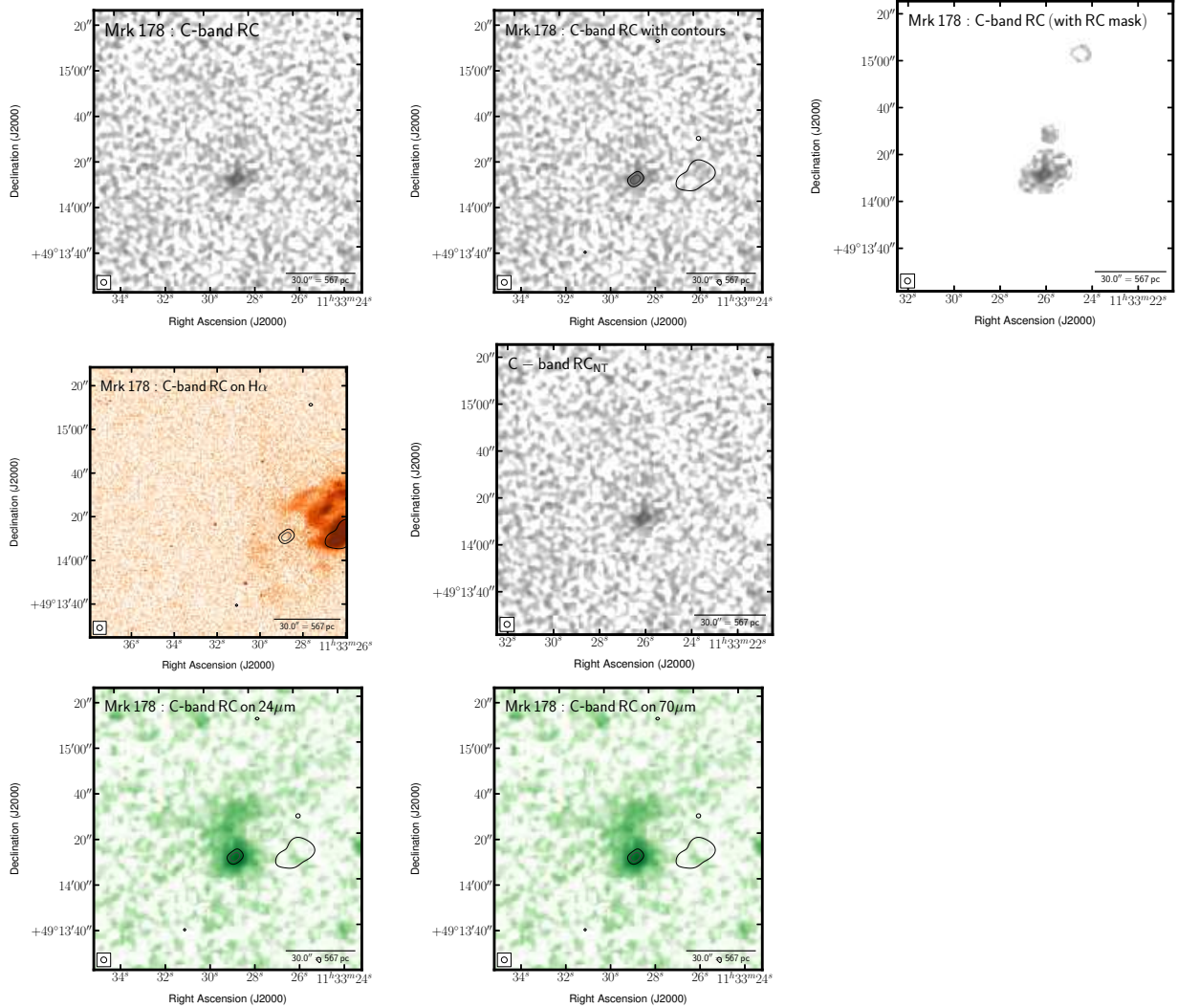


Fig. 42.— Multi-wavelength coverage of Mrk 178 displaying a $37' \times 37'$ area. We show total RC flux density at the native resolution (top left) and again with contours (top centre). The lowest contour highlights low-surface brightness emission at a level of $36.9 \mu\text{Jy beam}^{-1}$ —this is 2.5 times the rms after smoothing the native image by a factor of 2.5. The other contours are placed following $(2 + 2^n)\sigma_{\text{native}}$, where $n \geq 0$ and both the rms ($\sigma_{\text{native}} = 6.49 \mu\text{Jy beam}^{-1}$) and the resolution ($\text{FWHM}_{\text{native}} = 2.6 \times 2.5$ arcsec) are taken from the native resolution image. These same contours are also superposed on ancillary LITTLE THINGS images where possible: $\text{H}\alpha$ (middle left); $\text{RC}_{\text{NT}}^{\text{Th}}$ inferred from Deeg et al. 1997 (middle centre); *Spitzer* $24 \mu\text{m}$ (bottom left); *Spitzer* $70 \mu\text{m}$ (bottom centre). We also show the RC that was isolated by the RC-based masking technique (top right). The greyscale intensity scales used are arbitrary to best highlight structure.

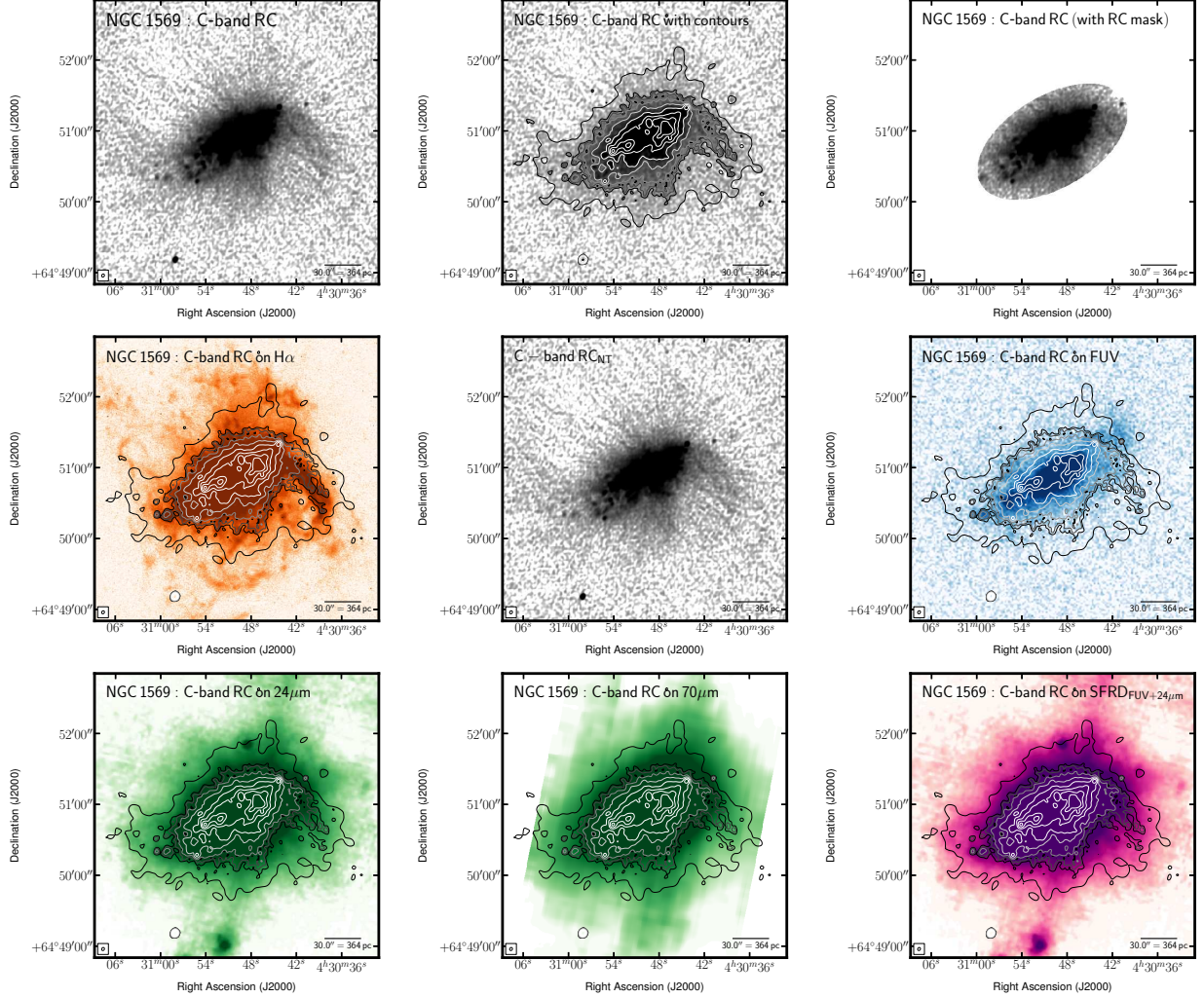


Fig. 43.— Multi-wavelength coverage of NGC 1569 displaying a $1' \times 1'$ area. We show total RC flux density at the native resolution (top left) and again with contours (top centre). The lowest contour highlights low-surface brightness emission at a level of $42.2 \mu\text{Jy beam}^{-1}$ —this is 2.5 times the rms after smoothing the native image by a factor of 2.5. The other contours are placed following $(2 + 2^n)\sigma_{\text{native}}$, where $n \geq 0$ and both the rms ($\sigma_{\text{native}} = 6.77 \mu\text{Jy beam}^{-1}$) and the resolution ($\text{FWHM}_{\text{native}} = 2.7 \times 2.3$ arcsec) are taken from the native resolution image. These same contours are also superposed on ancillary LITTLE THINGS images where possible: $\text{H}\alpha$ (middle left); RC_{NT} inferred from Deeg et al. 1997 (middle centre); *GALEX* FUV (middle right); *Spitzer* $24 \mu\text{m}$ (bottom left); *Spitzer* $70 \mu\text{m}$ (bottom centre); FUV+ $24 \mu\text{m}$ -inferred SFRD from Leroy et al. 2012 (bottom right). We also show the RC that was isolated by the RC-based masking technique (top right). The greyscale intensity scales used are arbitrary to best highlight structure.

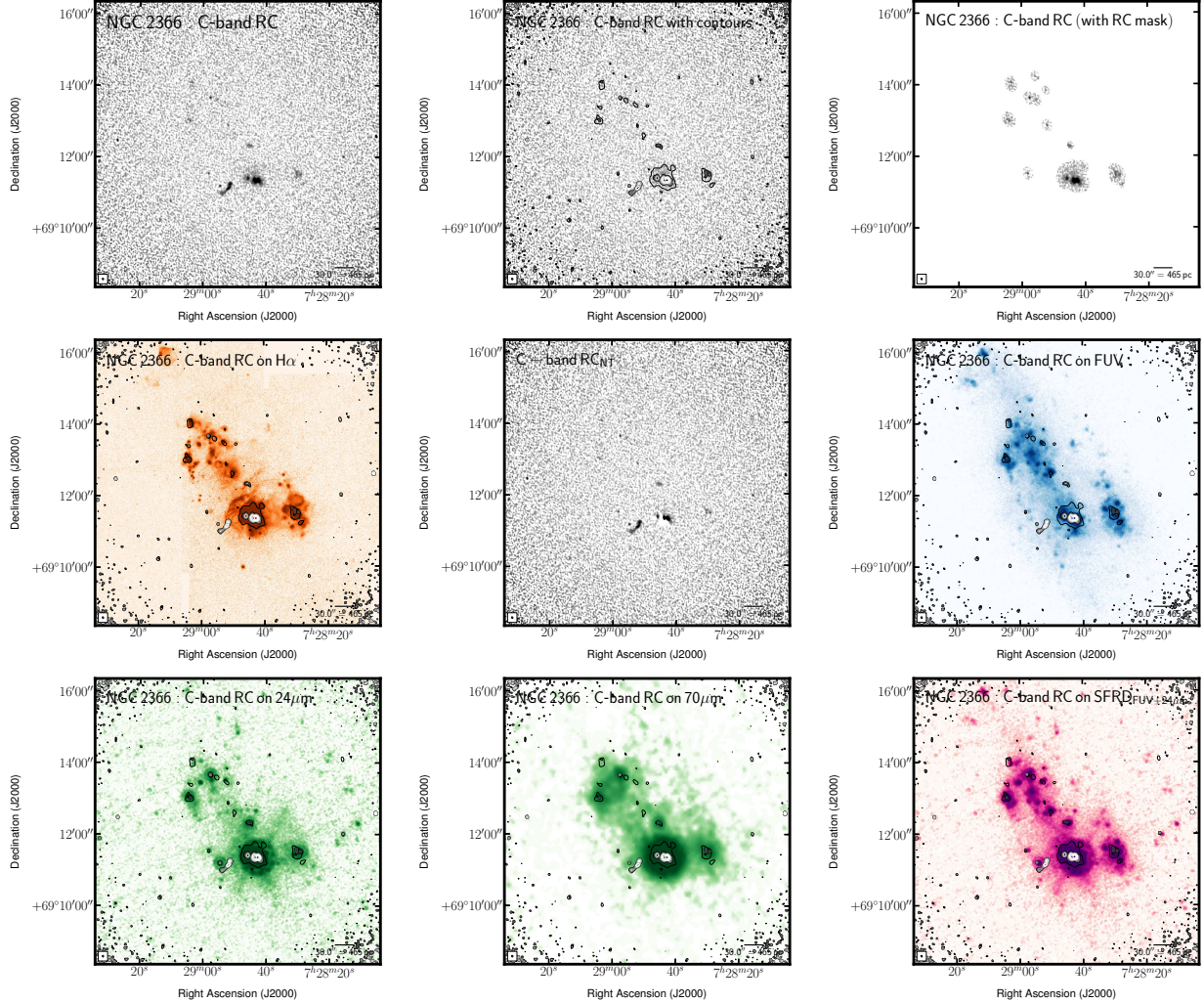


Fig. 44.— Multi-wavelength coverage of NGC 2366 displaying a $7' \times 7'$ area. We show total RC flux density at the native resolution (top left) and again with contours (top centre). The lowest contour highlights low-surface brightness emission at a level of $26.5 \mu\text{Jy beam}^{-1}$ —this is 2.5 times the rms after smoothing the native image by a factor of 2.5. The other contours are placed following $(2 + 2^n)\sigma_{\text{native}}$, where $n \geq 0$ and both the rms ($\sigma_{\text{native}} = 6.46 \mu\text{Jy beam}^{-1}$) and the resolution ($\text{FWHM}_{\text{native}} = 2.9 \times 2.3$ arcsec) are taken from the native resolution image. These same contours are also superposed on ancillary LITTLE THINGS images where possible: $\text{H}\alpha$ (middle left); RC_{NTh} inferred from Deeg et al. 1997 (middle centre); *GALEX* FUV (middle right); *Spitzer* $24 \mu\text{m}$ (bottom left); *Spitzer* $70 \mu\text{m}$ (bottom centre); FUV+ $24 \mu\text{m}$ -inferred SFRD from Leroy et al. 2012 (bottom right). We also show the RC that was isolated by the RC-based masking technique (top right). The greyscale intensity scales used are arbitrary to best highlight structure.

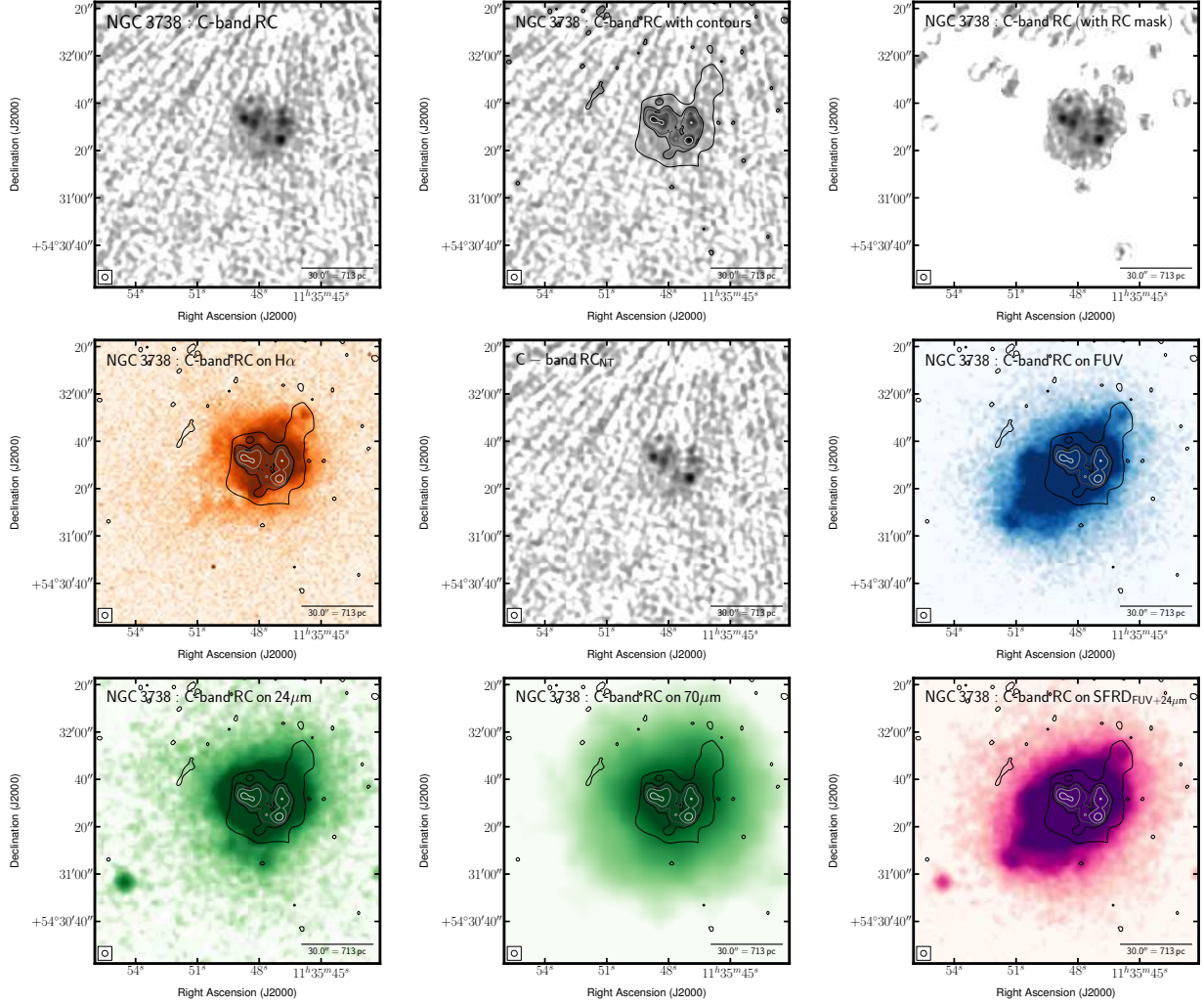


Fig. 45.— Multi-wavelength coverage of NGC 3738 displaying a $2' \times 2'$ area. We show total RC flux density at the native resolution (top left) and again with contours (top centre). The lowest contour highlights low-surface brightness emission at a level of $43.8 \mu\text{Jy beam}^{-1}$ —this is 2.5 times the rms after smoothing the native image by a factor of 2.5. The other contours are placed following $(2 + 2^n)\sigma_{\text{native}}$, where $n \geq 0$ and both the rms ($\sigma_{\text{native}} = 7.60 \mu\text{Jy beam}^{-1}$) and the resolution ($\text{FWHM}_{\text{native}} = 2.5 \times 2.5$ arcsec) are taken from the native resolution image. These same contours are also superposed on ancillary LITTLE THINGS images where possible: $\text{H}\alpha$ (middle left); RC_{NTh} inferred from Deeg et al. 1997 (middle centre); *GALEX* FUV (middle right); *Spitzer* $24 \mu\text{m}$ (bottom left); *Spitzer* $70 \mu\text{m}$ (bottom centre); FUV+ $24 \mu\text{m}$ —inferred SFRD from Leroy et al. 2012 (bottom right). We also show the RC that was isolated by the RC-based masking technique (top right). The greyscale intensity scales used are arbitrary to best highlight structure.

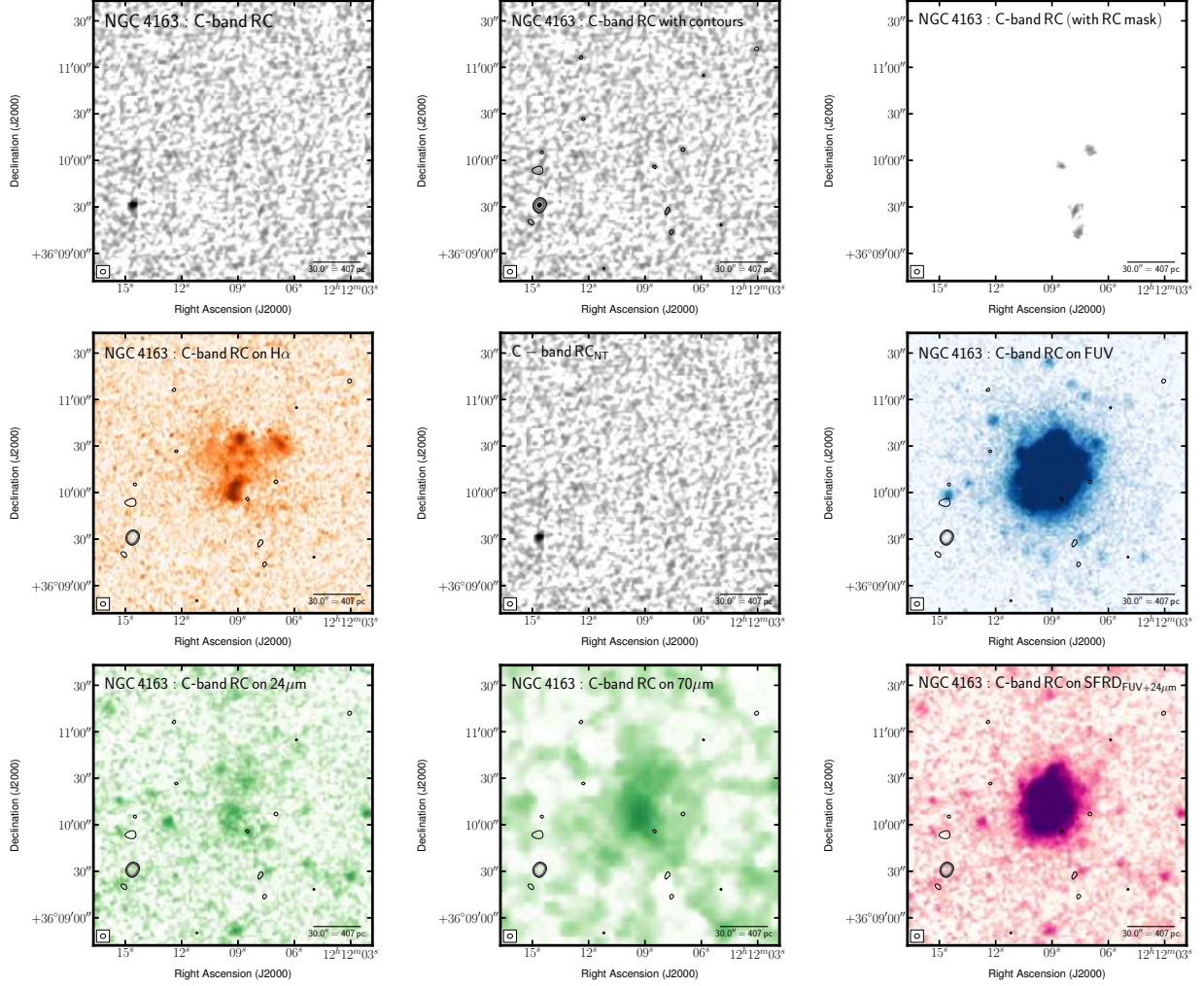


Fig. 46.— Multi-wavelength coverage of NGC 4163 displaying a $3' \times 3'$ area. We show total RC flux density at the native resolution (top left) and again with contours (top centre). The lowest contour highlights low-surface brightness emission at a level of $25.4 \mu\text{Jy beam}^{-1}$ —this is 2.5 times the rms after smoothing the native image by a factor of 2.5. The other contours are placed following $(2 + 2^n)\sigma_{\text{native}}$, where $n \geq 0$ and both the rms ($\sigma_{\text{native}} = 4.53 \mu\text{Jy beam}^{-1}$) and the resolution ($\text{FWHM}_{\text{native}} = 3.3 \times 2.9$ arcsec) are taken from the native resolution image. These same contours are also superposed on ancillary LITTLE THINGS images where possible: $\text{H}\alpha$ (middle left); $\text{RC}_{\text{NT}}^{\text{Th}}$ inferred from Deeg et al. 1997 (middle centre); *GALEX* FUV (middle right); *Spitzer* $24 \mu\text{m}$ (bottom left); *Spitzer* $70 \mu\text{m}$ (bottom centre); FUV+ $24 \mu\text{m}$ -inferred SFRD from Leroy et al. 2012 (bottom right). We also show the RC that was isolated by the RC-based masking technique (top right). The greyscale intensity scales used are arbitrary to best highlight structure.

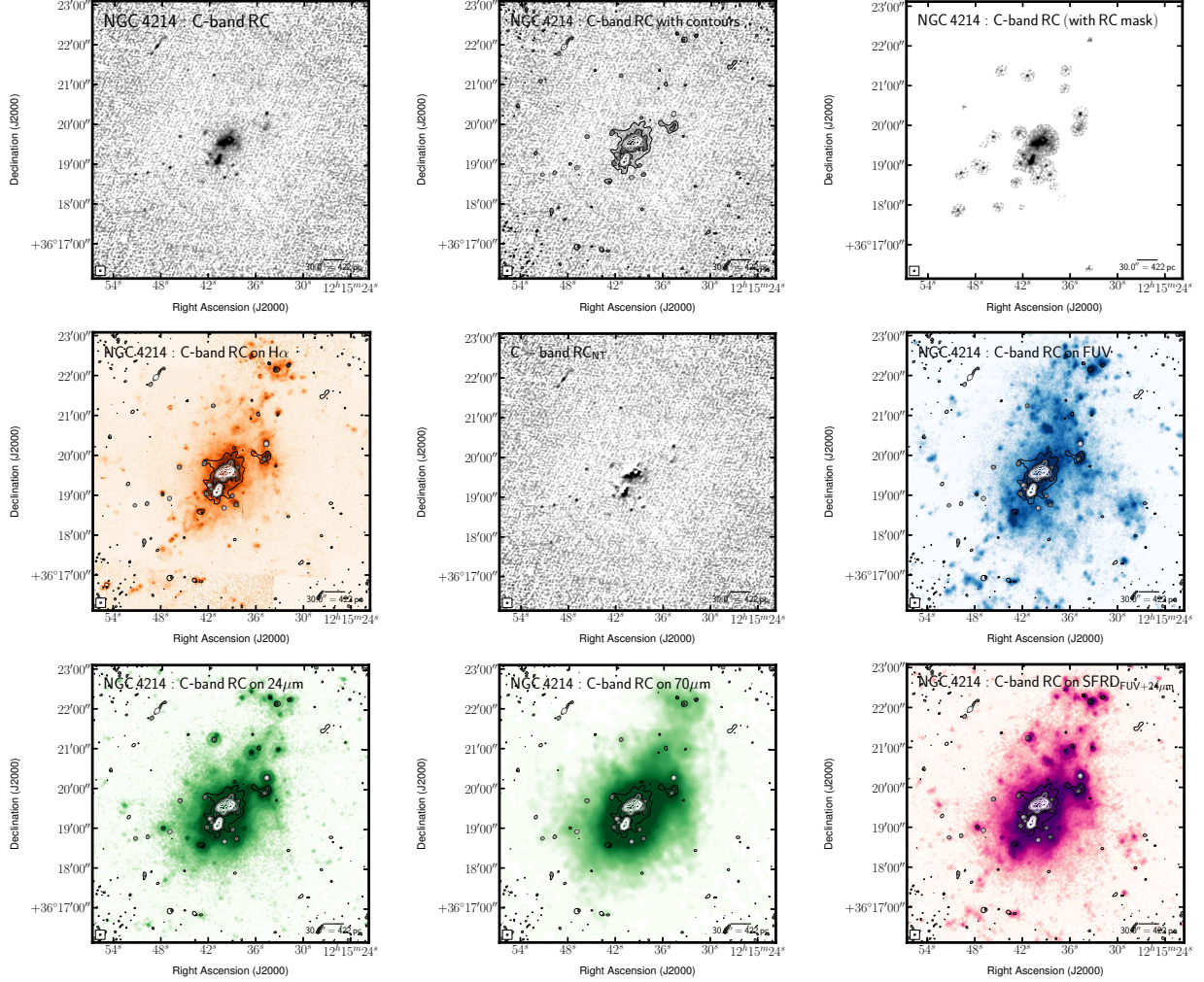


Fig. 47.— Multi-wavelength coverage of NGC 4214 displaying a $7' \times 7'$ area. We show total RC flux density at the native resolution (top left) and again with contours (top centre). The lowest contour highlights low-surface brightness emission at a level of $38.4 \mu\text{Jy beam}^{-1}$ —this is 2.5 times the rms after smoothing the native image by a factor of 2.5. The other contours are placed following $(2 + 2^n)\sigma_{\text{native}}$, where $n \geq 0$ and both the rms ($\sigma_{\text{native}} = 7.13 \mu\text{Jy beam}^{-1}$) and the resolution ($\text{FWHM}_{\text{native}} = 2.9 \times 2.4 \text{ arcsec}$) are taken from the native resolution image. These same contours are also superposed on ancillary LITTLE THINGS images where possible: $\text{H}\alpha$ (middle left); RC_{NTh} inferred from Deeg et al. 1997 (middle centre); *GALEX* FUV (middle right); *Spitzer* $24 \mu\text{m}$ (bottom left); *Spitzer* $70 \mu\text{m}$ (bottom centre); FUV+ $24 \mu\text{m}$ -inferred SFRD from Leroy et al. 2012 (bottom right). We also show the RC that was isolated by the RC-based masking technique (top right). The greyscale intensity scales used are arbitrary to best highlight structure.

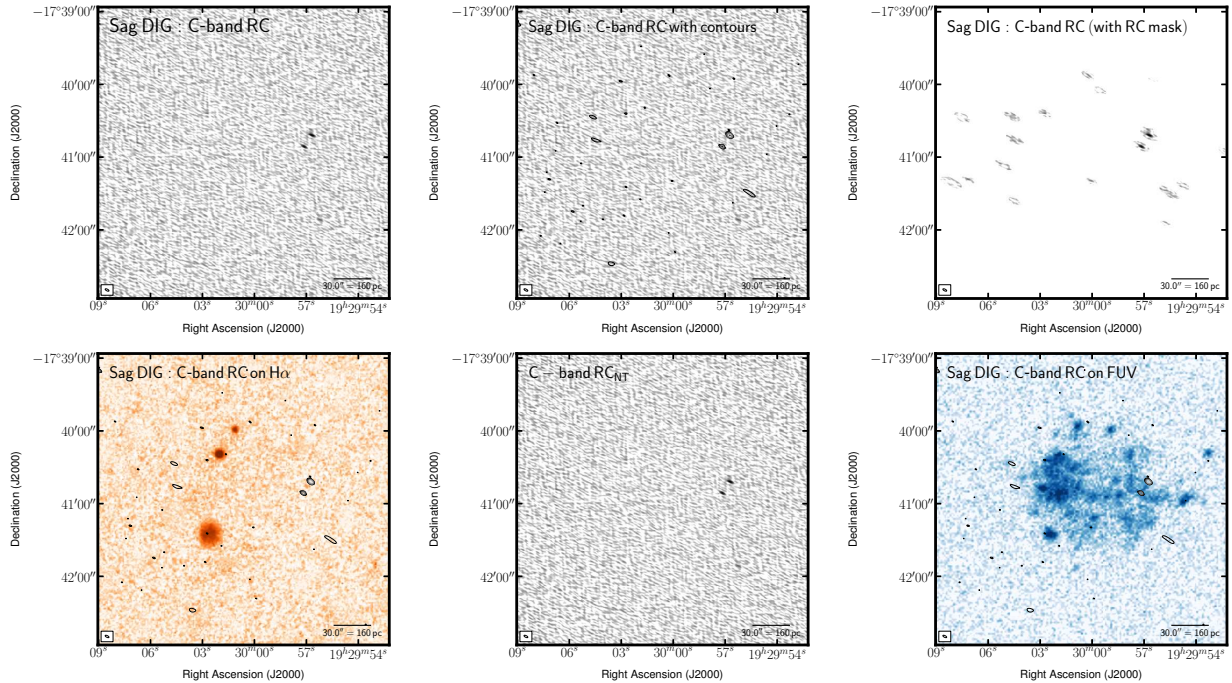


Fig. 48.— Multi-wavelength coverage of Sag DIG displaying a $4' \times 4'$ area. We show total RC flux density at the native resolution (top left) and again with contours (top centre). The lowest contour highlights low-surface brightness emission at a level of $27.9 \mu\text{Jy beam}^{-1}$ —this is 2.5 times the rms after smoothing the native image by a factor of 2.5. The other contours are placed following $(2 + 2^n)\sigma_{\text{native}}$, where $n \geq 0$ and both the rms ($\sigma_{\text{native}} = 8.23 \mu\text{Jy beam}^{-1}$) and the resolution ($\text{FWHM}_{\text{native}} = 3.5 \times 1.4 \text{ arcsec}$) are taken from the native resolution image. These same contours are also superposed on ancillary LITTLE THINGS images where possible: $\text{H}\alpha$ (middle left); RC_{NTh} inferred from Deeg et al. 1997 (middle centre); *GALEX* FUV (middle right). We also show the RC that was isolated by the RC-based masking technique (top right). The greyscale intensity scales used are arbitrary to best highlight structure.

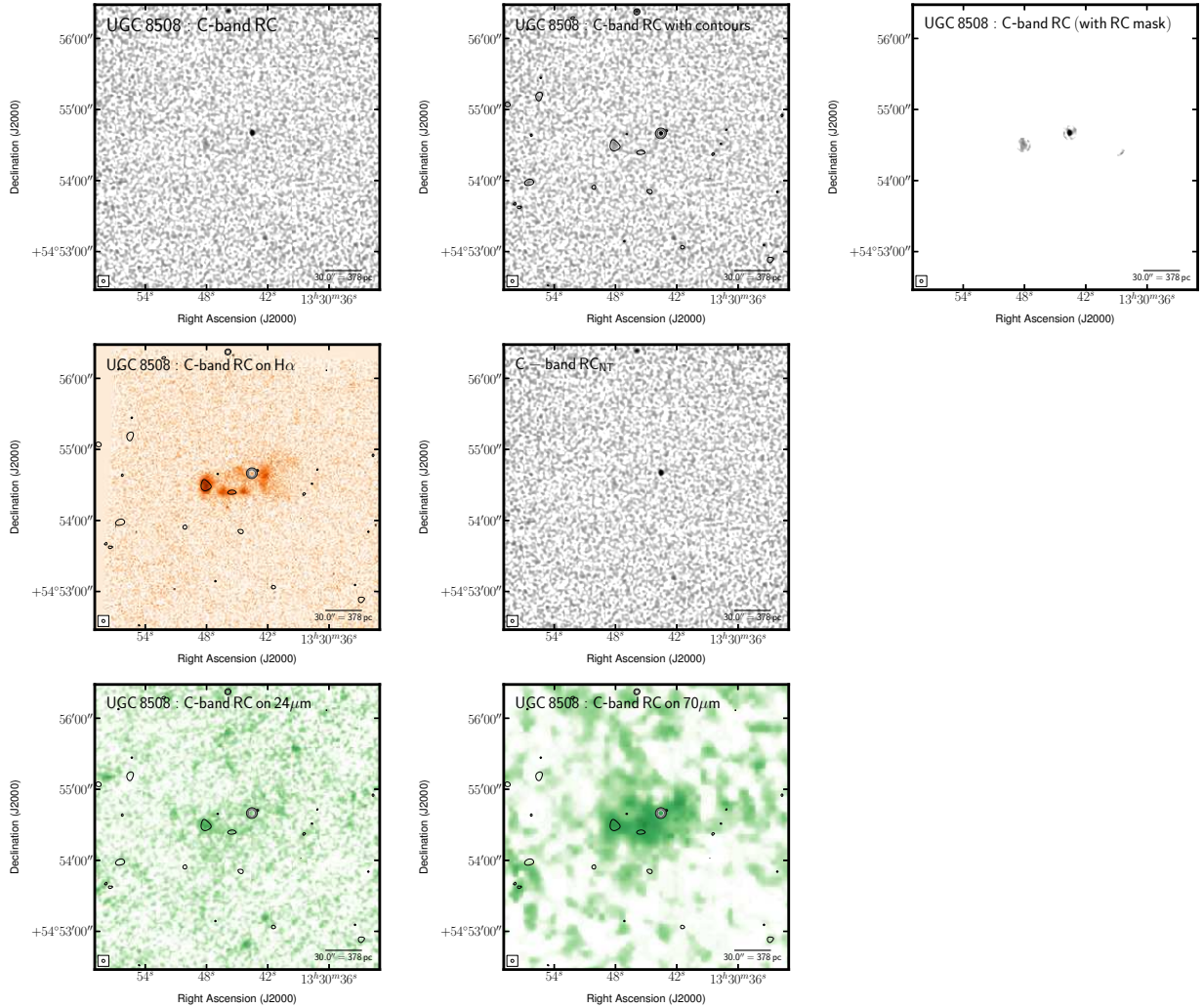


Fig. 49.— Multi-wavelength coverage of UGC 8508 displaying a $4' \times 4'$ area. We show total RC flux density at the native resolution (top left) and again with contours (top centre). The lowest contour highlights low-surface brightness emission at a level of $23.2 \mu\text{Jy beam}^{-1}$ —this is 2.5 times the rms after smoothing the native image by a factor of 2.5. The other contours are placed following $(2 + 2^n)\sigma_{\text{native}}$, where $n \geq 0$ and both the rms ($\sigma_{\text{native}} = 6.04 \mu\text{Jy beam}^{-1}$) and the resolution ($\text{FWHM}_{\text{native}} = 2.6 \times 2.5$ arcsec) are taken from the native resolution image. These same contours are also superposed on ancillary LITTLE THINGS images where possible: $\text{H}\alpha$ (middle left); RC_{NTh} inferred from Deeg et al. 1997 (middle centre); *Spitzer* $24 \mu\text{m}$ (bottom left); *Spitzer* $70 \mu\text{m}$ (bottom centre). We also show the RC that was isolated by the RC-based masking technique (top right). The greyscale intensity scales used are arbitrary to best highlight structure.

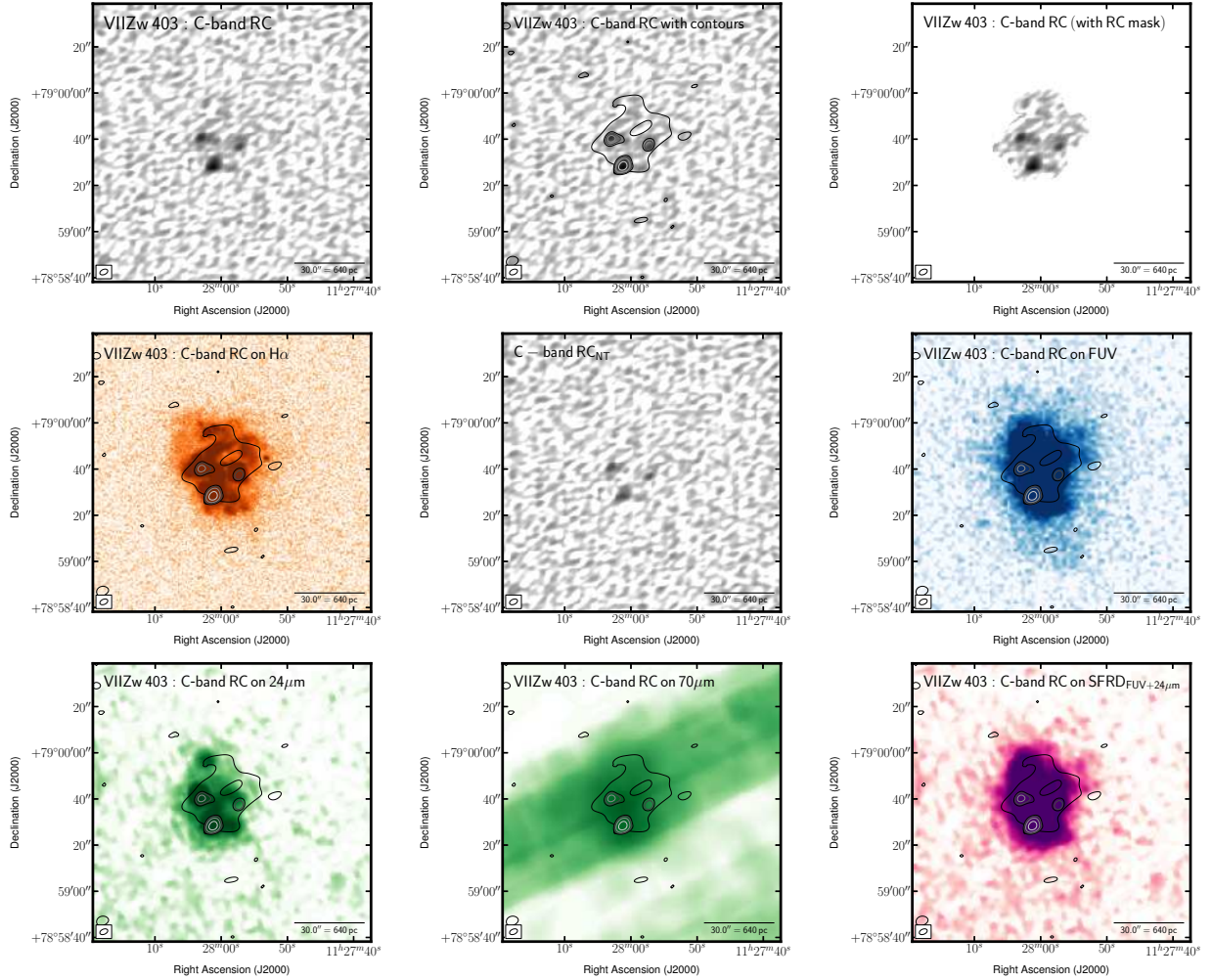


Fig. 50.— Multi-wavelength coverage of VII Zw 403 displaying a $2' \times 2'$ area. We show total RC flux density at the native resolution (top left) and again with contours (top centre). The lowest contour highlights low-surface brightness emission at a level of $18.7 \mu\text{Jy beam}^{-1}$ —this is 2.5 times the rms after smoothing the native image by a factor of 2.5. The other contours are placed following $(2 + 2^n)\sigma_{\text{native}}$, where $n \geq 0$ and both the rms ($\sigma_{\text{native}} = 6.30 \mu\text{Jy beam}^{-1}$) and the resolution ($\text{FWHM}_{\text{native}} = 3.6 \times 2.2$ arcsec) are taken from the native resolution image. These same contours are also superposed on ancillary LITTLE THINGS images where possible: $\text{H}\alpha$ (middle left); RC_{NT} inferred from Deeg et al. 1997 (middle centre); *GALEX* FUV (middle right); *Spitzer* $24 \mu\text{m}$ (bottom left); *Spitzer* $70 \mu\text{m}$ (bottom centre); $\text{FUV} + 24 \mu\text{m}$ –inferred SFRD from Leroy et al. 2012 (bottom right). We also show the RC that was isolated by the RC–based masking technique (top right). The greyscale intensity scales used are arbitrary to best highlight structure.

C. RC-based mask tests

We performed a number of tests to ensure our RC-based masking technique was suitable for isolating RC emission. We checked its ability to:

1) retrieve strong emission—we created an extended source of known flux density, added noise, and then created the RC-based mask to retrieve emission (see Figure 52; top panels)—the input flux density and isolated flux density were consistent;

2) retrieve weak emission—we created an unresolved source (of brightness $X\mu\text{Jy}$) and an extended source (of brightness $X\mu\text{Jy beam}^{-1}$), and over 20 iterations, added noise characterised with a variance $\sigma_{\text{rms}} = 1$, and average, $\mu = 0$ (see Figure 52; middle panels). We found that the retrieval rate for unresolved sources drops below 90% for sources below $X = 5\sigma$ (corresponding to $\sim 0.03\text{ mJy}$ in our sample) and for extended sources, this occurs below a source strength of $X = 3\sigma$ ($\sim 0.02\text{ mJy}$);

In our analysis, we were forced to integrate only the tips of the icebergs (i.e., only the significant RC emission) which means any low surface-brightness (read: weak) emission may have been overlooked. RC emission was isolated if it exhibited a significant amount in either the native resolution or the smoothed map.

We tested how this may have affected our results by looking at only those dwarfs that exhibited significant pockets of RC (emission isolated by the RC-based mask; see Figure 6) and find that the isolated quantities were consistent with disk integrated fluxes.

3) avoid interpreting noise as real emission—we used `python` to generate a map of noise characterised with $\sigma = 1$ and $\mu = 0$, and then created the RC-based mask to isolate emission that exceeded σ_{max} (see Equation 1 and Figure 52; bottom panels).

D. Comparison with literature number counts

With a similar observing setup to ours, but using the Australia Telescope Compact Array (ATCA), Huynh et al. (2012) conducted a 900 arcminute² survey at 5.5 GHz with a synthesised beam of $4.9'' \times 2.0''$ reaching an rms noise of $12\mu\text{Jy beam}^{-1}$. After correcting for incompleteness, they present their source counts (sources $\text{sr}^{-1} \text{Jy}^{-1}$) in 10 bins between 50 and 5000 μJy .

Our images were generated using a synthesised beam of approximately $3''$ and therefore, our sensitivity per beam per second was roughly the same as that of Huynh et al. (2012). Sources were counted from two distinct regions in our images: from within the confine of the galaxy disk, and from outside of the galaxy disk.

After converting the Huynh et al. (2012) bins (see their Table 2) to 6.2 GHz (the effective frequency for most of our images) assuming a spectral index of -0.7 , we cycled through each RC image and counted all the discrete sources of RC emission that had a flux density in the range ΔS . A source was counted if its S/N was greater than 5 and if the primary beam attenuation was at most 0.4. No attempt was made to count resolved sources of emission (e.g., radio lobes, multiple SF regions from a dwarf, etc.) as originating from a single source. The 6.2 GHz source counts are presented in Table 4.

The sources counted from outside of the dwarf galaxy disk can be used as a control; in this region, there is, by definition, no local SF and thus no RC emission is expected other than from the general background. When compared with Huynh et al. (2012), we find that half of our bins disagree (see column 8 of Table 4).

From within the disk, a bias is expected towards observing more RC emission; as SF is observed from within the dwarf galaxy disks, extra RC emission would be expected on top of any background sources. We indeed find a significant excess of discrete RC sources from within the dwarf galaxy disk (see column 5 of Table 4); this is most noticeable in the third and fourth bins. These two bins are equivalent to a region forming stars at a rate of 0.9×10^{-4} and $1.5 \times 10^{-4} M_{\odot} \text{yr}^{-1}$ assuming the Condon et al. 2002 RC-SFR relation at a distance of 5 Mpc, respectively.

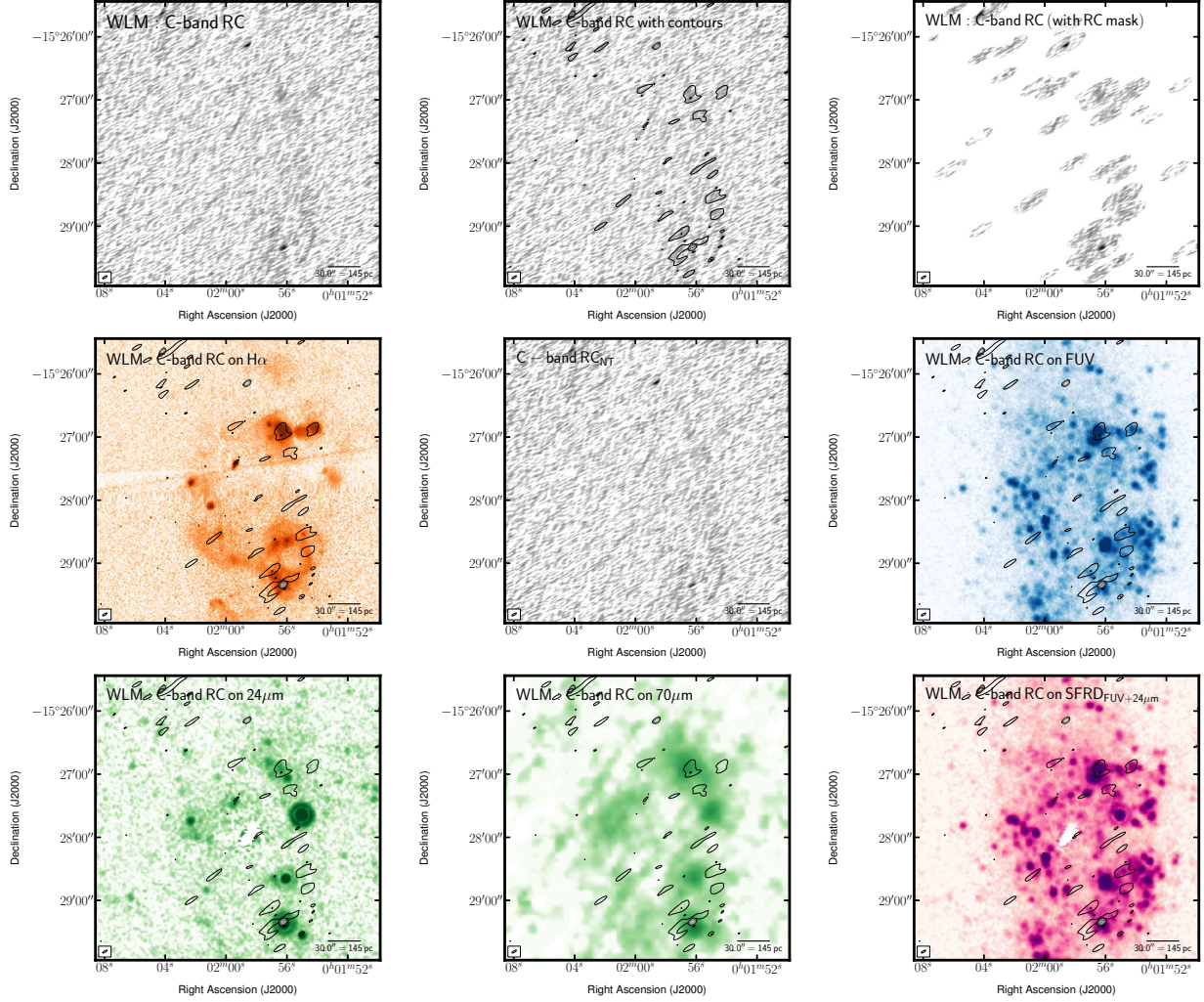


Fig. 51.— Multi-wavelength coverage of WLM displaying a $4' \times 4'$ area. We show total RC flux density at the native resolution (top left) and again with contours (top centre). The lowest contour highlights low-surface brightness emission at a level of $27.6 \mu\text{Jy beam}^{-1}$ —this is 2.5 times the rms after smoothing the native image by a factor of 2.5. The other contours are placed following $(2 + 2^n)\sigma_{\text{native}}$, where $n \geq 0$ and both the rms ($\sigma_{\text{native}} = 5.33 \mu\text{Jy beam}^{-1}$) and the resolution ($\text{FWHM}_{\text{native}} = 5.0 \times 1.5 \text{ arcsec}$) are taken from the native resolution image. These same contours are also superposed on ancillary LITTLE THINGS images where possible: $\text{H}\alpha$ (middle left); RC_{NTb} inferred from Deeg et al. 1997 (middle centre); *GALEX* FUV (middle right); *Spitzer* $24 \mu\text{m}$ (bottom left); *Spitzer* $70 \mu\text{m}$ (bottom centre); FUV+ $24 \mu\text{m}$ -inferred SFRD from Leroy et al. 2012 (bottom right). We also show the RC that was isolated by the RC-based masking technique (top right). The greyscale intensity scales used are arbitrary to best highlight structure.

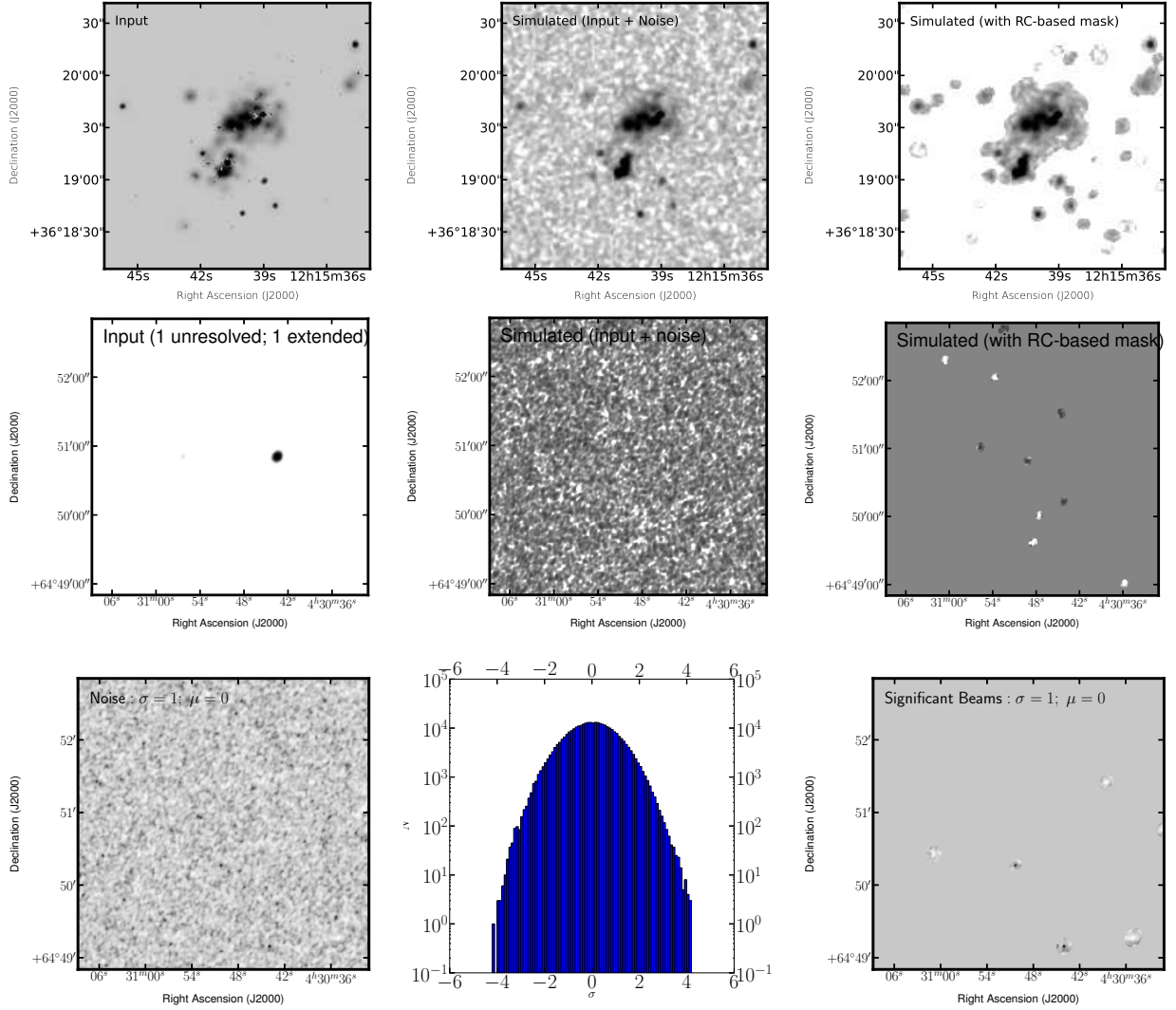


Fig. 52.— *Top*: Test to examine ability of the RC-based masking technique to retrieve strong RC emission. We created an extended source of known flux density (left), added noise (centre), and then applied our RC-based masking procedure to isolate RC emission that exceeded σ_{\max} (right). *Middle*: Test to examine ability of the RC-based masking technique to retrieve weak RC emission. We created an unresolved source and an extended source (left), and added noise characterised with a variance, $\sigma_{\text{rms}} = 1$, and average, $\mu = 0$ (centre). We then applied our RC-based masking procedure to isolate RC emission that exceeded σ_{\max} (right). In this case, neither the resolved nor the unresolved source was retrieved. *Bottom*: Test to examine ability of the RC-based masking technique to avoid interpreting noise as real emission. We generated a map of noise characterised with $\sigma = 1$ and $\mu = 0$ (left and centre), and then applied our RC-based masking procedure to isolate RC emission that exceeded σ_{\max} (right). In this case, 5 beams (2 positive; 3 negative) are interpreted as being significant.

Column 9 of Table 4 gives the ratio of count rates from within the disk to that outside of the disk. A bias is expected towards observing more RC sources from within the disk (as SF is observed from within the dwarf galaxy disks). The ratios are largely consistent with 1 implying that our observations were not very

sensitive to the RC emission originating from the dwarf galaxy, but there are bins where we indeed observe a greater density of sources from within the disk than outside of it.

TABLE 4
C-BAND SOURCE COUNTS

		Within disk			Out of disk			Ratio
ΔS (μJy) (1)	$\langle S \rangle$ (μJy) (2)	N (3)	dN/dS ($\text{sr}^{-1} \text{Jy}^{-1}$) (4)	Ratio (5)	N (6)	dN/dS ($\text{sr}^{-1} \text{Jy}^{-1}$) (7)	Ratio (8)	Ratio (9)
72–115	93	17	6.6×10^9	0.9 ± 0.3	51	4.9×10^9	0.7 ± 0.1	1.4 ± 0.5
115–182	150	18	4.3×10^9	1.8 ± 0.5	46	2.6×10^9	1.1 ± 0.2	1.7 ± 0.6
182–289	246	16	2.4×10^9	3.8 ± 1.2	15	5.2×10^8	0.8 ± 0.3	4.5 ± 2.1
289–459	394	7	6.4×10^8	1.7 ± 0.9	14	3.0×10^8	0.8 ± 0.3	2.1 ± 1.4
459–728	605	5	3.0×10^8	0.9 ± 0.6	15	2.1×10^8	0.6 ± 0.2	1.4 ± 1.1
728–1154	983	1	3.7×10^7	0.4 ± 0.9	6	5.2×10^7	0.5 ± 0.3	0.7 ± 1.7
1154–1830	1536	4	9.4×10^7	2.3 ± 1.9	3	1.7×10^7	0.4 ± 0.4	5.6 ± 7.1
1830–2901	2019	3	5.4×10^7	2.9 ± 2.8	4	1.7×10^7	0.9 ± 0.7	3.2 ± 4.0
2901–4597	3452	1	1.1×10^7	0.7 ± 1.6	4	9.9×10^6	0.6 ± 0.5	1.1 ± 2.6
4597–11477	8619	1	4.2×10^6	...	2	2.0×10^6	...	2.1 ± 5.7
11477–28653	21515	1	1.7×10^6	...	2	8.0×10^5	...	2.1 ± 5.7

NOTE.—Column 1: 6.2 GHz flux density range of bin; Column 2: 6.2 GHz equivalent flux density of bin; Column 3/6: Number of sources in bin; Column 4/7: Number of sources in bin normalised by equivalent flux density and solid angle; Column 5/8: Ratio of normalised source counts from this study to that of Huynh et al. (2012). Due to the low number counts, uncertainties on the number count, N , are calculated through the $1 + \sqrt{N + 0.75}$ approximation (see Equation 7 of Gehrels 1986); Column 9: Ratio of source counts from within the dwarf galaxy disk to that outside.

TABLE 5

THE GALAXY SAMPLE THIS IS HOW TABLE 1 SHOULD LOOK LIKE!

Galaxy	Other names ^a	D (Mpc)	Ref ^b	M_V (mag)	R_H^c (arcmin)	R_D^c (kpc)	$E(B - V)^d$	$\log_{10} \Sigma_{SFR,D}^{H\alpha}$ ($M_{\odot} \text{yr}^{-1} \text{kpc}^{-2}$) ^e	$\log_{10} \Sigma_{SFR,D}^{FUV}$ ($M_{\odot} \text{yr}^{-1} \text{kpc}^{-2}$) ^e	$12 + \log_{10} \text{O}/\text{H}^f$	Ref ^g
Im Galaxies											
CVnIdwA	UGCA 292	3.6	1	-12.4	0.87	0.57 ± 0.12	0.01	-2.58 ± 0.01	-2.48 ± 0.01	7.3 ± 0.06	24
DDO 43	PGC 21073, UGC 3860	7.8	2	-15.1	0.89	0.41 ± 0.03	0.05	-1.78 ± 0.01	-1.55 ± 0.01	8.3 ± 0.09	25
DDO 46	PGC 21585, UGC 3966	6.1	...	-14.7	...	1.14 ± 0.06	0.05	-2.89 ± 0.01	-2.46 ± 0.01	8.1 ± 0.1	25
DDO 47	PGC 21600, UGC 3974	5.2	3	-15.5	2.24	1.37 ± 0.06	0.02	-2.70 ± 0.01	-2.40 ± 0.01	7.8 ± 0.2	26
DDO 50	PGC 23324, UGC 4305, Holmberg II, VII Zw 223	3.4	1	-16.6	3.97	1.10 ± 0.05	0.02	-1.67 ± 0.01	-1.55 ± 0.01	7.7 ± 0.14	27
DDO 52	PGC 23769, UGC 4426	10.3	4	-15.4	1.08	1.30 ± 0.13	0.03	-3.20 ± 0.01	-2.43 ± 0.01	(7.7)	28
DDO 53	PGC 24050, UGC 4459, VII Zw 238	3.6	1	-13.8	1.37	0.72 ± 0.06	0.03	-2.42 ± 0.01	-2.41 ± 0.01	7.6 ± 0.11	27
DDO 63	PGC 27605, Holmberg I, UGC 5139, Mailyan 044	3.9	1	-14.8	2.17	0.68 ± 0.01	0.01	-2.32 ± 0.01	-1.95 ± 0.00	7.6 ± 0.11	27
DDO 69	PGC 28868, UGC 5364, Leo A	0.8	5	-11.7	2.40	0.19 ± 0.01	0.00	-2.83 ± 0.01	-2.22 ± 0.01	7.4 ± 0.10	29
DDO 70	PGC 28913, UGC 5373, Sextans B	1.3	6	-14.1	3.71	0.48 ± 0.01	0.01	-2.85 ± 0.01	-2.16 ± 0.00	7.5 ± 0.06	30
DDO 75	PGC 29653, UGCA 205, Sextans A	1.3	7	-13.9	3.09	0.22 ± 0.01	0.02	-1.28 ± 0.01	-1.07 ± 0.01	7.5 ± 0.06	30
DDO 87	PGC 32405, UGC 5918, VII Zw 347	7.7	...	-15.0	1.15	1.31 ± 0.12	0.00	-1.36 ± 0.01	-1.00 ± 0.01	7.8 ± 0.04	31
DDO 101	PGC 37449, UGC 6900	6.4	...	-15.0	1.05	0.94 ± 0.03	0.01	-2.85 ± 0.01	-2.81 ± 0.01	8.7 ± 0.03	25
DDO 126	PGC 40791, UGC 7559	4.9	8	-14.9	1.76	0.87 ± 0.03	0.00	-2.37 ± 0.01	-2.10 ± 0.01	(7.8)	28
DDO 133	PGC 41636, UGC 7698	3.5	...	-14.8	2.33	1.24 ± 0.09	0.00	-2.88 ± 0.01	-2.62 ± 0.01	8.2 ± 0.09	25
DDO 154	PGC 43869, UGC 8024, NGC 4789A	3.7	...	-14.2	1.55	0.59 ± 0.03	0.01	-2.50 ± 0.01	-1.93 ± 0.01	7.5 ± 0.09	27
DDO 155	PGC 44491, UGC 8091, GR 8, LSB C D646-07	2.2	9	-12.5	0.95	0.15 ± 0.01	0.01	-1.44 ± 0.01	...	7.7 ± 0.06	29
DDO 165	PGC 45372, UGC 8201, IIZw 499, Mailyan 82	4.6	10	-15.6	2.14	2.26 ± 0.08	0.01	-3.67 ± 0.01	...	7.6 ± 0.08	27
DDO 167	PGC 45939, UGC 8308	4.2	8	-13.0	0.75	0.33 ± 0.05	0.00	-2.36 ± 0.01	-1.83 ± 0.01	7.7 ± 0.2	26
DDO 168	PGC 46039, UGC 8320	4.3	8	-15.7	2.32	0.82 ± 0.01	0.00	-2.27 ± 0.01	-2.04 ± 0.01	8.3 ± 0.07	25
DDO 187	PGC 50961, UGC 9128	2.2	1	-12.7	1.06	0.18 ± 0.01	0.00	-2.52 ± 0.01	-1.98 ± 0.01	7.7 ± 0.09	32
DDO 210	PGC 65367, Aquarius Dwarf	0.9	10	-10.9	1.31	0.17 ± 0.01	0.03	...	-2.71 ± 0.06	(7.2)	28
DDO 216	PGC 71538, UGC 12613, Peg DIG, Pegasus Dwarf	1.1	11	-13.7	4.00	0.54 ± 0.01	0.02	-4.10 ± 0.07	-3.21 ± 0.01	7.9 ± 0.15	33
F564-V3	LSBC D564-08	8.7	4	-14.0	...	0.53 ± 0.03	0.02	...	-2.79 ± 0.02	(7.6)	28
IC 10	PGC 1305, UGC 192	0.7	12	-16.3	...	0.40 ± 0.01	0.75	-1.11 ± 0.01	...	8.2 ± 0.12	34
IC 1613	PGC 3844, UGC 668, DDO 8	0.7	13	-14.6	9.10	0.58 ± 0.02	0.00	-2.56 ± 0.01	-1.99 ± 0.01	7.6 ± 0.05	35
LGS 3	PGC 3792, Pisces dwarf	0.7	14	-9.7	0.96	0.23 ± 0.02	0.04	...	-3.88 ± 0.06	(7.0)	28
M81dwA	PGC 23521	3.5	15	-11.7	...	0.26 ± 0.00	0.02	...	-2.26 ± 0.01	(7.3)	28
NGC 1569	PGC 15345, UGC 3056, Arp 210, VII Zw 16	3.4	16	-18.2	...	0.38 ± 0.02	0.51	0.19 ± 0.01	-0.01 ± 0.01	8.2 ± 0.05	36
NGC 2366	PGC 21102, UGC 3851, DDO 42	3.4	17	-16.8	4.72	1.36 ± 0.04	0.04	-1.67 ± 0.01	-1.66 ± 0.01	7.9 ± 0.01	37
NGC 3738	PGC 35856, UGC 6565, Arp 234	4.9	3	-17.1	2.40	0.78 ± 0.01	0.00	-1.66 ± 0.01	-1.53 ± 0.01	8.4 ± 0.01	25
NGC 4163	PGC 38881, NGC 4167, UGC 7199	2.9	1	-14.4	1.47	0.27 ± 0.03	0.00	-2.28 ± 0.13	-1.74 ± 0.01	7.9 ± 0.2	38
NGC 4214	PGC 39225, UGC 7278	3.0	1	-17.6	4.67	0.75 ± 0.01	0.00	-1.03 ± 0.01	-1.08 ± 0.01	8.2 ± 0.06	39
SagDIG	PGC 63287, Lowal's Object	1.1	19	-12.5	...	0.23 ± 0.03	0.14	-2.97 ± 0.04	-2.11 ± 0.01	7.3 ± 0.1	35
UGC 8508	PGC 47495, IZw 60	2.6	1	-13.6	1.28	0.27 ± 0.01	0.00	-2.03 ± 0.01	...	7.9 ± 0.2	38
WLM	PGC 143, UGCA 444, DDO 221, Wolf-Lundmark-Melott	1.0	20	-14.4	5.81	0.57 ± 0.03	0.02	-2.77 ± 0.01	-2.05 ± 0.01	7.8 ± 0.06	40
BCD Galaxies											
Haro 29	PGC 40665, UGCA 281, Mrk 209, I Zw 36	5.8	21	-14.6	0.84	0.29 ± 0.01	0.00	-0.77 ± 0.01	-1.07 ± 0.01	7.9 ± 0.07	41
Haro 36	PGC 43124, UGC 7950	9.3	...	-15.9	...	0.69 ± 0.01	0.00	-1.86 ± 0.01	-1.55 ± 0.01	8.4 ± 0.08	25
Mrk 178	PGC 35684, UGC 6541	3.9	8	-14.1	1.01	0.33 ± 0.01	0.00	-1.60 ± 0.01	-1.66 ± 0.01	7.7 ± 0.02	42
VII Zw 403	PGC 35286, UGC 6456	4.4	22,23	-14.3	1.11	0.52 ± 0.02	0.02	-1.71 ± 0.01	-1.67 ± 0.01	7.7 ± 0.01	25

^aSelected alternate identifications obtained from NED.^bReference for the distance to the galaxy. If no reference is given, the distance was determined from the galaxy's radial velocity, given by de Vaucouleurs et al. (1991), corrected for infall to the Virgo Cluster (Mould et al. 2000) and a Hubble constant of $73 \text{ km s}^{-1} \text{ Mpc}^{-1}$.^c R_H is the Holmberg radius, the radius of the galaxy at a B -band isophote, corrected for reddening, of $26.7 \text{ mag arcsec}^{-2}$. R_D is the disk scale length measured from V -band images. (Table from Hunter & Elmegreen 2006).^dForeground reddening from Burstein & Heiles (1984).^e $\text{SFR}_D^{H\alpha}$ is the SF rate, measured from $H\alpha$, normalized to the area πR_D^2 , where R_D is the disk scale length (Hunter & Elmegreen 2004). SFR_D^{FUV} is the SF rate determined from *GALEX* FUV fluxes (Hunter et al. 2010, with an update of the *GALEX* FUV photometry to the GR4/GR5 pipeline reduction).^fValues in parentheses were determined from the empirical relationship between oxygen abundance and M_B given by Richer & McCall (1995) and are particularly uncertain.

References. — (1) Dalcanton et al. 2009; (2) Karachentsev et al. 2004; (3) Karachentsev et al. 2003a; (4) Karachentsev et al. 2006; (5) Dolphin et al. 2002; (6) Sakai et al. 2004; (7) Dolphin et al. 2003; (8) Karachentsev et al. 2003b; (9) Tolstoy et al. 1995a; (10) Karachentsev et al. 2002; (11) Meschin et al. 2009; (12) Sakai et al. 1999; (13) Pietrzynski et al. 2006; (14) Miller et al. 2001; (15) Freedman et al. 2001; (16) Grocholski et al. 2008; (17) Tolstoy et al. 1995b; (18) Gieren et al. 2006; (19) Momany et al. 2002; (20) Gieren et al. 2008; (21) Schulte-Ladbeck et al. 2001; (22) Lynds et al. 1998; (23) Méndez et al. 2002; (24) van Zee & Haynes 2006; (25) Hunter & Hoffman 1999; (26) Skillman, Kennicutt, & Hodge 1989; (27) Moustakas et al. 2010; (28) Richer & McCall 1995; (29) van Zee et al. 2006; (30) Kniazev et al. 2005; (31) Croxall et al. 2009; (32) Lee et al. 2003b; (33) Skillman et al. 1997; (34) Lequex et al. 1979; (35) Lee et al. 2003a; (36) Kobulnicky & Skillman 1997; (37) González-Delgado et al. 1994; (38) Moustakas & Kennicutt (2006); (39) Masegosa et al. 1991; (40) Lee et al. 2005; (41) Viallefond & Thuan 1983; (42) González-Riestra et al. 1988.

Bell (2003) talk about RC not being a good SF indicator on pages 800-801.

Ramya,Prabhu,Sahu 2012: The star formation rates (SFR) estimated from H α match well with the SFR estimated using non-thermal radio emission for individual star forming regions, but are $\sim 6 - 7$ times less as compared to the SFR calculated from FIR emission.

Irwin,Brar,Saikia,Henriksen 2013: The non-linear relation between synchrotron emission and cold dust can be understood if the heating of the cold dust is the ISRF in which cooler stars (rather than hot young stars) dominate, leading to variations in cold dust emission that are dominated by density rather than temperature variations. Synchrotron emission depends on the magnetic field strength and CR electron generation, both of which depend on gas density via $B \propto \sqrt{\rho}$ and the Schmidt law, respectively. With these assumptions, $S_{617} \propto S_{850}^{2.2}$ which agrees with the observed correlation.

Rabidoux,Pisano,Kepley,Johnson 2013: We confirm that the RC-FIR correlation holds for the unresolved galaxies total 33 GHz flux.

Run a test: Make an image of a galaxy using a uv range. Then smooth the native resolution image up to the resolution of the uvtapered image. Then take a ratio of the images.

Make sure that, for a galaxy largely free of dust, the FUV+24 μ m- and FUV-inferred SFRDs are the *same!*

Question is: Is the Holmberg radius a suitable radius to define as the disk oength? We are saying that we expect non-thermal emission to extend, as a maximum, to the size of the galaxy, but the Holmberg radius doesn't necessarily define the extent to which the non-thermal emission may extend. Find a study that relates the Holberg Radius to the extent of the radio disk.

Examples of Preprints

Smith, A. B. 1999, arXiv:astro-ph/9812345 (style for preprints before April 2007)

Smith, A. B. 2007, arXiv:0702.1234 (style for preprints after April 2007)

Lockwood, G. W., & Skiff, B. A. 1988, Air Force Geophys. Lab. preprint (AFGL-TR-88-0221)

References to preprints are acceptable only for papers not yet published. For papers that have been accepted but are not yet published, the preprint number may be given at the end of a reference submitted or in press (i.e., Smith, A. B. 1999, AJ, in press (arXiv:astro-ph/9912345)).

Papers Submitted or In Press

Wolk, S. J., & Walter, F. M. 1999, AJ, submitted

Wolk, S. J., & Walter, F. M. 1999, AJ, in press

TABLE 6

INTEGRATED EMISSION OVER THE DWARF DISK THIS IS HOW TABLE SHOULD LOOK LIKE

Galaxy	R.A	Dec.	Size	P.A	f_{disk}	C-band RC	H α	FUV	24 μ m MIR	70 μ m FIR	C-band RC $_{\text{NTTh}}$	B_{eq}	Notes
(1)	hh mm ss.s	dd mm ss.s	(')	($^{\circ}$)	(%)	(mJy)	(10^{-13} ergs s $^{-1}$ cm $^{-2}$)	(mJy)	(10^{-2} Jy)	(10^{-2} Jy)	(mJy)	(μ G)	(14)
	(2)	(3)	(4)	(5)	(6)	(7)	(8)	(9)	(10)	(11)	(12)	(13)	
CVn I dwA	12 38 40.2	+32 45 40	1.7 \times 1.4	80	12	0.12 \pm 0.04 (−0.01)	1.95 \pm 0.03	0.99 \pm 0.02	0.30 \pm 0.01	3.58 \pm 0.05	0.05 \pm 0.04 (−0.01)	< 6	B,L
DDO 43	07 28 17.8	+40 46 13	1.8 \times 1.2	6	5	0.28 \pm 0.05 (0.00)	1.16 \pm 0.02	0.66 \pm 0.01	0.25 \pm 0.05 (0.00)	10	B,L
DDO 46	07 41 26.6	+40 06 39	3.8 \times 3.4	84	6	1.39 \pm 0.08 (1.31)	1.00 \pm 0.02	1.16 \pm 0.01	1.35 \pm 0.08 (1.31)	6	V
DDO 47	07 41 55.3	+16 48 08	4.5 \times 2.3	−79	3	0.35 \pm 0.05 (0.09)	2.88 \pm 0.02	2.31 \pm 0.01	0.32 \pm 0.05 (0.09)	7	B,L
DDO 50	08 19 08.7	+70 43 25	7.9 \times 5.7	18	3	6.09 \pm 0.14 (0.59)	57.32 \pm 0.46	32.24 \pm 0.15	20.18 \pm 0.03	359.90 \pm 0.32	3.63 \pm 0.14 (0.57)	10	B
DDO 52	08 28 28.5	+41 51 21	2.2 \times 1.4	4	2	0.11 \pm 0.04 (0.00)	0.27 \pm 0.01	0.45 \pm 0.00	−0.04 \pm 0.00	2.05 \pm 0.06	0.11 \pm 0.04 (0.00)	< 10	B,L
DDO 53	08 34 08.0	+66 10 37	2.7 \times 1.4	81	4	0.41 \pm 0.05 (0.14)	4.25 \pm 0.04	1.99 \pm 0.02	2.87 \pm 0.00	28.53 \pm 0.03	0.25 \pm 0.05 (0.13)	8	B,L
DDO 63	09 40 30.4	+71 11 02	4.3 \times 4.3	0	6	1.79 \pm 0.07 (1.53)	4.12 \pm 0.02	3.41 \pm 0.02	2.09 \pm 0.01	4.32 \pm 0.11	1.64 \pm 0.07 (1.52)	6	B
DDO 69	09 59 25.0	+30 44 42	4.8 \times 2.7	−64	3	0.86 \pm 0.08 (0.68)	1.66 \pm 0.01	4.11 \pm 0.02	−0.75 \pm 0.01	13.22 \pm 0.08	0.85 \pm 0.08 (0.68)	9	B,L
DDO 70	10 00 00.9	+05 19 50	7.4 \times 4.4	88	2	1.92 \pm 0.09 (1.54)	6.09 \pm 0.04	9.07 \pm 0.05	0.69 \pm 0.02	70.15 \pm 0.15	1.72 \pm 0.09 (1.54)	6	B,L
DDO 75	10 10 59.2	−04 41 56	6.2 \times 5.2	42	1	0.73 \pm 0.13 (0.28)	43.30 \pm 0.10	23.74 \pm 0.07	0.31 \pm 0.02	102.60 \pm 0.25	0.39 \pm 0.13 (0.26)	< 9	B,L
DDO 87	10 49 34.7	+65 31 46	2.3 \times 1.3	76	8	0.12 \pm 0.05 (0.10)	0.67 \pm 0.01	0.59 \pm 0.01	0.10 \pm 0.00	6.78 \pm 0.04	0.10 \pm 0.05 (0.10)	< 7	B,L
DDO 101	11 55 39.4	+31 31 08	2.1 \times 1.5	−69	4	0.00 \pm 0.08 (0.00)	0.79 \pm 0.01	0.33 \pm 0.00	0.27 \pm 0.01	−0.77 \pm 0.04	0.00 \pm 0.08 (0.00)	< 10	B,L
DDO 126	12 27 06.5	+37 08 23	3.5 \times 1.7	−41	3	0.31 \pm 0.05 (0.00)	3.61 \pm 0.04	2.62 \pm 0.02	0.37 \pm 0.01	17.12 \pm 0.06	0.17 \pm 0.05 (0.00)	7	B,L
DDO 133	12 32 55.4	+31 32 14	4.7 \times 3.2	−6	5	0.68 \pm 0.07 (0.52)	4.53 \pm 0.04	3.72 \pm 0.03	0.78 \pm 0.02	35.31 \pm 0.20	0.55 \pm 0.07 (0.51)	6	B,L
DDO 154	12 54 06.2	+27 09 02	3.1 \times 1.6	46	0	−0.01 \pm 0.01 (0.00)	2.18 \pm 0.02	3.49 \pm 0.02	0.29 \pm 0.01	3.54 \pm 0.05	−0.01 \pm 0.01 (0.00)	< 13	B,L
DDO 155	12 58 39.8	+14 13 10	1.9 \times 1.3	51	7	0.23 \pm 0.05 (0.00)	4.65 \pm 0.06	...	0.24 \pm 0.01	18.20 \pm 0.08	0.04 \pm 0.05 (0.00)	< 9	B,L
DDO 165	13 06 25.3	+67 42 25	4.3 \times 2.3	89	6	0.16 \pm 0.06 (0.01)	1.47 \pm 0.01	...	0.05 \pm 0.01	7.79 \pm 0.06	0.16 \pm 0.06 (0.01)	< 5	B,L
DDO 167	13 13 22.9	+46 19 11	1.5 \times 1.0	−24	0	0.00 \pm 0.00 (0.00)	0.79 \pm 0.01	0.97 \pm 0.01	B,L
DDO 168	13 14 27.2	+45 55 46	4.6 \times 2.9	−25	2	0.37 \pm 0.07 (0.11)	5.80 \pm 0.03	4.91 \pm 0.03	0.80 \pm 0.01	44.96 \pm 0.14	0.26 \pm 0.07 (0.11)	7	B,L
DDO 187	14 15 56.7	+23 03 19	2.1 \times 1.7	37	1	−0.05 \pm 0.03 (0.00)	0.55 \pm 0.01	0.95 \pm 0.01	−0.02 \pm 0.01	−2.57 \pm 0.10	−0.05 \pm 0.03 (0.00)	< 10	B,L
DDO 210	20 46 52.0	−12 50 50	2.6 \times 1.3	−85	3	0.47 \pm 0.03 (0.32)	...	0.53 \pm 0.01	−0.19 \pm 0.01	6.08 \pm 0.04	B,L
DDO 216	23 28 35.0	+14 44 30	8.0 \times 3.6	−58	1	−0.01 \pm 0.04 (0.05)	0.10 \pm 0.01	1.15 \pm 0.01	−0.01 \pm 0.01	10.73 \pm 0.09	−0.01 \pm 0.04 (0.05)	< 7	B,L
F564-V03	09 02 53.9	+20 04 29	1.3 \times 1.0	7	7	0.06 \pm 0.03 (−0.00)	...	0.08 \pm 0.00	V,L
Haro 29	12 26 16.7	+48 29 38	1.7 \times 1.4	85	17	1.70 \pm 0.08 (0.00)	12.95 \pm 0.36	8.91 \pm 0.24	6.71 \pm 0.01	36.08 \pm 0.05	0.53 \pm 0.08 (0.00)	9	B
Haro 36	12 46 56.3	+51 36 48	1.5 \times 1.2	90	9	0.22 \pm 0.05 (0.00)	2.19 \pm 0.02	2.56 \pm 0.05	1.07 \pm 0.00	26.65 \pm 0.06	0.15 \pm 0.05 (0.00)	< 8	V,L
IC 1613	01 05 00.0	+02 06 55	18.2 \times 14.7	71	17	1.72 \pm 0.21 (0.50)	46.28 \pm 0.19	54.47 \pm 0.27	4.09 \pm 0.05	364.30 \pm 0.50	1.72 \pm 0.21 (0.50)	6	B,L
IC 10	00 20 17.5	+59 18 14	11.6 \times 9.1	−38	8	95.69 \pm 0.30 (0.00)	90.78 \pm 0.44	89.79 \pm 0.30 (0.00)	19	V
LGS 3	01 03 55.2	+21 52 39	1.9 \times 1.0	−3	1	0.02 \pm 0.01 (0.00)	...	0.06 \pm 0.00	B,L
M81 dwA	08 23 27.2	+71 01 51	1.5 \times 1.1	86	1	0.02 \pm 0.03 (0.00)	...	0.33 \pm 0.00	V,L
Mrk 178	11 33 29.0	+49 14 24	2.0 \times 0.9	−51	8	0.42 \pm 0.05 (0.00)	0.49 \pm 0.01	...	0.51 \pm 0.00	0.51 \pm 0.00	0.42 \pm 0.05 (0.00)	10	B
NGC 1569	04 30 49.8	+64 50 51	2.3 \times 1.3	−59	100	151.50 \pm 0.24 (1.60)	156.70 \pm 0.97	2.43 \pm 0.04	802.60 \pm 3.05	4069.00 \pm 3.04	136.70 \pm 0.25 (1.60)	24	V
NGC 2366	07 28 48.8	+69 12 22	9.4 \times 4.0	33	6	11.62 \pm 0.19 (0.07)	91.03 \pm 1.08	27.69 \pm 0.18	74.60 \pm 0.02	572.10 \pm 0.36	5.04 \pm 0.21 (0.06)	9	B
NGC 3738	11 35 49.0	+54 31 23	4.8 \times 4.8	0	19	2.87 \pm 0.15 (0.00)	15.99 \pm 0.17	10.31 \pm 0.15	13.17 \pm 0.01	279.70 \pm 0.46	1.71 \pm 0.15 (0.00)	10	B
NGC 4163	12 12 09.2	+36 10 13	2.9 \times 1.9	18	2	0.06 \pm 0.02 (0.02)	1.43 \pm 0.02	2.27 \pm 0.05	0.50 \pm 0.01	10.93 \pm 0.12	0.06 \pm 0.02 (0.02)	< 7	B,L
NGC 4214	12 15 39.2	+36 19 38	9.3 \times 8.5	16	6	23.40 \pm 0.26 (0.45)	175.60 \pm 0.89	68.53 \pm 0.35	226.60 \pm 0.06	2715.00 \pm 1.26	11.57 \pm 0.27 (0.77)	12	B
Sag DIG	19 30 00.6	−17 40 56	4.3 \times 2.3	88	4	0.44 \pm 0.11 (0.42)	1.04 \pm 0.01	1.65 \pm 0.01	0.44 \pm 0.11 (0.42)	9	V,L
UGC 8508	13 30 44.9	+54 54 29	2.5 \times 1.4	−60	3	0.58 \pm 0.04 (0.51)	2.83 \pm 0.04	...	0.45 \pm 0.01	14.79 \pm 0.06	0.53 \pm 0.04 (0.50)	10	B,L
VII Zw 403	11 27 58.2	+78 59 39	2.2 \times 1.1	−11	16	0.89 \pm 0.07 (0.00)	7.06 \pm 0.12	2.70 \pm 0.05	2.14 \pm 2.20	64.66 \pm 1.26	0.31 \pm 0.07 (0.00)	7	B
WLM	00 01 59.2	−15 27 41	11.6 \times 5.1	−2	15	2.10 \pm 0.20 (0.14)	15.80 \pm 0.06	21.59 \pm 0.07	4.97 \pm 0.01	128.10 \pm 0.20	1.41 \pm 0.20 (0.14)	5	B,L

NOTE.—Column 1: Name of dwarf galaxy ; Columns 2/3: Celestial coordinates (J2000) of centre of optical disk; Column 4/5: Size (major and minor axes) and position angle (P.A) of optical disk (Hunter & Elmegreen 2006); Column 6: Proportion of the disk isolated by the RC-based masking technique; Column 7: C-band (\sim 6 GHz) radio continuum flux density. The RC quantity in parenthesis is the amount that was regarded as ‘ambiguous’; Column 8: H α flux; Column 9: GALEX FUV flux density; Column 10: *Spitzer* 24 μ m MIR flux density; Column 11: *Spitzer* 70 μ m FIR flux density; Column 12: C-band (\sim 6 GHz) radio continuum non-thermal (synchrotron) flux density. All RC $_{\text{NTTh}}$ emission is assumed to be synchrotron and is inferred by subtracting the RC $_{\text{Th}}$ component from the total RC (Deeg et al. 1997). The quantity in parenthesis is the amount that was regarded as ‘ambiguous’; Column 13: Equipartition magnetic field strength in the plane of the sky (see Equation 3 of Beck & Krause 2005).

^BDisk parameters are derived from the Holmberg radius of B-band images.

^VB-band data was not available, so disk parameters are derived from 3 times the V-band disk scale length.

^LWhen the RC emission was integrated over the entire disk, the S/N did not exceed 3.